Volume 4, Issue 1, 2018

Journal of Biomedical Photonics & Engineering

Special Section

"Laser and optical technologies in biomedicine and ecology"

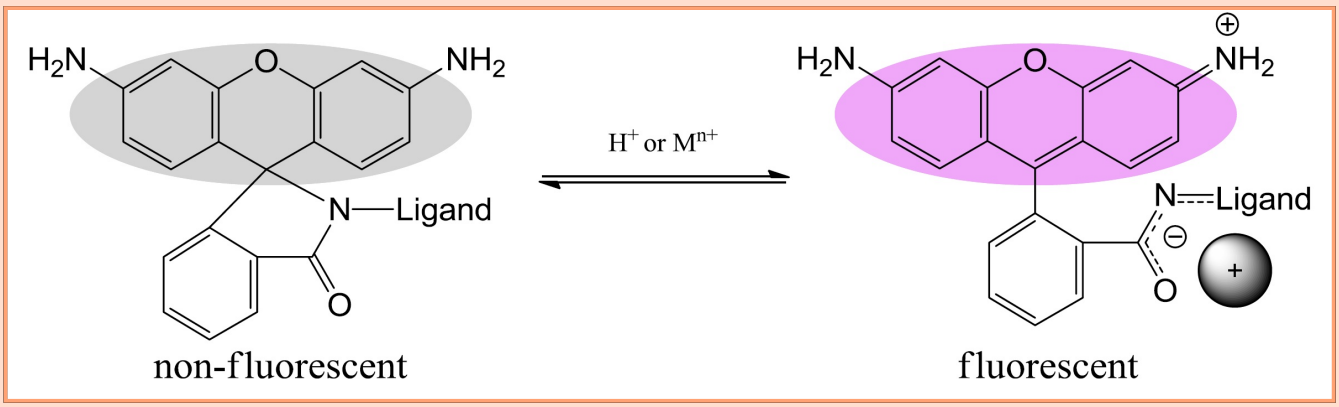

Special Section Editors
Aleksandra M. Mayorova, Valery P. Zakharov

 doi: 10.18287/JBPE18.04.010001

Journal of Biomedical Photonics & Engineering

by Samara National Research University

Volume 4, Issue 1 (March 2018)

Editorial Board

Postal address:

39B Lukacheva st., room #301

Samara 443086, Russian Federation

doi: 10.18287/JBPE18.04.010001

Special Section
“Laser and optical technologies in biomedicine and ecology”

Special Section Editors

Aleksandra M. Mayorova, Samara Branch of P.N. Lebedev Physical Institute of Russian Academy of Sciences

Valery P. Zakharov, Samara National Research University, Russia

Used Figure from this issue on the Cover

Andrey A. Leonov, et al. Luminescent Chemosensor Systems for Detecting Metal Ions in Aqueous Media, 010502, Fig. 1.

Contents

In vivo hyperspectral imaging of skin malignant and benign tumors in visible spectrum

Ivan A. Bratchenko[1]*, Violetta P. Sherendak[1], Oleg O. Myakinin[1], Dmitry N. Artemyev[1], Alexander A. Moryatov[2,3], Ekaterina Borisova[4], Latchezar Avramov[4], Larisa A. Zherdeva[1], Andrey E. Orlov[3], Sergey V. Kozlov[2,3], and Valery P. Zakharov[1]

[1] Department of Laser and Biotechnical Systems, Samara National Research University, 34 Moskovskoe Shosse, Samara 443086, Russian Federation

[2] Department of Oncology, Samara State Medical University, 89 Chapayevskaya St., Samara 443099, Russian Federation

[3] Samara Regional Clinical Oncology Dispensary, 50 Solnechnaya st., Samara 443031, Russian Federation

[4] Institute of Electronics, Bulgarian Academy of Sciences, 72 Tzarigradsko chaussee blvd, Sofia 1784, Bulgaria

*** e-mail:** iabratchenko@gmail.com

Abstract. The paper presents analysis of hyperspectral images for human skin cancer pathologies diagnostics. Hyperspectral images data contained backscattered spectra of normal skin and tumors. Analysis of hyperspectral images provided information about hemoglobin and melanin content for the differentiation of malignant and benign skin neoplasms based on tissues optical density calculation. It was shown that the accuracy of cancerous tissues classification reaches 88% for proposed algorithm of hyperspectral images analysis. The proposed approach may be a rapid and reliable tool for skin oncological diseases screening. © 2018 Journal of Biomedical Photonics & Engineering.

Keywords: hyperspectral imaging; backscattering spectroscopy; oncodermatology; oncological diagnostics; melanoma; nevi; carcinoma; melanin; hemoglobin content.

Paper #3252 received 10 Sep 2017; revised manuscript received 2 Oct 2017; accepted for publication 4 Oct 2017; published online 16 Jan 2018. doi: 10.18287/JBPE17.04.010301.

References

1. All Cancers (excluding non-melanoma skin cancer). Estimated Incidence, Mortality and Prevalence Worldwide in 2012, GLOBOCAN.
2. D. V. Karpin, V. V. Starinskiy, G. V. Petrova (Eds.), The state of oncological care for the population in 2015 in Russia, MORI - P. Herzen Moscow Oncology Research Institute, Moscow (2016) [in Russian].
3. A. V. Ermakov, "Early diagnosis and prophylaxis for cutaneous melanoma," Oncosurgery 5(3), 52-58 (2013) [in Russian].
4. N. R. Abbasi, H. M. Shaw, D. S. Rigel, R. J. Friedman, W. H. McCarthy, I. Osman, A. W. Kopf, and D. Polsky, "Early diagnosis of cutaneous melanoma: revisiting the ABCD criteria," JAMA 292(22), 2771–2776 (2004).
5. F. M. Walter, A. T. Prevost, J. Vasconcelos, P. N. Hall, N. P. Burrows, H. C. Morris, A. L. Kinmonth, and J. D. Emery, "Using the 7-point checklist as a diagnostic aid for pigmented skin lesions in general practice: a diagnostic validation study," British Journal of General Practice 63(610), 345–353 (2013).
6. G. Argenziano, G. Fabbrocini, P. Carli, V. De Giorgi, E. Sammarco, and M. Delfino, "Epiluminescence microscopy for the diagnosis of doubtful melanocytic skin lesions," Archives of Dermatology 1341(12), 1563–1570 (1998).
7. C. Benvenuto-Andrade, S. W. Dusza, A. L. C. Agero, A. Scope, M. Rajadhyaksha, A. C. Halpern, and A. A. Marghoob, "Differences Between Polarized Light Dermoscopy and Immersion Contact Dermoscopy for the Evaluation of Skin Lesions," Archives of Dermatology 143(3), 329-338 (2007).
8. P. Bourne, C. Rosendahl, J. Keir, and A. Cameron, "BLINCK—A diagnostic algorithm for skin cancer diagnosis combining clinical features with dermatoscopy findings," Dermatology Practical & Conceptual 2(2), 55-61 (2012).

9. C. Rosendahl, G. Williams, D. Eley, T. Wilson, G. Canning, J. Keir, I. McColl, and D. Wilkinson, "The impact of subspecialization and dermatoscopy use on accuracy of melanoma diagnosis among primary care doctors in Australia," Journal of the American Academy of Dermatology 67(5), 846-852 (2012).
10. C. Massone, A. Di Stefani, and H. P. Soyer, "Dermoscopy for skin cancer detection," Current Opinion in Oncology 17, 147–153 (2005).
11. G. Lu, and B. Fei, "Medical hyperspectral imaging: a review," Journal of Biomedical Optics 19(1), 010901 (2014).
12. I. Diebele, I. Kuzmina, A. Lihachev, J. Kapostinsh, A. Derjabo, L. Valeine, and J. Spigulis, "Clinical evaluation of melanomas and common nevi by spectral imaging," Biomedical Optics Express 3(3), 467-472 (2012).
13. A. Machihin, and V. Pozhar, "Double-AOTF-based aberration-free spectral imaging endoscopic system for biomedical applications," Journal of Innovative Optical Health Sciences 8(3), 1541009 (2015).
14. I. A. Bratchenko, M. V. Alonova, O. O. Myakinin, A. A. Moryatov, S. V. Kozlov, and V. P. Zakharov, "Hyperspectral visualization of skin pathologies in visible region," Computer Optics 40(2), 240-248 (2016).
15. L. A. Zherdeva, I. A. Bratchenko, O. O. Myakinin, A. A. Moryatov, S. V. Kozlov, and V. P. Zakharov, "*In vivo* hyperspectral imaging and differentiation of skin cancer," Proceedings of SPIE 10024, 100244G (2016).
16. R. O. Duda, P. E. Hart, and D. G. Stork, Pattern Classification, 2nd ed., Wiley (2001).
17. A. N. Bashkatov, E. A. Genina, V. I. Kochubey, and V. V. Tuchin, "Optical properties of human skin, subcutaneous and mucous tissues in the wavelength range from 400 to 2000 nm," Journal of Physics D: Applied Physics 38(15), 2543-2555 (2005).
18. R. L. van Veen, H. J. Sterenborg, A. Pifferi, A. Torricelli, E. Chikoidze, and R. Cubeddu, "Determination of visible near-IR absorption coefficients of mammalian fat using time- and spatially resolved diffuse reflectance and transmission spectroscopy," Journal of Biomedical Optics 10(5), 054004 (2005).
19. G. Zonios, J. Bykowski, and N. Kollias, "Skin melanin, hemoglobin, and light scattering properties can be quantitatively assessed in vivo using diffuse reflectance spectroscopy," Journal of Investigative Dermatology 117(6), 1452-1457 (2001).
20. V. P. Zakharov, I. A. Bratchenko, S. V. Kozlov, A. A. Moryatov, O. O. Myakinin, and D. N. Artemyev, "Two-step Raman spectroscopy method for tumor diagnosis," Proceedings of SPIE 9129, 91293V (2014).
21. I. A. Bratchenko, D. N. Artemyev, O. O. Myakinin, Y. A. Khristoforova, A. A. Moryatov, S.V. Kozlov, and V. P. Zakharov, "Combined Raman and autofluorescence *ex vivo* diagnostics of skin cancer in near-infrared and visible regions," Journal of Biomedical Optics 22(2), 027005 (2017).
22. E. G. Borisova, L. P. Angelova, and E. P. Pavlova, "Endogenous and Exogenous Fluorescence Skin Cancer Diagnostics for Clinical Applications," IEEE Journal of Selected Topics in Quantum Electronics 20(2), 211-222 (2014).
23. J. Zhao, H. Lui, S. Kalia, and H. Zeng, "Real-time Raman spectroscopy for automatic *in vivo* skin cancer detection: an independent validation," Analytical and Bioanalytical Chemistry 407(27), 8373–8379 (2015).
24. S.-H. Tseng, P. Bargo, A. Durkin, and N. Kollias, "Chromophore concentrations, absorption and scattering properties of human skin in-vivo," Optics Express 17(17), 14599–14617 (2009).
25. D.T. Dicker, J. Lerner, P. Van Belle, S.F. Barth, D. Guerry 4th, M. Herlyn, D.E. Elder, and W.S. El-Deiry, "Differentiation of normal skin and melanoma using high resolution hyperspectral imaging," Cancer Biology & Therapy 5(8), 1033-1038 (2006).
26. Z. Huang, H. Lui, D. I. McLean, M. Korbelik, and H. Zeng, "Raman Spectroscopy in Combination with Background Near-infrared Autofluorescence Enhances the In Vivo Assessment of Malignant Tissues," Photochemistry and Photobiology 81(5), 1219-1226 (2005).
27. W. Wang, J. Zhao, M. Short, and H. Zeng, "Real-time in vivo cancer diagnosis using raman spectroscopy," Journal of Biophotonics 8(7), 527–545 (2014).
28. X. Feng, A. J. Moy, H. T. M. Nguyen, J. Zhang, M. C. Fox, K. R. Sebastian, J. S. Reichenberg, M. K. Markey, and J. W. Tunnell, "Raman active components of skin cancer," Biomedical Optics Express 8(6), 2835–2850 (2017).
29. L. A. Austin, S. Osseiran, and C. L. Evans, "Raman technologies in cancer diagnostics," Analyst 141(2), 476-503 (2016).
30. V. P. Zakharov, I. A. Bratchenko, D. N. Artemyev, O. O. Myakinin, D. V. Kornilin, S. V. Kozlov, and A. A. Moryatov, "Comparative analysis of combined spectral and optical tomography methods for detection of skin and lung cancers," Journal of Biomedical Optics 20(2), 025003 (2015).

1 Introduction

Malignant melanoma holds a special place among other skin malignancies. It is the most aggressive skin tumor and it is responsible for more than 85% of all lethal cases from malignant skin tumors. Skin melanoma is uneven with the highest incidence rates for Australia

and New Zealand (up to 40 cases per 100.000 population), the United States of America (up to 21.1 cases per 100.000 population), and some countries in Europe [1]. In particular, in the United States in 2013, the disease was detected in 76,600 Americans, while 35% of sick people were under 45 years old. In Russia more than half a million new patients with malignant neoplasms are detected each year, and 14% of them are malignant skin tumors. Skin melanoma in Russia is less common (about 8500 cases every year - 3.97 new diseases per 100 thousand people), but also a high annual incidence rate from 4.55 to 6.1% per year can be stated for the last decade [2]. In Samara region a high incidence rates of malignant neoplasms is observed - about 446.6 new cases per 100.000 population. One of the region features is a high incidence of skin tumors; about 18.6% of all new cancers are skin cancers, and Samara holds the first place in Russia according to this index in 2015.

Skin melanoma is characterized by a variety of clinical marks, and it is especially difficult to differentiate melanoma from other skin tumors in the initial stages of the disease. Potentially dangerous pigmented skin tumors can be detected by more than 90% of the population during visual examination [3]. Hyperdiagnosis of melanoma leads to an unreasonably high volume of surgical interventions and serious cosmetic defects. Despite the significant progress achieved in systemic drug therapy for skin melanoma, the results of 5-year survival are still most dependent on timely and effective diagnosis and adequate volume of surgical treatment. Therefore, design of methods for early skin cancers diagnostics remains in high demand.

Today common practice to increase accuracy of first-hand inspection is dermatoscopy analysis of skin neoplasms. Such an analysis provides the opportunity to enlarge the standard ABCD rule [4] or 7-point checklist [5] and involve additional criteria in suspicious skin tissues inspection. For example, dermatoscopy analysis may include monitoring of more specifically related tumor features like atypical pigmentation and vascular networks as well as so-called blue-whitish veil, which represents a gray-white pattern with well perceptible blue tone [6]. Unfortunately, the features' list has been originally borrowed from epiluminescence microscopy. In most cases, that means a special immersion interface should be used to get high-quality images in contrast with the ordinary ABCD rule or 7-point checklist, which, in general, do not requires any refractive equalization agents, but, nevertheless, may be improved using these ones [7]. More precise techniques and complex criteria require more trained and qualified practitioners.

Thus, dermatoscopy opens up a new dimension on clinical morphology of pigmented skin lesions and enables well-trained physicians to improve their diagnostic accuracy up to 65% [8]. The use of dermatoscopy both improves clinical diagnostic accuracy and increases the ratio of skin cancers to all lesions biopsied or excised; moreover, this improvement is independent of the type of doctor using dermatoscopy [9]. Also, dermatoscopy in the hands of physicians with experience has higher discriminatory power than naked-eye examination to detect melanoma [10]. Despite all the advantages, dermatoscopy analysis still requires well-trained physician to handle every suspicious skin neoplasm, and thus is not suitable for mass screening applications. Further increase in accuracy of skin lesions analysis may be performed with application of spectroscopic and automatic analysis of acquired data, as digital follow-up examinations and computer-aided diagnosis provide the opportunity to perform precise mass cancer screening without well-trained physicians.

As an alternative to the dermatoscopy a hyperspectral imaging technique may be used. This technique simultaneously allows for imaging of the pathology area and spectral data acquiring. The tissue image allows one to estimate tissue morphology and allows for finding the stage of tumor growth, while the spectral data allows one to make a conclusion about the chemical composition of the tested tissue area. Hyperspectral imaging (HSI) provides information about the intensity of the reflected light at a range of wavelengths at each surface point of the image. The hyperspectral image is a three-dimensional array of $M \times N \times K$ data consisting of a sequence of K images of $M \times N$ size, and each of these images corresponds to an intensity of backscattered signal in the spectral band $\lambda_K \pm \Delta\lambda$ at each point of tested object surface. The applicability of multi- and hyperspectral imaging techniques for the analysis of cancers in visible and NIR ranges has been demonstrated in many studies [11, 12]. However, accuracy of various cancer pathologies diagnosis with hyperspectral methods implementation for the analysis of backscattering spectra is still remains under consideration.

In this study, the HSI technique was used to demonstrate the possibility of malignant and benign skin tumors differentiation based on the backscattered radiation analysis only in visible spectrum. In contrast to existing methods for diagnosing melanocytic skin tumors that use data on backscattered spectra in the visible and IR regions (see, for example, Ref. [12]), it is proposed to use data from backscattered spectra in a relatively small band of visible spectrum of 520 - 670 nm. This approach makes it possible to simplify the system of hyperspectral images recording, which ultimately will reduce the cost of the equipment used in screening surveys. The paper presents data about the analysis of tissues optical density (OD), melanin and hemoglobin content for skin malignant and benign tumors, and application of melanin and hemoglobin content data for skin tumors differentiating.

2 Materials and Methods

2.1 Hyperspectral imaging

Hyperspectral images of tissues were acquired with HSI camera developed by the Scientific and Technical

Center of Unique Instrumentation of Russian Academy of Sciences (Moscow) [13]. The setup for hyperspectral images registration is shown in Fig.1. The experimental setup includes the LED source 1, illuminating the tested tissue 2. Backscattered radiation 3 passes through the collimator 4 and enters into the acoustooptic tunable monochromator 5, controlled by an external computer 8. The controller board 14 sets the operating mode of high frequency generator 17 and amplifiers 15-16. The generator 17 and the amplifiers 15-16 creates a high frequency signal supplied to the acoustooptical cells 10 and 12 that generate acoustic waves of a certain frequency. During the passage of an acoustic wave through the acoustooptic cell, optical properties are changed so a filtration of radiation wavelengths occurs, and only radiation at wavelength λ reaches the matrix of digital camera 7. The radiation at wavelengths, that different from λ, changes direction of its propagation and does not reach the camera. The optical system can display images with spectral resolution up to 2.3 nm in the range 450-750 nm. The data transfer protocol provides the capability to obtain images with resolution 1360 × 1024px (the maximal increasing on scanning area is 7 × 7 cm). Captured hyperspectral images of skin tissues were from 5 × 5 cm to 7 × 7 cm and contained tumor and healthy tissue area. For methodology optimization, we choose 5 nm and 501 × 501px for scanning step and registration area respectively during the *in vivo* registration process of the patient's skin hypercube. Thus, each sample is characterized by the hypercube 501 × 501 × 61px. Backscattering spectra were stimulated by white LED source located in a distance of 40-50 cm from the tissue sample. The obtained data has been processed in MATLAB R2014a.

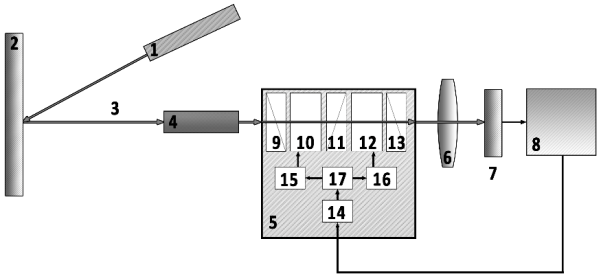

Fig. 1 Scheme of skin hyperspectral images experimental registration: 1 - broadband LED source; 2 - object; 3 - backscattered radiation; 4 - collimator; 5 - tunable monochromator; 6 – lens; 7 - digital camera; 8 - computer; 9, 11 13 - polarizers; 10, 12 - acoustooptical cells; 14 - controller; 15, 16 - high frequency amplifiers; 17 - high frequency generator.

There were 60 patients with skin cancers (38 female and 21 male, all white, Caucasian, skin phenotype I and II) enrolled in this study. A total of 10 basal cell carcinomas (BCC), 12 malignant melanomas (MM) and 37 benign neoplasms (BN) (including 13 nevi, 4 gemangiomas, 2 inflammatory lipogranulomas, 8 keratosis, 1 Bowen disease, 4 keratopapillomas and 5 different inflammatory diseases) were studied. The detailed distribution of human skin lesions, including information about tumor locations, is provided in Table 1. Every hyperspectral tumor study was accompanied by histological analysis to make a final diagnosis. The protocols of *in vivo* tissue diagnostics were approved by the ethical committee of Samara State Medical University. The institutional Review Board of Samara National Research University approved the study protocols. This research adhered to the tenets set forth in the Declaration of Helsinki. Informed consent of each subject was obtained.

Typical normalized spectra and tumor images stabilization procedure may be found elsewhere [14, 15]. Generally, to obtain quantitative estimations of various human skin tissues backscattered spectra we used data about OD of skin tissues. The diffuse backscattered reflectance from skin in spatial point *(x, y)* may be characterized by OD on the selected wavelength *λ* as:

$$OD(x,y,\lambda) = lg\frac{I_o(x,y,\lambda)}{I(x,y,\lambda)}, \qquad (1)$$

where I_0 *(x, y, λ)* is backscatter intensity from the background of light source, I *(x, y, λ)* is backscattered intensity from the tissue sample. While the exact determination of tumor type may be performed with OD analysis based on above spectral bands:

$$OD_i(x,y) = \frac{1}{\lambda_2-\lambda_1}\int_{\lambda_1}^{\lambda_2} OD(x,y,\lambda)d\lambda, \qquad (2)$$

where hemoglobin-related optical density OD_H defined for (λ_1 = 530 nm, λ_2 = 570 nm) and melanin-related OD_M for (λ_1 = 600 nm, λ_2 = 670 nm). Further, we calculated mean OD_H and OD_M values for all studied tumors and healthy skin. Allocation of tumor area was performed on the basis of approach presented in our previous studies [15]. Healthy skin region was chosen near the tumor area with 1.5 – 2 cm indentation from the tumor and included approximately 1 × 1 cm area of healthy skin. Example of hyperspectral image with tumor and healthy skin areas allocation as well as distribution of OD_M coefficient is presented in Fig. 2.

Discrimination of tumors was performed based on two approaches. First approach took into account only raw values of OD_H and OD_M coefficients, while second approach used normalized $OD^N{}_H$ and $OD^N{}_M$ coefficients. Normalization was performed as:

$$OD_i^N = \frac{OD_i^T}{OD_i^H}, \qquad (3)$$

where $OD^T{}_i$ and $OD^H{}_i$ are OD_i coefficients calculated for one patient for tumor (index ^{T}) and healthy skin (index ^{H}) areas respectively.

OD_i coefficients were used for tissue classification by discriminant analysis (DA). DA can separate two or more classes based on different statistical parameters of

Table 1 Summary of patients with skin tumors.

Lesion	Age	Gender		Location			
		Male	Female	chest/stomach	neck/head	limb	back
MM	39-77	4	8	2	-	4	6
BCC	36-82	6	4	1	5	1	4
BN	21-84	11	26	5	6	9	13

Gaussian distributions. The efficiency of the proposed approach is characterized by sensitivity and specificity and ability to select defined classes in different areas of phase plane. The analysis of skin tissues data allocation was performed using quadratic DA classifiers [16].

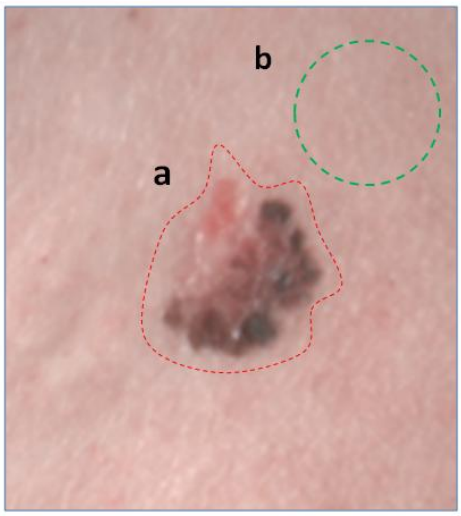

Fig. 2 Hyperspectral image of *in vivo* skin sample containing MM (a) and healthy skin (b) regions (5 × 5 cm)

2.2 Diffuse-reflectance spectra measurement

For reflectance measurements a halogen lamp with broad-band output spectrum (370-1050 nm) was applied. Optical fiber probe R400-7-VIS-NIR (400um Reflection Probe, VIS/NIR, 2m (Ocean Optics Inc., Dunedin, FL, USA) was used to deliver the light from laser and lamp and to collect the diffuse reflectance signals. The spectra were recorded and stored using a fiber-optic microspectrometer (USB4000-VIS-NIR, Ocean Optics, Dunedin, FL, USA). A personal computer was used to control the system and to store and display the data using the specialized microspectrometer software SpectraSuite ("Ocean Optics", Inc., Dunedin, FL, USA).

For reflectance measurement mode initial calibration was carried out before every measurement. The portion of the light reflected from a sample is expressed as a percentage R [%] relative to a standard reflectance (Spectralon®). The reflectance R [%] is calculated by the following equation:

$$R_\lambda = \frac{S_\lambda - D_\lambda}{SR_\lambda - D_\lambda} \times 100\%, \quad (4)$$

where R_λ is the reflectance [%], S_λ is the light intensity reflected by the sample at each wavelength, D_λ the dark intensity at each wavelength (correction signal for detector dark current), SR_λ the standard reference reflectance intensity at each wavelength.

Spectroscopic measurements of normal skin and lesion areas were carried out after 5-10 minutes of rest for each patient at room temperature (23 to 25 ˚C). Several spectra were measured from each suspicious area and averaged to reduce the influence of inhomogeneity of the lesions. It was recorded and averaged five to seven spectra from every lesion, depending on its size, and three to five spectra from surrounding normal skin. These averaged spectra from the health skin area were used like an indicator of the spectral changes in the pathological areas. The spectra were smoothed using the Savitzky-Golay algorithm in order to reduce the instrumental noise of the spectrometric system. A constant distance of 2 mm between the end tip of the optical fibers and the skin surface were applied, using a mechanical stand to avoid any influence of displacement from the normal position on the intensity level. All spectra were obtained at normal incidence - at the 90^o angle between optical fibers end tip and skin surface. This geometry was carefully reproduced in all measurements to minimize diffuse reflectance intensity changes related to distance, and reflectance spectral shape changes related to the angle uncertainties during measurements.

Before every spectroscopic measurement a clinical observation and dermatoscopic evaluation of the lesion under interest was made. After these initial medical and spectroscopic measurements a histological samples were obtained from every lesion. The results from histological examination were used as a “gold standard” in comparison of all data obtained.

In this study we had included diffuse reflectance results from 102 patients, distributed as follow: 39 - benign nevi, 35 -dysplastic nevi, 28 - pigmented malignant melanoma (nodular and lentigo MM).

3 Results and Discussion

In the visible region of the spectrum (400-800 nm), the main chromophores of biological tissues are hemoglobin and melanin, since proteins absorb radiation in the shorter-wave and longer-wave regions,

water in the longer-wave region, and fats have a local absorption maximum near 750 nm [17, 18]. The presence of such a transparency window of biological tissues allows for studying the internal structure of a thin surface layer of tissue with up to several millimeters depth [19]. In this case, the dependence of the extinction coefficient of melanin has a descending shape in the 450 - 750 nm region, while hemoglobin extinction coefficient in the same spectral region has two local maxima near the 530 nm and 570 nm regions. Moreover, upon transition to a longer wavelength region (600-800 nm), the value of the extinction coefficient of hemoglobin is much smaller and becomes several orders of magnitude lower than extinction melanin in the same region. Thus, to estimate hemoglobin and melanin content in the skin we calculated OD_H coefficient in 530 - 570 nm area and OD_M in 600 - 670 nm area.

In diffuse-reflectance spectroscopy mode the most significant differences are related to the influence of skin pigments – melanin and hemoglobin from the blood. They are responsible for the shape of the reflectance spectra observed in the region of 350-1000 nm. On Fig. 3 are presented averaged, compared by pathology type lesions vs. normal skin reflectance. Malignant melanoma (MM) lesions (28 patients) had the lowest reflectance intensity in the whole spectral range in VIS-NIR region. The dysplastic nevi reflectance is similar by intensity levels and could not be easily separated by values from MM, but the spectral shape differences observed, related to a reduced slope values of the reflectance curve in the region of 600-900 nm is typical for the non-melanoma pigmented lesions, while for a normal skin it is expressively negative by value and strongly positive for all pigmented melanoma lesions detected.

Thus, differentiation of pathologies from normal tissues and distinguishing one type of tumor from the other is possible with backscattered spectrum analysis in the visible region, since it contains data on hemoglobin and melanin content in skin tissues. In current study for the differentiation of skin tissues we used values of OD for melanin and hemoglobin content. Fig. 4 shows distributions of OD_H and OD_M coefficients for BN and malignant skin tissues. One may see that MM and BCC have almost the same values of OD_H. This fact proves our assumption about vast capillary network in malignant tumors in comparison to BN, as BN formations contain less blood according to Fig. 4 (a) data. For melanin content (Fig. 4 (b)) we may note a vast dispersion for BCC data, but this fact may be caused by rather small number of studied BCCs. Also, it is interesting to note that medians for OD_H and OD_M distributions for all three studied skin classes (MM, BCC and BN) have almost identical values.

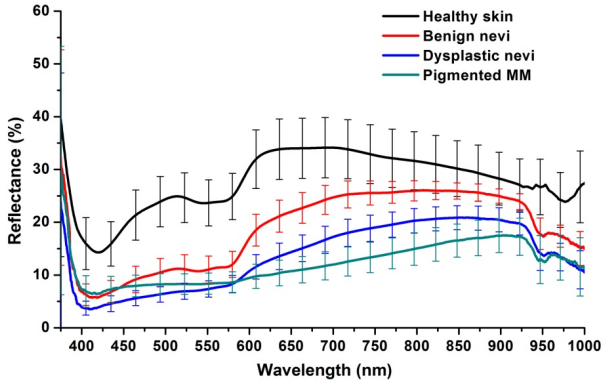

Fig. 3 Diffuse reflectance spectra of melanin-pigmented lesions vs. healthy skin tissue reflectance. Spectra are averaged by the set of lesions of different pathologies investigated and the standard deviation is presented as error bars.

In general, application of OD_H and OD_M coefficients shows accuracy of skin tissues classification on 55 – 60 % level. Increase of skin tissues classification accuracy is possible with joint implementation of two criteria. This approach may be implemented with phase plane analysis. In separation of phase plane classes axes of the plane are criterions of tissues classification, and every tested sample is a point on the phase plane with coordinates corresponding to the criterion values for this tissue sample [20]. Phase plane analysis was performed for OD_H and OD_M coefficients pair. Example of phase plane analysis is shown in Fig. 5. Separation of BCC and MM was performed with quadratic DA, axes of phase plane in Fig. 5 are OD_H and OD_M.

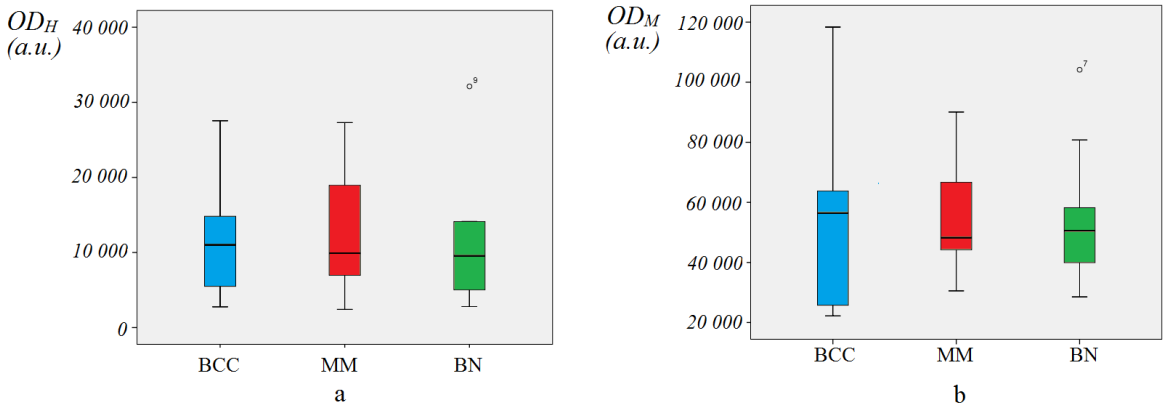

Fig. 4 Whisker and box plots for OD_H (a) and OD_M (b) distribution of skin tissues.

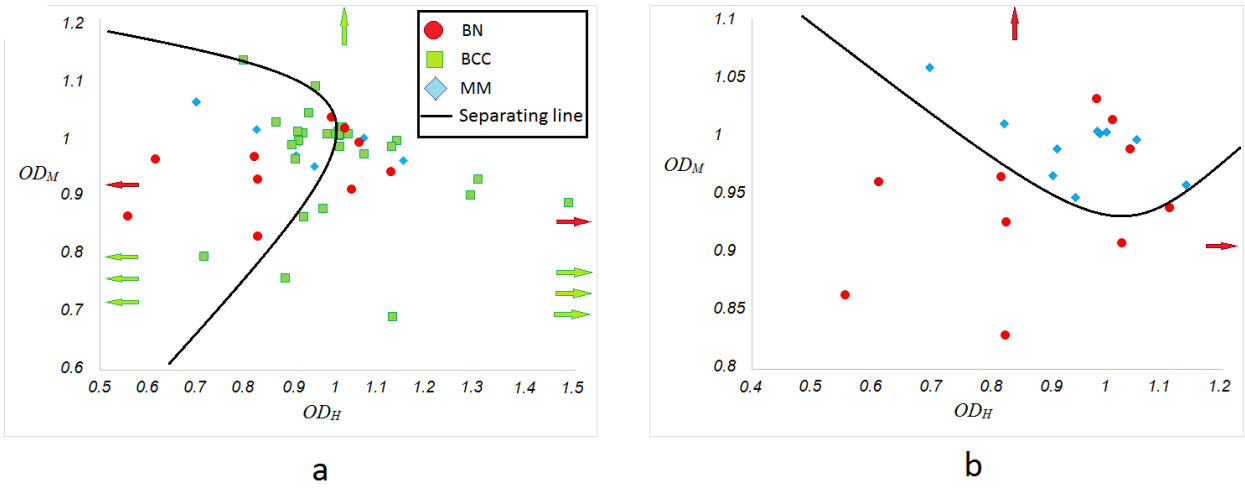

Fig. 5 Skin neoplasms separation on phase plane with OD_H and OD_M coefficients and quadratic DA: malignant tissues vs BN (a) and MM vs BCC (b).

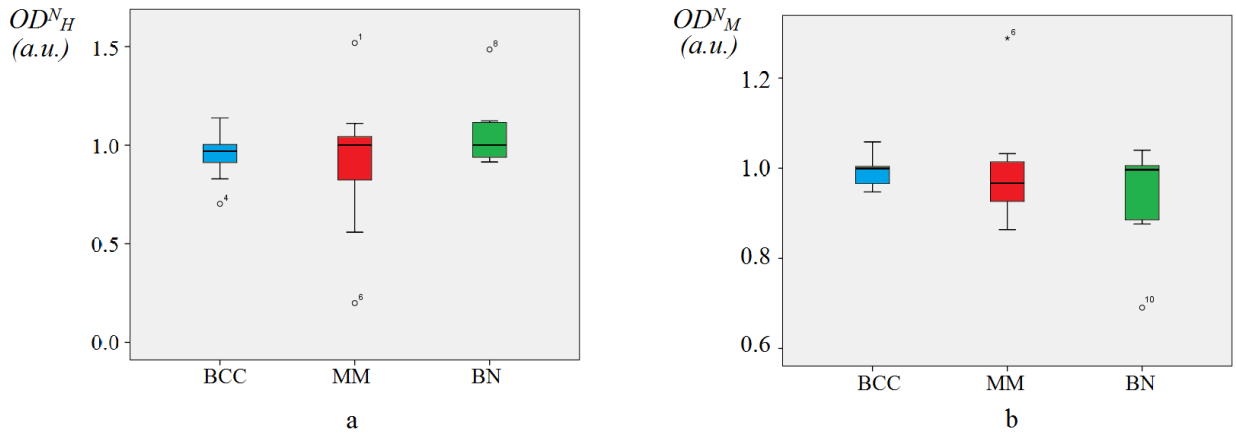

Fig. 6 Whisker and box plots for $OD^N{}_H$ (a) and $OD^N{}_M$ (b) distribution of skin tissues.

Fig. 7 Skin neoplasms separation on phase plane with $OD^N{}_H$ and $OD^N{}_M$ coefficients and quadratic DA: malignant tissues vs BN (a) and MM vs BCC (b).

Both classifications presented in Fig. 5 (malignant vs BN and MM vs BCC) provides 68% accuracy. Here sensitivity and specificity for malignant vs BN classification are 82% and 54% respectively; and sensitivity and specificity for MM vs BCC classification are 75% and 60% respectively. Rather low accuracy of about 70% in skin tissues classification in comparison with other optical techniques application for skin pathologies analysis [21-23] may be caused by high dispersion in melanin and hemoglobin content in skin

for different persons. A number of studies demonstrates a clear contrast between skin phototypes, skin sites, and wavelengths for main skin chromophores concentrations [24]. Thus, we may take into account initial variations of skin properties and count these variations in OD_H and OD_M coefficients calculation.

In order to account initial skin chromophores concentrations we may normalize OD_H and OD_M coefficients for tested tumors on the values of the same coefficients for normal skin of the same patient. Details of normalized OD^N_H and OD^N_M coefficients calculation are presented in section 2.3. Fig. 6 demonstrates whisker and box plots for OD^N_H and OD^N_M distributions for skin tissues. Comparison of Fig. 4 and Fig. 6 shows that normalization of OD_H and OD_M on the values of normal skin helps to slightly improve the separation of skin tissues classes based on melanin and hemoglobin content calculation.

Application of OD^N_H and OD^N_M coefficients for skin tissues separation helps to achieve about 60 – 70 % accuracy, that is 5 – 10 % higher than for the OD_H and OD_M coefficients implementation. Analysis of phase planes for malignant and BN tissues separation and MM and BCC separation is presented in Fig. 7. Here separation of malignant and BN tissues is possible with sensitivity and specificity of 64% and 73% correspondingly and total accuracy of 69%. This accuracy is almost the same as in the case of OD_H and OD_M coefficients application. However, separation of MM and BCC is possible with sensitivity and specificity of 75% and 100% correspondingly and total accuracy of 88%. Additionally, it is interesting to note, that separation of MM and BN is possible with 68% accuracy for OD_H and OD_M coefficients, and with 74% accuracy for OD^N_H and OD^N_M.

Comparing the proposed method with the previously developed methods of MM instrumental detection [11, 22, 25, 26] one may say that the developed method can compete not only with other hyperspectral methods of analysis of biological tissues, but also with such types of optical analysis of biological tissues as an autofluorescence analysis and Raman spectroscopy. Despite slightly less values of total accuracy for skin tissues classification in comparison to Raman spectroscopy study [21, 23], hyperspectral imaging provides an ability to scan large tissue areas and detect suspicious formations. Raman spectroscopy today commonly used to measure tissue properties only in a single point [27-29]. The proposed hyperspectral imaging setup allows for achieving almost the same results of MM and BN separation when compared with hyperspectral techniques using data both from visible and NIR spectra [12]. Although, to make a reliable comparison of the results of the proposed method with the data of other studies, more wide studies on the registration and analysis of hyperspectral images of skin tumors are required.

4 Conclusion

The developed method of human skin tumors differentiation may become a simple and reliable approach for mass screening applications, as it allows for quickly detection and classification of malignant tumors with relatively inexpensive equipment. Registration of tissue hyperspectral image is possible within 15-20 seconds, so the proposed technique may be used directly in clinics. In addition, in the proposed approach, only the white LED light illuminator is used as a radiation source. All of this makes the system used in the study a reliable, quick and inexpensive device of skin mass screening applications.

Comparison of the achieved results with the existing hyperspectral methods of skin pathologies detection [12] allows us to say that the developed approach makes it possible to confidently detect malignant tumors and uses for this purpose only the spectral response of the skin in visible spectrum. Comparison of similar approaches of skin tumors diagnostics using information about backscattered radiation in the visible spectrum [25] also supports the proposed experimental technique. Dicker et al [25] applied hyperspectral imaging in the visible spectra only for *ex vivo* diagnostics of pigmented skin tumors, while the proposed method successfully work with real patients in clinics. In addition, the proposed method can become a part of a more complex system of tissues optical monitoring. This may be done by combining the results of the study with data obtained by other optical methods [27, 30].

Further development of the proposed system is possible in several directions. The first is to conduct more wide *in vivo* studies both with samples of skin tumors and with other human tissues samples to establish the exact diagnostic capabilities of the proposed technique. The second direction is the creation of an automatic algorithm for the detection of tumors in hyperspectral images, which would allow for determining the tumor presence and analysis of tumor type based on the data of backscattered spectra. Thus, the proposed approach to mass screening of skin tumors may significantly increase the accuracy of oncological pathologies diagnosis during the "first-hand" examinations in clinics.

Disclosures

All authors declare no conflict of interests for this paper and have no financial interest in the materials used in the chapter.

Acknowledgements

This research was supported by the Ministry of Education and Science of the Russian Federation.

Average refractive index of tendon as a function of water content

Marina E. Shvachkina*, Dmitry D. Yakovlev, Alexander B. Pravdin, and Dmitry A. Yakovlev
Department of Optics and Biophotonics, Faculty of Physics, Saratov State University, 83 Astrakhanskaya st, Saratov 410012, Russia

*** e-mail:** marevesh@mail.ru

Abstract. Experimental data on the dependence of the average refractive index of rat tail tendon (RTT) on water content are reported. Using optical coherence tomography, the average group refractive index (at a wavelength of 930 nm) and cross-section area of rat tail tendon fascicle specimens during their air-drying and rehydration were monitored. The dependence of the average group refractive index of RTT (n_g) on the volume fraction of water (C_w) has been found to be nonlinear and to be well approximated by the quadratic polynomial $n_g = 1.5713 - 0.1969C_w - 0.0328(C_w)^2$. The reported data are shown to be in good agreement with previously published data for bovine cornea. © 2018 Journal of Biomedical Photonics & Engineering.

Keywords: collagen; tissue; refractive index; water content; hydration.

Paper #3268 received 23 Dec 2017; revised manuscript received 1 Mar 2018; accepted for publication 16 Mar 2015; published online 31 Mar 2018. doi: 10.18287/JBPE18.04.010302.

References

1. S. L. Jacques, "Optical properties of biological tissues: a review," Physics in Medicine and Biology 58(11), R37-R61 (2013).
2. F. P. Bolin, L. E. Preuss, R. C. Taylor, and R. J. Ference, "Refractive index of some mammalian tissues using a fiber optic cladding method," Applied Optics 28(12), 2297-2303 (1989).
3. G. J. Tearney, M. E. Brezinski, B. E. Bouma, M. R. Hee, J. F. Southern, and J. G. Fujimoto, "Determination of the refractive index of highly scattering human tissue by optical coherence tomography," Optics Letters 20(21), 2258-2260 (1995).
4. A. R. Knuettel and M. Boehlau-Godau, "Spatially confined and temporally resolved refractive index and scattering evaluation in human skin performed with optical coherence tomography," Journal of Biomedical Optics 5(1), 83-93 (2000).
5. M. Ohmi, Y. Ohnishi, K. Yoden, and M. Haruna, "In vitro simultaneous measurement of refractive index and thickness of biological tissue by the low coherence interferometry," IEEE Transactions on Biomedical Engineering 47(9), 1266-1270 (2000).
6. X. Wang, C. Zhang, L. Zhang, L. Xue, and J. Tian, "Simultaneous refractive index and thickness measurements of bio-tissue by optical coherence tomography," Journal of Biomedical Optics 7(4), 628-632. (2002).
7. Y. L. Kim, J. T. Walsh Jr, T. K. Goldstick, and M. R. Glucksberg, "Variation of corneal refractive index with hydration," Physics in Medicine and Biology 49(5), 859-868 (2004).
8. J. Lai, Z. Li, C. Wang, and A. He, "Effective refractive indices of biological tissues and its experimental determination," Proceedings of SPIE 5630 (2005).
9. H. Ding, J. Q. Lu, W. A. Wooden, P. J. Kragel, and X. H. Hu, "Refractive indices of human skin tissues at eight wavelengths and estimated dispersion relations between 300 and 1600 nm," Physics in Medicine and Biology 51(6), 1479-1489 (2006).
10. J. Kim, D. P. Dave, C. G. Rylander, J. Oh, and T. E. Milner, "Spatial refractive index measurement of porcine artery using differential phase optical coherence microscopy," Lasers in Surgery and Medicine 38(10), 955-959 (2006).
11. J. Sun, S. J. Lee, L. Wu, M. Sarntinoranont, and H. Xie, "Refractive index measurement of acute rat brain tissue slices using optical coherence tomography," Optics Express 20(2), 1084-1095 (2012).

12. D. Maciel, S. P. Veres, H. J. Kreuzer, and L. Kreplak, "Quantitative phase measurements of tendon collagen fibres," Journal of Biophotonics 10(1), 111-117 (2017).
13. Z. C. Deng, J. Wang, Z. X. Hu, J. C. Mei, and Q. Ye, "Study on the relation between the refractive index of fresh muscle tissue and its water content from 400 to 750 nm," Journal of Modern Optics 65(4), 451-455 (2017).
14. A. M. Zysk, S. G. Adie, J. J. Armstrong, M. S. Leigh, A. Paduch, D. D. Sampson, F. T. Nguyen, and S. A. Boppart, "Needle-based refractive index measurement using low-coherence interferometry," Optics Letters 32(4), 385-387 (2007).
15. L. Oliveira, A. Lage, M. P. Clemente, and V. V. Tuchin, "Optical characterization and composition of abdominal wall muscle from rat," Optics and Lasers in Engineering 47(6), 667-672 (2009).
16. T. K. Biswas and T. M. Luu, "In vivo MR measurement of refractive index, relative water content and T2 relaxation time of various brain lesions with clinical application to discriminate brain lesions," Internet Journal of Radiology 13(1), 1 (2011).
17. P. Fratzl, "Collagen: structure and mechanics, an Introduction," in Collagen, Springer, New York, USA, 1-13 (2008).
18. P. Kannus, "Structure of the tendon connective tissue," Scandinavian journal of medicine and science in sports 10(6), 312-320 (2000).
19. H. R. Screen, V. H. Chhaya, S. E. Greenwald, D. L. Bader, D. A. Lee, and J. C. Shelton, "The influence of swelling and matrix degradation on the microstructural integrity of tendon," Acta Biomaterialia 2(5), 505-513 (2006).
20. A. A. de Aro, B. de Campos Vidal, and E. R. Pimentel, "Biochemical and anisotropical properties of tendons," Micron 43(2), 205-214 (2012).
21. J. Kastelic, A. Galeski, and E. Baer, "The multicomposite structure of tendon," Connective Tissue Research 6(1), 11-23 (1978).
22. R. W. D. Rowe, "The structure of rat tail tendon," Connective Tissue Research 14(1), 9-20 (1985).
23. V. V. Tuchin, Tissue optics: light scattering methods and instruments for medical diagnosis, SPIE press, Bellingham, Washington (2015).
24. A. T. Yeh, B. Choi, J. S. Nelson, and B. J. Tromberg, "Reversible dissociation of collagen in tissues," Journal of Investigative Dermatology 121(6), 1332-1335 (2003).
25. W. V. Sorin, and D. F. Gray, "Simultaneous thickness and group index measurement using optical low-coherence reflectometry," IEEE Photonics Technology Letters 4(1), 105-107 (1992).
26. X. J. Wang, T. E. Milner, M. C. Chang, and J. S. Nelson, "Group refractive index measurement of dry and hydrated type I collagen films using optical low-coherence reflectometry," Journal of Biomedical Optics 1(2), 212-217 (1996).
27. Z. Bor, K. Osvay, B. Racz, and G. Szabo, "Group refractive index measurement by Michelson interferometer," Optics Communications 78(2), 109-112 (1990).
28. M. Born, and E. Wolf, Principles of optics: electromagnetic theory of propagation, interference and diffraction of light, Cambridge University Press, Cambridge (1999).
29. D. J. Segelstein, The complex refractive index of water, Doctoral dissertation, University of Missouri-Kansas City, Kansas City (1981).
30. F. De Chaumont, S. Dallongeville, N. Chenouard, N. Herve, S. Pop, T. Provoost, V. Meas-Yedid, P. Pankajakshan, T. Lecomte, Y. Le Montagner, T. Lagache, A.Dufour, and J.-C. Olivo-Marin, "Icy: an open bioimage informatics platform for extended reproducible research," Nature Methods 9(7), 690-696 (2012).
31. D. M. Maurice, "The structure and transparency of the cornea," The Journal of Physiology 136(2), 263-286 (1957).
32. K. M. Meek, N. J. Fullwood, P. H. Cooke, G. F. Elliott, D. M. Maurice, A. J. Quantock, R. S. Wall, and C. R. Worthington, "Synchrotron x-ray diffraction studies of the cornea, with implications for stromal hydration," Biophysical Journal 60(2), 467-474 (1991).
33. E. P. Katz, and S. T. Li, "Structure and function of bone collagen fibrils," Journal of Molecular Biology 80(1), 1-15 (1973).
34. D. W. Leonard, and K. M. Meek, "Refractive indices of the collagen fibrils and extrafibrillar material of the corneal stroma," Biophysical Journal 72(3), 1382-1387 (1997).
35. C. Morin, C. Hellmich, and P. Henits, "Fibrillar structure and elasticity of hydrating collagen: a quantitative multiscale approach," Journal of Theoretical Biology 317, 384-393 (2013).
36. S. Hayes, T. White, C. Boote, C. S. Kamma-Lorger, J. Bell, T. Sorenson, N. Terrill, O. Shebanova, and K. M. Meek, "The structural response of the cornea to changes in stromal hydration," Journal of The Royal Society Interface 14(131), 20170062 (2017).
37. J. C. Martinez-Anton, and E. Bernabeu, "Spectrogoniometry and the WANTED method for thickness and refractive index determination," Thin Solid Films 313, 85-89 (1998).

1 Introduction

One of the optical parameters that can be directly measured for biological tissues is the average refractive index of the tissue [1-15]. In the literature, one can find estimates of the average refractive index for many types of tissues (cornea, sclera, dermis, epidermis, brain tissue *etc.*; see, *e.g.*, [1, 2, 4, 7-13, 15, 16]). The average refractive index depends on tissue composition and, in particular, on the water content [1]. The water content is one of the most variable and important tissue parameters, and the possibility to evaluate it from the measured values of the average tissue refractive index is of great practical interest. However, to date direct measurements of the average tissue refractive index as a function of tissue water content have been made only for a small number of tissues, *e.g.*, muscle tissue [13, 15] and brain tissues [1, 16]. Of collagenous tissues, as far as we are aware, reliable estimates of the average refractive index as a function of water content were obtained only for cornea [7], which is a tissue with a very high water content – normal cornea contains about 76 wt % water and 15 wt % collagen [17]. In this paper we present experimental estimates for the average tissue refractive index as a function of water content for tendon, a collagenous tissue with the highest normal collagen content—tendons contain typically 24–38 wt % collagen and 55–72 wt % water [18-20]. The experiments reported here were performed on rat tail tendon (RTT) fascicles. Fascicles are secondary collagen bundles of tendons [20-22]. Their composition and collagen fibril packing are similar to those of collagen fibers of dermis and sclera [17]. But fascicles, whose diameter typically lies within the range from 250 to 500 μm, are tens times thicker than dermal and scleral collagen fibers, which makes them quite convenient for experimentation. Due to their relatively simple structure, ease of extraction and manipulation, and ready availability, RTT fascicles are a very popular model object for studying physical and physiological properties of collagen fibers and collagenous tissues. For example, they are used in studying the effect of immersion agents, which are employed in the immersion optical clearing technique [23], on collagen bundles (see, *e.g.*, [24]). The quantitative data presented here can be used in such studies as reference data. For example, these data can be used for evaluating the duration of the solely dehydration stage of the immersion agent – biotissue interaction.

2 Methods

In order to determine the average refractive index of RTT fascicles as a function of water content, we monitored, using optical coherence tomography (OCT), the cross-section area and average refractive index of RTT fascicle specimens during their air-drying from the native state to the air-dry state and in the process of rehydration of dried specimens in normal saline solution (NSS: aqueous solution of 0.9 wt % NaCl). A series of measurements began with the measurement of the cross-section area and refractive index of the sample in its initial (native) state. The fascicle, being submerged in NSS, was mounted, in a slightly stretched state, on an object-plate using binder clips and covered with a cover-slip. Then it was placed in the OCT beam path so that the direction of the fascicle was perpendicular to the B-scan direction in order to obtain an OCT-scan of the cross-section of the fascicle (Fig. 1a). After that, the cover-slip was removed, and the NSS was quickly removed from the surface of the object-plate with a filter paper. The (non-covered) sample was placed on the OCT scanner stage in the same position as before in order to monitor the sample parameters during its dehydration in air at room temperature (Fig. 1b, c). To estimate the parameters of the sample in the standard air-dry state, the sample was allowed to dry for 1 hr at 105°C (Fig. 1d). For rehydration measurements, the dried fascicle on the object-plate was surrounded by a large amount of NSS and covered by a cover-slip.

One of the parameters that was traced in the experiment was the coefficient of fascicle volume change (volume factor)

$$k_s = V/V_0, \tag{1}$$

where V is the current value of tissue volume and V_0 is the volume of the tissue in the initial state. In our experiments, the tendon fascicle with fixed ends remained slightly stretched during both the dehydration and following rehydration, *i.e.* the length of the fascicle did not change. Therefore the volume factor can be calculated as

$$k_s = S/S_0, \tag{2}$$

where S and S_0 are the values of the cross-section area at the moment of measuring and in the initial state, respectively.

The measured values of k_s were used for estimating the water volume fraction C_w in the tissue. By definition,

$$C_w = V_w / V, \tag{3}$$

where V is the volume of the tissue and V_w is the volume of water in the tissue. On the assumption that to a good accuracy

$$V = V_{dry} + V_w, \tag{4}$$

where V_{dry} is the volume of the tissue in the dry state, it follows from (1) and (3) that

$$C_w \approx \frac{k_s - k_{s\,dry}}{k_s}, \tag{5}$$

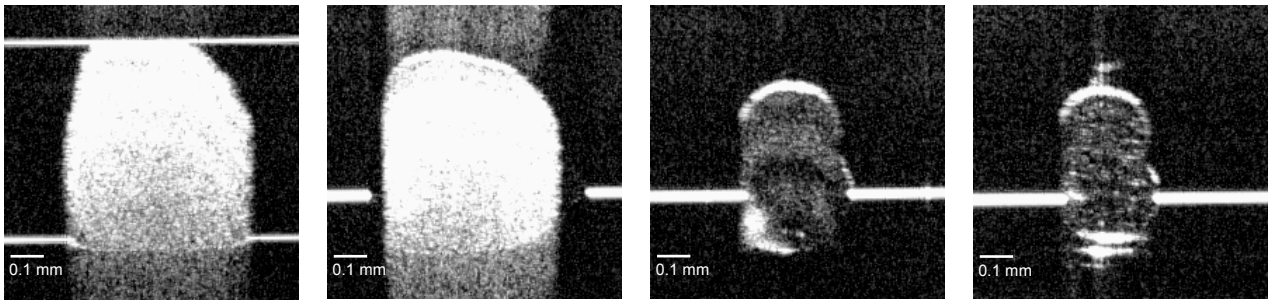

Fig. 1 OCT-images of a transverse cross-section of an RTT fascicle (a) in normal saline solution (native state), (b) after air-drying at room temperature for 1.7 min, (c) after air-drying at room temperature for 24 min, and (d) after air-drying at 105°C for 1 hour.

where $k_{s\,dry}$ is the value of k_s for the dry state. For the native state, $C_w = 1 - k_{s\,dry}$.

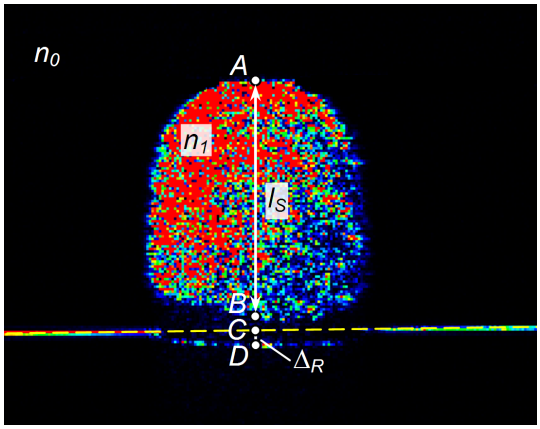

Fig. 2 Parameters used in the calculations of the average group refractive index of the tissue from an OCT-image of the specimen.

To estimate the average refractive index of the tissue using OCT, we employed a common method [3, 7, 25, 26] in which the group refractive index and physical thickness of the sample are determined from the measured values of the optical path length $l_S = n_1 d$, where d is the physical thickness of the sample for the given A-scan line and n_1 is the average group refractive index of the sample for this scan line, and shift Δ_R of the image of a reflecting surface arranged beyond the sample with respect to its position in the absence of the sample (in our experimental geometry, as in [26], the role of this reflecting surface is played by the frontal surface of the object–plate (glass substrate); see Fig.2). In an example in Fig. 2, where an OCT-image of a transverse section of an RTT fascicle is shown, apart from a common scale factor, $l_S = |\mathrm{AB}|$ and $\Delta_R = |\mathrm{CD}|$. Given l_S and Δ_R, the average refractive index of the sample n_1 for the A-scan line under consideration can be calculated as

$$n_1 = \frac{n_0 l_S}{l_S - \Delta_R},$$

where n_0 is the group refractive index of the surrounding medium (in our experiments, air or NSS). We calculated the average group refractive index of the specimen for the given cross-section as an average over several (3 to 5) A-scan lines. The group refractive index of the surrounding medium was calculated from dispersion data for the phase refractive index of the medium using the following common relation [27, 28]:

$$n_g(\lambda_0) = n_p(\lambda_0) - \lambda_0 \left.\frac{dn_p}{d\lambda}\right|_{\lambda=\lambda_0}, \qquad (6)$$

where n_p is the phase refractive index, n_g is the group refractive index, and λ_0 is the central wavelength of the probing radiation in vacuum. For the OCT-system that we used, ThorLabs-OCP930SR, $\lambda_0 = 930$ nm. We took $n_g(930\text{ nm}) = 1$ for air and $n_g(930\text{ nm}) = 1.3416$ for NSS. The phase refractive index of NSS was assumed to be approximately equal to the phase refractive index of water. For water, we used the dispersion data reported in [29], which gave the mentioned value of 1.3416.

The area S [see(2)] was calculated using the formula

$$S = \frac{S_{\text{OCT-pix}}\, k_{pm^2}}{n_{gt}}, \qquad (7)$$

where $S_{\text{OCT-pix}}$ is the area of the specimen cross-section in the OCT-image in pixels, k_{pm^2} is an instrument scale factor (in our case, $k_{pm^2} = 1.2632 \cdot 10^{-5}$ mm^2/pixel), and n_{gt} is the value of the average group refractive index of the specimen calculated from the OCT data for this cross-section as described above. To find $S_{\text{OCT-pix}}$ we used the open-source image analysis software Icy [30].

An example of the measured time-dependences of the volume factor k_s (2) and the average group refractive index of the tissue in the process of air-drying for a sample of RTT fascicle is presented in Fig. 3. It is clearly seen that the shrinkage of the tissue due to water

loss is accompanied by an increase in its average refractive index.

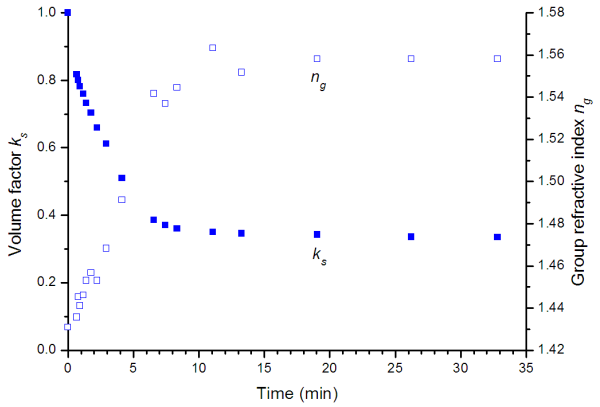

Fig. 3 Change of the volume factor k_s and average refractive index n_g of an RTT fascicle specimen during air-drying at room temperature.

Since the samples were relatively small in size, the boundaries of the sample and the upper boundary of the object-plate under the sample were clearly visible in OCT images even when the sample was in the native state, and their position could be determined with good accuracy. This ensured high accuracy of cross-section area measurements, which is confirmed by a small scatter of points in k_s *vs* time plots (as an example see Fig. 3). At the same time the samples were sufficiently thick for the relative accuracy of group refractive index measurements to be of the order of 0.3–0.5%.

3 Samples

Fascicles were excised from the tails of mature rats within one hour after decapitation, then immediately immersed in NSS. All refractive-index measurements were performed on fascicles ranging in diameter from 300 to 400 μm. The storage time of samples in NSS before they were used in experiments did not exceed 7 days. No statistically significant change (Friedman test, probability value $p = 0.32$) in the average refractive index of RTT fascicle specimens was observed during 7-day storage in NSS (see Fig. 4).

The studies were approved by the Ethics Committee of Saratov State Medical University (Saratov, Russia).

4 Results and discussion

Fig. 5 shows the measured dependences of the average refractive index, n_g, on the volume factor k_s for four samples of RTT fascicles, samples 1, 2, 3, and 4. The OCT data for sample 1 were collected during 30 min when this sample was dried at room temperature. Sample 2 was dried at room temperature for 2 hr, then held for 1 hr at 50°C, and finally held for 1 hr at 105°C. Sample 3 was dried for 40 min at room temperature and then for 1 hr at 105°C. Sample 4 was first dried at room temperature for 20 min and then placed in NSS for rehydration. From Fig. 5, it can be seen that the data for different samples are in good agreement, as are the data for drying and rehydration of sample 4.

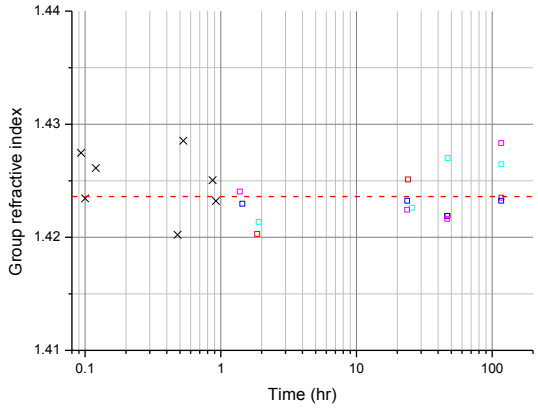

Fig. 4 Time and intersample variation of the measured refractive index for RTT specimens stored in normal saline solution (NSS). Abscissa: time of sample storage in NSS. The squares of the same color correspond to the same RTT fascicle specimen. The crosses correspond to different specimens. The red dash line shows the average value of n_g over all experimental points on this graph.

An average value of n_g for RTT fascicles in the native state was found to be 1.423 ±0.003 (mean ± SD; 12 samples). This value is shown by the black triangle in Fig. 5. An average value of $k_{s\,dry}$ was 0.323 ±0.003 (mean±one-half of the range; 3 samples), and, consequently, the average volume fraction of water for fascicles in the native state can be estimated as 0.677 ±0.003 [see (5)]. Taking 0.677 ±0.003 for C_w and 1.34 for the specific gravity ρ_{dry} of the dry tissue [31], we may estimate the average weight water content for the samples in the native state as 61 ±0.3 wt %.

In Fig. 6, the measured values of n_g for RTT are plotted against the volume water fraction C_w, C_w being calculated by (5) at $k_{s\,dry} = 0.323$. Kim *et al.* [7] reported the measured values of the group refractive index as a function of a hydration parameter H for bovine cornea at $\lambda_0 = 819.9$ nm. The hydration H of tissue is defined as the ratio of the weight of water to the dry weight. Having calculated C_w from H as

$$C_w = \frac{H\rho_{dry}}{1 + H\rho_{dry}} \qquad (8)$$

at $\rho_{dry} = 1.34$, we transferred the experimental data for cornea [7] to Fig. 6 for comparison. It can be seen from the figure that the data for tendon and cornea fit rather well.

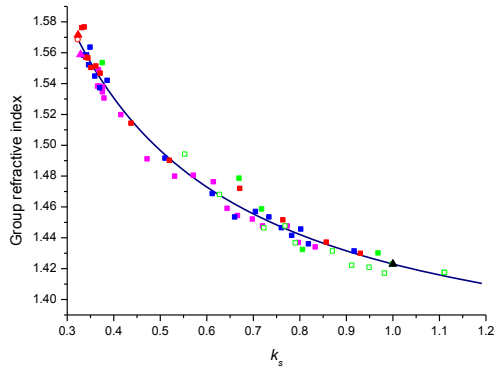

Fig. 5 Group refractive index of RTT fascicles *vs* volume factor k_s. The blue squares (■) show experimental points (k_s, n_g) for sample 1 (air-dried at room temperature). The red symbols (■, ▲, ○) represent the data for sample 2: the squares (■) are the points obtained during air-drying at room temperature; the open circle (○) and solid triangle (▲) show the points obtained on air-drying at 50°C and 105°C, respectively. Purple symbols (■, ▲) show the data for sample 3: the squares (■) are for air-drying at room temperature, and the triangle (▲) is for air-drying at 105°C. The green symbols (■, □) are for sample 4: the solid squares (■) are for the stage of air-drying, and open squares (□) are for the stage of rehydration (80 min). The black triangle (▲) shows the average value of n_g of RTT fascicles in the native state (over 12 specimens).

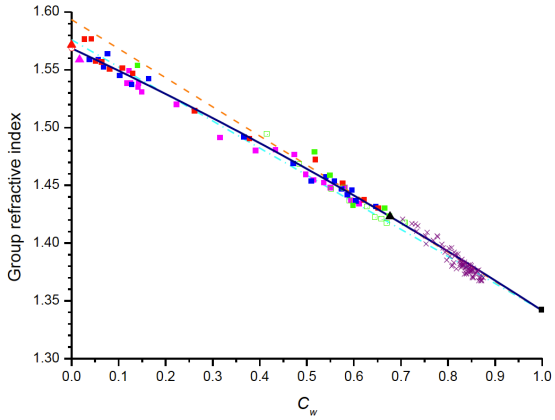

Fig. 6 Group refractive index of RTT fascicles *vs* volume water content C_w. The symbols are the same as in Figure 5. The crosses (×) represent the experimental points for bovine cornea [7] ($\lambda_0 = 819.9$ nm). The solid line (——) and cyan dash-dot (– • –) line represent respectively the approximating quadratic (Eq.9) and linear (Eq.10 with $n_{dry} = 1.576$) polynomials to the data for RTT. The orange dash line (– – –) is the straight line (Eq.10 with $n_{dry} = 1.594$) passing through the points (C_w, n_g)=(1, 1.3416) (water) and (0.677, 1.423) (the average for the native state of RTT).

The experimental data for RTT are well approximated by the quadratic polynomial

$$n_g = 1.5713 - 0.1969C_w - 0.0328C_w^2 \qquad (9)$$

(Fig. 6). The coefficients of this expression were found by the least squares method under the additional conditions that $n_g(C_w)$ must be equal to the group refractive index of water $n_w = 1.3416$ at $C_w = 1$ and to the reliable estimate $n_g = 1.423$ at $C_w = 0.677$ (native state). At $C_w = 0$, approximation (9) gives $n_g = 1.5713$, which is close to the measured values of the group refractive index for the dry state, n_{dry}. We estimated the accuracy of this and subsequent approximations using the parameter $\sigma_{fit} = \sqrt{r_{ss}/n}$, where r_{ss} is the residual sum of squares and n is the number of experimental points. For approximation (9), $\sigma_{fit} \approx 5.4\cdot10^{-3}$. When approximating the experimental data by a linear function

$$n_g = (1 - C_w)n_{dry} + n_w C_w, \qquad (10)$$

which corresponds to the Gladstone-Dale law [23, 31, 32], with given $n_w = 1.3416$, σ_{fit} is minimum (about $6.7\cdot10^{-3}$) when $n_{dry} = 1.576$ (Fig. 6, cyan line). This approximation gives a significantly underestimated value of n_g (1.417) for the native state. The approximation of the RTT data by the straight line passing through the points (C_w, n_g) = (1, 1.3416) (water) and (0.677, 1.423) (native state), the red line in Fig. 6, ensures a rather good accuracy for the range $0.52 \le C_w \le 1$ ($\sigma_{fit} \approx 4\cdot10^{-3}$) but gives a significantly overestimated value for n_{dry} (1.594). The significant deviation of the actual $n_g(C_w)$ curve from this approximating line in the region $C_w \le 0.52$ may be attributed to a change of the mode of hydration. In the literature, two modes of collagenous tissue hydration are distinguished [33-36]. For relatively high values of H ($H > H_c$, where H_c is a critical value, the so-called fibrillar saturation point [35]), changes in the total water content in the tissue lead to changes of the water content in extrafibrillar space while the water content in collagen fibrils remains unchanged [7, 33-36]. In the alternative mode ($H < H_c$), changes in the total water content are accompanied by changes in water content both in collagen fibrils and extrafibrillar space [33-36]. For RTT, $H_c \approx 0.82$ [32, 35], which corresponds to $C_w \approx 0.52$.

Fig. 7 shows the dependence of the phase refractive index n_p of RTT on C_w. The phase refractive index was calculated using approximating function (9) and Eq. (6) on the assumption that

$$\left.\frac{dn_p}{d\lambda}\right|_{\lambda=\lambda_0} = (1 - C_w)\left.\frac{dn_{dry}}{d\lambda}\right|_{\lambda=\lambda_0} + C_w\left.\frac{dn_w}{d\lambda}\right|_{\lambda=\lambda_0}.$$

The values of $dn_{dry}/d\lambda$ and $dn_w/d\lambda$ were calculated from the dispersion data for gelatin [37] and water [29], respectively. We did not find in the literature any reliable experimental data on the wavelength dependence of the phase refractive index of dry collagen in the spectral range under consideration. Gelatin is known to be produced by partial hydrolysis of animal collagen and to have a very similar chemical structure to collagen. For this reason, we used the available data for dry gelatin. For the phase refractive index of gelatin we used the dispersion formula $n = 1.53 + 1788/\lambda_{nm}^2 + 5.73 \cdot 10^8/\lambda_{nm}^4$, where λ_{nm} is the numerical value of the wavelength λ in nanometers [37].

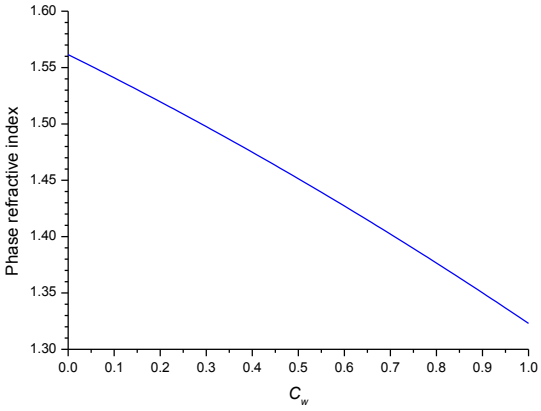

Fig. 7 Tentative estimate of the average phase refractive index of RTT fascicles as a function of volume water content.

5 Conclusion

The average group refractive index of RTT fascicles has been measured as a function of water content using OCT. For the native state, this refractive index has been found to be 1.423 ± 0.003 at a wavelength of 930 nm. In the range $0.52 \le C_w \le 1$, the average group refractive index of RTT fascicles has been found to change almost linearly with C_w. Over the entire range of C_w values, $0 \le C_w \le 1$, the experimental data are well fitted by the quadratic polynomial (9).

Disclosures

The authors declare that there are no conflicts of interest related to this article.

Acknowledgements

The study was supported by the Russian Ministry of Education and Science, Project 3.1586.2017/4.6.

 doi: 10.18287/JBPE18.04.010101

Introduction to the Special Section on Laser and optical technologies in biomedicine and ecology

We are pleased to present the Special Section of the Journal of Biomedical Photonics & Engineering, which focuses on laser and optical technologies for biomedical and ecological applications. The Special Section contains the selected papers from the XV all-Russian Youth Samara conference-contest on optics and laser physics (Samara, November 14-18, 2018) in particular the papers from the Biophotonics Workshop.

The conference-contest on optics and laser physics was organized by P.N. Lebedev Physical Institute (Samara Branch) and Samara National Research University and supported by Russian Foundation for Basic Research (grant No. 17-32-10263), Administration of Samara Region and SPIE Samara Student Chapter. The Special Section of J-BPE introduces you to the major current issues of laser and optical technologies in biomedicine and ecology discussed at the Conference-contest.

The paper of **Elena M. Artemina** and co-authors is devoted to the study of normal and pathologic human skin samples using low-coherence reflectometry and scanning speckle polarimetry. The authors have demonstrated efficiency of the techniques for monitoring of pathological structural changes of human skin as well as the analysis of the influence of immersion clearing agents.

The study of **Andrey A. Leonov** and co-authors has an ecological focus. The authors proposed a new chemosensor structure for registration of metal ions contained in aqueous solutions. A hydrophilic polymer modified by a special ion-sensitive indicator is the base of the device. The presence of metal ions leads to changes in the characteristics of luminescence, providing a sensor response and allows to detect relatively low concentrations of nickel ions in water.

Knowledge of the refractive index of blood is important, for example for simulation of light distribution in the blood-saturated tissues, for diagnostic and dosimetry of that tissues. It is known that blood is extremely turbid medium with high anisotropic factor, scattering and absorption coefficients in the visible region. That's why the development of indirect techniques of determination of blood refractive indexes are actual and practically important. **Ekaterina V. Lazareva and Valery V. Tuchin** presented the technique for modelling of blood refractive indexes on the base of the measured values of refractive indexes of water solutions of haemoglobin and albumin.

Anna V. Neupokoeva and co-authors used the probe microscopy method for 3D analysis of crystallograms of biological fluids after laser impact. The authors studied the effect of laser radiation of different wavelengths and doses on the solution of the Grippoferon and the aqua solution of medical conserved bile. Those solutions were used as model media to confirm the laser effect on the size of macromolecular clusters. Not only qualitative but also quantitative changes of 3D crystallograms after laser impact can be determined using a probe microscope.

Laser hyperthermia with the use of sensitizers is the promising high sensitive technique for tumor destruction. Gold nanorods are used as sensitive agents by **Vadim M. Genin** and co-authors. They studied the heating kinetics in model tumors and surrounding skin depending on the concentration of gold nanoparticles as well as tissue vascularization. The results were directed on the optimization of the nanorods injection procedure into the tumor for its selective and effective destruction.

Development of portable diagnostic fluorimeter, proposed earlier, for detecting the advanced glycation end products in skin is presented in the paper of **Vladimir N. Grishanov** and co-authors. The authors demonstrated that measurements of the skin-scattered radiation in the visible spectral region using pulsed sources of radiation allow to reduce individual variability of the integral diagnostic parameter. Besides, some technical improvements of the fluorimeter were performed.

 doi: 10.18287/JBPE18.04.010101

Thus, the papers of the Special Section demonstrate successful and promising applications of the optical and laser technologies for solution of biomedical and ecological problems.

Special Section Editors:

Aleksandra M. Mayorova, Samara Branch of P.N. Lebedev Physical Institute of Russian Academy of Sciences

Valery P. Zakharov, Samara National Research University

Low-Coherence Reflectometry and Speckle Polarimetry in the Monitoring of Human Skin Pathologic Changes

Elena M. Artemina[1*], Sergey A. Yuvchenko[2], Marina V. Alonova[2], Dmitry A. Zimnyakov[2], and Sergey R. Utz[1]

[1] Saratov State Medical University named after V.I. Razumovsky, 112 Bolshaya Kazachya Str., Saratov 410012, Russia
[2] Saratov State Technical University named after Yu.A. Gagarin, 77 Politekhnicheskaya Str., Saratov 410054, Russia

*** e-mail:** farfalla87@mail.ru

Abstract. We present the results of the study of normal and pathologic human skin using low-coherence reflectometry and speckle polarimetry. The statistical characteristics of local polarisation states in the individual coherence areas (speckles) of the forward scattered laser radiation demonstrate high sensitivity to the pathologic changes of the biotissue morphology in vitro. The analysis of the attenuation rate of the low-coherence reflectometer signal depending on the probing depth provides additional information for the identification of skin morphologic changes and the analysis of the effect of immersion agents on the biotissue optical properties. © 2018 Journal of Biomedical Photonics & Engineering.

Keywords: surface epidermis strip; polarisation diagnostics of biotissues; optical clearing of biotissues; optical coherence tomography.

Paper #3267 received 18 Dec 2017; revised manuscript received 18 Feb 2018; accepted for publication 18 Feb 2018; published online 20 Mar 2018. doi: 10.18287/JBPE18.04.010501. [Special Section. Workshop "Biophotonics" of the XV all-Russian Youth Samara conference-contest on optics and laser physics].

References

1. V. V. Tuchin, Handbook of optical biomedical diagnostics, SPIE Press Bellingham, Washington (2016).
2. V. V. Tuchin, Optics of biological tissues. Methods of light scattering in medical diagnostics, FIZMATLIT, Moscow (2012).
3. D. A. Zimnyakov, M. V. Alonova, E. M. Reshetnikova, E. M. Galkina, S. R. Utz, J. S. Sina, O. V. Angelsky, S. B. Ermolenko, and P. V. Ivashko, "Polarization biopsy in the regime of low forward scattering: a comparative analysis of human skin pathologies," Problems of optical physics and biophotonics SMF-2013: mater. XVII International. youth. sci. shc. on optics, laser physics and biophotonics, 17-25 (2013).
4. A. Fercher, "Optical coherence tomography – development, principles, applications," Zeitschrift für Medizinische Physik 20(4), 251-276 (2010).
5. G. Jarry, E. Steimer, V. Damaschini, M. Epifanie, M. Jurczak, and R. Kaiser, "Coherence and polarization of light propagating through scattering media and biological tissues," Applied Optics 37(31), 7357-7367 (1998).
6. J. Briers, "Laser Doppler, speckle and related techniques for blood perfusion mapping and imaging," Physiological measurement 22(4), R35-R66 (2001).
7. T. K. Lee, L. Tchvialeva, I. Markhvida, H. Zeng, H. Lui, A. Doronin, I. Meglinski, and D. I. McLean, "Polarization Speckles and Skin Applications," Imaging in Dermatology, 77-87 (2016).
8. S. L. Jacques, J. C. Ramella-Roman, and K. Lee, "Imaging skin pathology with polarized light," Journal of Biomedical Optics 7(3), 329-340 (2002).
9. S. L. Jacques, M. R. Ostermeyer, L. V. Wang, and D. V. Stephens, "Polarized light transmission through skin using video reflectometry: toward optical tomography of superficial tissue layers," Proceedings of SPIE 2671, 199-211 (1996).
10. S. R. Utz, S. I. Dovganskiy, and O. D. Odoevskaya, "Use of the method of superficial skin biopsy in dermatological practice," Vestnik dermatologii i venerologii 7, 37-38 (1992) [in Russian].
11. P. V. Novitsky, and I. A. Zograf, Estimation of errors in measurement results, 2th Edition, Energoatomizdat Publishing House, Leningrad (1991) [in Russian].

12. D. A. Zimnyakov, Yu. P. Sinichkin, P. V. Zakharov, and D. N. Agafonov, "Residual polarization of non-coherently backscattered linearly polarized light: the influence of the anisotropy parameter of the scattering medium," Waves in Random Media 11(4), 395-412 (2001).
13. E. M Artemina, S. R. Utz, S. A. Yuvchenko, D. A. Zimnyakov, and M. V. Alonova, "Comparative evaluation of clarifying agents to improve the quality of the far long-wave ultraviolet therapy chronic dermatosis," Saratov Journal of Medical Scientific Research 12(3), 453-458 (2016) [in Russian].

1 Introduction

Optical probing of biological tissues *in vivo* and *in vitro* is presently one of the most intensely developed approaches to the characterisation of morphologic and functional condition of biotissues and its change in the course of therapeutic impact. It is traditional to estimate the local values of optical transport parameters of the tissue (the scattering coefficient, the absorption coefficient, the scattering anisotropy parameter) in the probed region [1, 2]. However, in spite of the euphoria related to the possible application of optical radiation to the morphologic and functional diagnostics of biotissues, it is somewhat restricted by the complexity of interpretation of the resulting empirical data. In the case of probing with coherent or partially coherent radiation (e.g., laser polarimetry or optical coherence tomography), the difficulties are caused by the stochastic interference of the probing radiation in the biotissue, which is a multiply scattering randomly inhomogeneous medium [3-5]). The interference gives rise to speckle modulation of the probe radiation that decreases the signal-to-noise ratio in the process of probing and reduces the biotissue probing depth. Note, that the effect of speckle modulation of the probing laser radiation can play not only a negative role, but also a positive one in the optical biomedical diagnostics. A typical example are speckle correlation methods applied to monitor the microhaemodynamics in biotissues [1, 2, 6, 7-9]. Thus, additional information on the morphologic and functional condition of the biotissue under diagnostics can be extracted not only by analysing the attenuated non-scattered ("coherent") component of the probing radiation and the components caused by low-multiplicity scattering, but also by estimating the statistical and correlation properties of multiply scattered speckle modulated "noise" component.

The aim of the present paper is to develop such approach in application to the monitoring of structural changes of human skin caused by different pathologies using the methods of scanning speckle polarimetry (for skin samples *in vitro*) and low-coherence reflectometry (for skin *in vivo*).

2 Experimental technique

We carried out the experiments *in vitro* and *in vivo* with human skin samples in the normal condition and with different kinds of pathologies. The *in vitro* samples (surface strips of epidermis (SSE)) were taken in the outpatient and inpatient setting of the Clinic of Skin Diseases, Saratov State Medical University named after V.I. Razumovsky from 20 patients with different dermatoses (lichen ruber planus, alopecia, discoid lupus erythematosus, psoriasis, demodicosis, scabies) aged 18-60 years, and from 10 healthy persons aged 20-40 years.

To get the SSE we used the technique described in Ref. [10] that comprises several steps. A drop of medical glue was applied to a microscope slide preliminarily washed in the (1:1) mixture of spirit and ether. The slide was applied to the skin and tightly pressed towards it. In 30 seconds, the slide was carefully removed. The medical autosterile nontoxic Sulphacrylate glue (Institute of Catalysis, Siberian Branch of the Russian Academy of Sciences, Novosibirsk) provided firm adhesion between the slide and the epidermis surface that prevented the skin traumatisation. After stripping, the epidermis fragment appeared to be toughly fixed on the glass forming a firm thin film. The material was multiply taken from the same skin area until the appearance of point bleeding. In the process of the study and after it, no side reactions caused by the use of the glue were revealed.

From 9 to 15 skin strip samples with each type of pathology, 3-5 samples 20-80 μm thick from each person, were prepared. The thickness and the surface area of the samples depended on the specific changes of skin structure caused by the particular pathology, as well as on the localisation of the lesion site and the individual characteristics of the patient. Thus, for the samples of skin affected by psoriasis and discoid lupus erythematosus the thickness amounted to 60-80 μm, and for those with alopecia it was 20-35μm. The rest samples, including healthy skin, possessed the thickness 40-60 μm. Samples of healthy skin were taken from one zone of the body (the inner side of forearm). The surface area of the samples varied from 0.7 to 2 cm^2.

The samples of pathologically changed skin were taken from the patients in the stage of clinical presentations (scabies and demodicosis) or exacerbation of chronical diseases.

A schematic diagram of the laboratory scanning speckle polarimeter is presented in Fig. 1.

As a source of radiation we used the He-Ne laser *1* GN-2P (λ = 633 nm, P = 2 mW, linear polarisation). The focusing of laser radiation on the sample and the subsequent collimation of non-scattered component of the probing radiation was implemented using the telescopic system of two microscope objectives O_1 and O_2 ($8^\times$ and $10^\times$) with conjugate focal planes, in which the studied sample *4* was placed. The polarisation state of the forward-scattered probing radiation output from

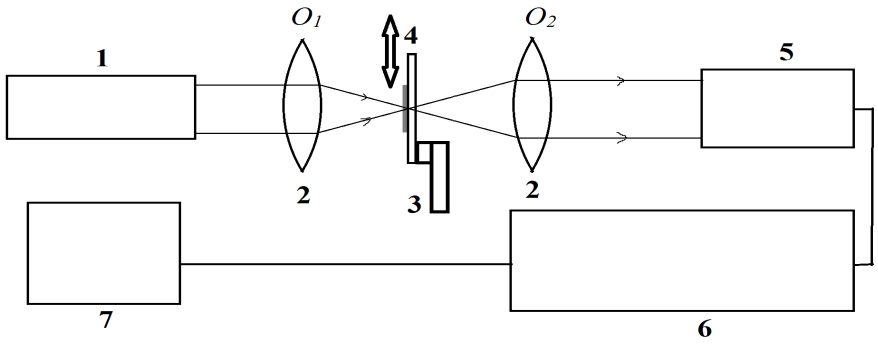

Fig. 1 Schematic diagram of the experimental setup. 1 – He-Ne laser; 2 – telescopic system of two microscope objectives O_1 and O_2; 3 – single-coordinate micropositioner; 4 – sample under study; 5 – measuring head of the polarimeter PAN5710VIS; 6 – polarimeter on the platform TXP 5004; 7 – PC.

the microscope objective O_2 was analysed using the polarimeter TXP5004 – PAN5710VIS (Thorlabs, USA). The optical field in the receiving aperture of the polarimeter head *5* was a superposition of the attenuated non-scattered component and forward-scattered components with different multiplicity of scattering. The used optical scheme allowed the registration of the probing radiation components scattered forward at small angles to the axis of the laser beam. As a result, in the detection zone large-scale speckles were produced, their mean size being comparable with that of the polarimeter photodetector aperture. The scanning was performed with the step 5 μm, which in our case provided the statistical independence of local realisations of the scattered field in the detection zone at each step.

In the scanning speckle polarimetry, the values of excentricity ε_i and azimuthal angle φ_i of the local polarisation ellipses in the analysed region of the scattered light field at each scanning step were used as recorded parameters. The azimuthal angle of the local polarisation ellipse is defined as the angle between the major axis of the ellipse and the polarisation vector in the probing beam. In the used speckle polarimeter the values of the polarisation parameters were determined with the error $\pm 0.01^{\circ}$ for the azimuthal angle and ±0.001 for the excentricity. The sets of ε_i and φ_i values obtained as a result of scanning were subjected to the frequency analysis; besides that using the obtained values the first- and second-order statistical moments were calculated for the excentricity and the azimuthal angle. These parameters were chosen because the obtained empirical distributions of ε_i and φ_i allow clear identification of the contribution of different processes into the formation of local polarisation states of the detected scattered field. In particular, multiple scattering leads to the homogeneous broadening of the azimuthal angle distribution, if the initial non-scattered probing beam is described by delta-function $\rho(\varphi) = \delta(\varphi)$. At the same time, the presence of structural anisotropy or optically active components in the tissue layer will lead to a shift of the distribution relative to the point $\varphi = 0$. Since all obtained results were processed, the possible individual differences were taken into account.

Analogously, the distribution shape for the excentricity of local polarisation ellipses, characterised by negative asymmetry coefficient is determined by the mean multiplicity of scattering of the probing radiation in the tissue layer. The variance of the local excentricity values monotonically grows with the increase of the scattering multiplicity. It is also worth noting that the values of the normalised components of the Stokes vector s_1, s_2, s_3, commonly used as detected parameters in the traditional polarimetry of biotissues can be calculated from the sets of ε_i and φ_i values, obtained in the course of our experiment. On the other hand, the traditional polarimetry based on the characterisation of the probed biotissue using all elements of the Mueller matrix or some part of them, restored from different input and output values of s_1, s_2, s_3, is rather labour-consuming and often makes the resulting data interpretation problematic.

In the clinical studies *in vivo*, the method of low-coherence reflectometry (LCR) was used. The method is based on the quantitative analysis of the attenuation of the mean signal output from a low-coherence interferometer, used to probe the biotissue, depending on the probing depth. As tools for LCR diagnostics one can use various modifications of optical coherence tomographs. In this case, the analysed signal is formed as a result of averaging over a sample of adjacent A-scans in the zone of probing. In contrast to the traditional OCT diagnostics, mainly based on the qualitative comparison of the OCT images with histologic data, the LCR method, as shown below, implies the comparison of the obtained quantitative characteristics of the damped signal with the data on the structure and optical properties of the tissues.

The LCR probing was conducted both with the diagnostic purpose and with the purpose of choosing an optimal immersion agent for optical clearing of superior skin layers in the phototherapy of lichen ruber planus

(LRP). 30 patients with manifestations of LRP aged from 18 to 65 years took part in the study. Different clearing agents (glucose, 1,2-propylene glycol, glycerol, oleic acid) were applied to their skin. We have chosen 4 elements in each individual patient, similar in magnitude and size and located in the same anatomic region (the most frequent localisation of skin rash was the flexion surface of forearm). Then, to enhance the penetration of the clearing agent through the stratum corneum, the affected areas were treated with the solution of ethanol. To enhance the transcutaneous penetration and to prevent the draining, the immersion agent was applied to the elements under occlusion (polyethylene film). The LCR probing was carried out in each element in the process of clearing (in 5-15-30-60 minutes).

As a low-coherence reflectometer, we used the optical coherence tomograph OSC1300SS with frequency sweeping (Thorlabs, USA) having the central wavelength 1325 nm.

3 Experimental results and discussion

In the process of using the scanning speckle polarimetry the sample volumes for the values of excentricity and azimuthal angle of local polarisation ellipses recorded by scanning the skin strips amounted to 1000-2000 values for each skin sample. In the process of the data statistical processing, the frequency analysis was carried out for each scan, after which the obtained distributions of relative frequencies for the values of excentricity and azimuthal angle were averaged over different data sets obtained for one person (see the section "Experimental technique"). In the process of frequency analysis, the number of intervals for grouping the obtained data in the region from the minimal value to the maximal one was chosen to be 18. This value is somewhat smaller than $\sqrt{N}$ (where N is the sample volume), proposed in Ref. [11] as a rational choice of the optimal number of intervals for the frequency analysis. The number of intervals smaller than $\sqrt{N}$ leads to the coarsening of the obtained histograms, and the greater numbers increase the uncertainty related to the possibility of "empty" intervals. Thus, in our analysis we have made a choice in favour of coarser estimates of the distribution of relative frequencies over the intervals. At the next stage of the analysis, the averaged frequency distributions obtained for each patient with the given pathology were averaged over the group of patients possessing this pathology. Thus, in the course of processing the results of speckle polarimetry, the obtained data were averaged twice, first, for each individual and, second, for the group of individuals. To our opinion, such approach essentially enhances the robustness of the obtained empirical data. Note also that the root-mean-square deviations of the minimal and maximal values of the excentricity and the azimuthal angle from the appropriate mean values for one patient did not exceed 20%. For a group of patients the similar quantity amounted to 32%, which is caused by the spread of individual physiologic features of the patients in the group.

For example, Figs. 2 and 3 present the histograms of the local values of excentricity and azimuthal angles of the polarisation ellipses obtained as described above in the samples of normal skin (a) and pathologic (psoriasis) skin *in vitro* (b).

In the samples of skin affected by psoriasis (Figs. 2b and 3b) we can see homogeneous broadening of the azimuthal angle distribution with minor shift towards the region of positive values and the monotonic decrease of the relative frequency of excentricity values, the modal value of the relative frequency being equal to 1. These results are in qualitative agreement with the experimental and theoretical data on the transformation of the polarisation state of light, propagating through isotropic multiply scattering media (see, e.g., [12]).

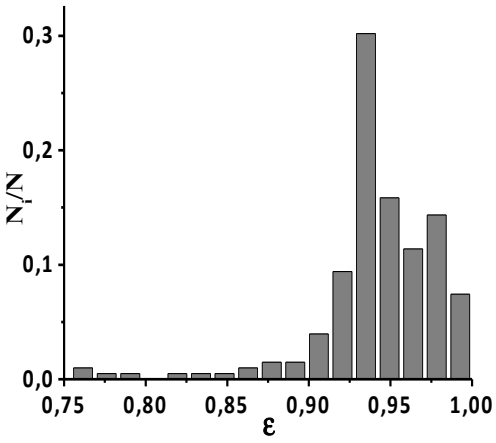

(a)

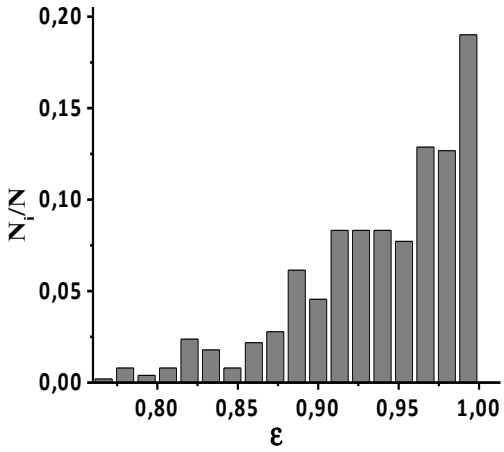

(b)

Fig. 2 Histograms of the local values of the polarisation ellipse excentricity for the epidermis of the *in-vitro* samples of normal skin (a) and the skin affected by psoriasis (b).

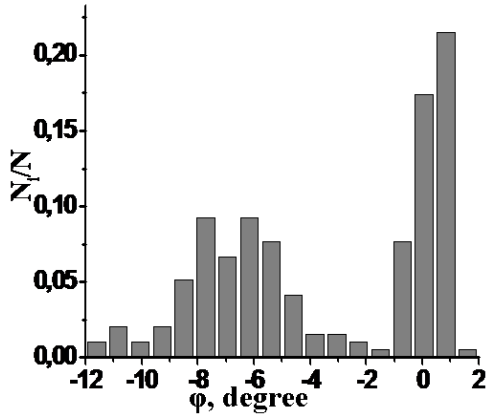

(a)

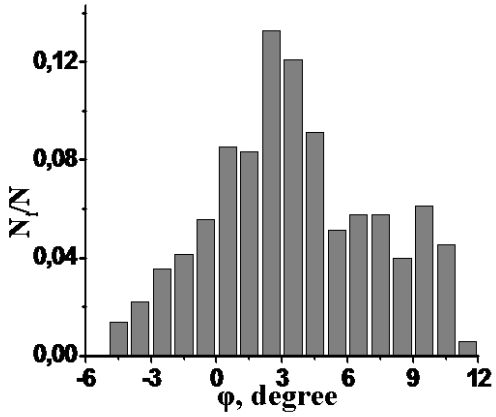

(b)

Fig. 3 Histograms of the local values of the polarisation ellipse azimuthal angle in the epidermis samples of the normal skin *in vitro* (a) and in the case of psoriasis (b).

On the other hand, one can see qualitative differences of the obtained results for the normal skin, namely, the bimodal character of the azimuthal angle histogram with essential shift of the minor mode towards the region of negative values, as well as the shift of the modal value of the excentricity to the region of small values. These features allow us to suppose that such samples possess a certain type of structural anisotropy. This hypothesis requires additional detailed studies.

As quantitative characteristics of the above peculiarities of the frequency distributions of the local values of the excentricity and the azimuthal angle one can consider the mean values $\langle\varepsilon\rangle$ and $\langle\varphi\rangle$. Using this approach the studied samples of skin strips can be divided into two groups. The first group is characterised by symmetric and asymmetric distributions of the azimuthal angle at small $\langle\varphi\rangle$, and for the second group the negative values of $\langle\varphi\rangle$ with sufficiently large absolute value are typical. The samples of skin affected by alopecia are characterised by considerably expressed bimodality of the azimuthal angle frequency distribution at the maximal absolute value of $\langle\varphi\rangle$. The mean excentricity values for the studied samples lie in the interval from 0.92 to 1, and the samples can be confidently divided into two groups, with $\langle\varepsilon\rangle > 0.96$ and with $\langle\varepsilon\rangle < 0.94$.

Such approach to the identification of pathologically affected skin samples *in vitro* using the scanning speckle polarimetry is illustrated by Fig. 4, where the mapping points corresponding to the normal and pathologic skin samples are presented in the coordinate system "mean azimuthal angle - mean excentricity of polarisation ellipse".

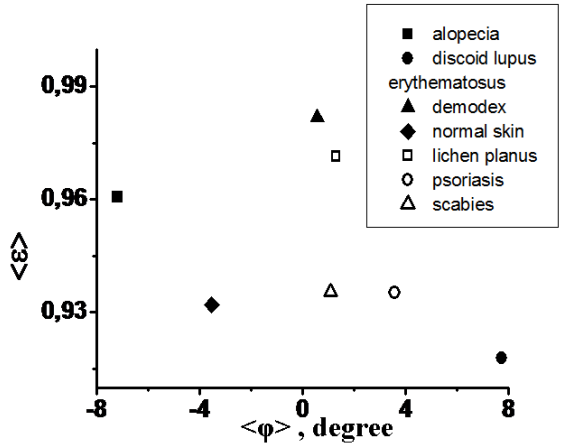

Fig. 4 Mapping of pathologic conditions of human skin epidermis for different diseases in the system of coordinates "mean value of the azimuthal angle - mean value of the polarisation ellipse excentricity" (obtained from the data of speckle polarimetry).

In the case of low-coherence reflectometry of human skin *in vivo* using the optical coherence tomograph as an instrumental base, the analysis of the recorded OCT signals was performed as follows.

At the first stage for the region chosen for probing we determined the damping LCR signal $I_r(z)$ (where z is the probing depth) by averaging over a group of 30 adjacent A-scans recorded by the optical coherence tomograph. As a result of the averaging, the noise speckle modulation of A-scans was reduced to the level acceptable for further analysis. The reconstructed LCR signal is a superposition of diffuse and low-multiplicity scattered components of the probing radiation backscattered by the layer of tissue that can be presented as

$$I_r(z) \approx I_{dr}(z) + I_{sr}(z), \qquad (1)$$

where $I_{dr}(z)$ is the diffuse signal component, $I_{sr}(z)$ is the low-multiplicity scattered component. The

theoretical analysis of the dependence of the diffuse component decrease rate on the probing depth, performed within the frameworks of the diffusion approximation of the radiation transport theory, and the comparison of the obtained theoretical data with the dependence of LCR signals on z observed experimentally have led us to the conclusion that under the used conditions of probing $I_{dr}(z) << I_{sr}(z)$. In turn, the component $I_{sr}(z)$ can be presented in the form

$$I_{sr}(z) \propto Q_{bs}(z)\exp\left(-2\overline{\mu}_t z\right), \qquad (2)$$

where $Q_{bs}(z)$ is the backscattering efficiency factor of the studied tissue at the depth z, $\overline{\mu}_t$ is the biotissue extinction coefficient averaged over the probed volume.

At the next stage of the processing, the exponential trend $\exp\left(-2\overline{\mu}_t z\right)$ was extracted from the LCR signal using the least square method. The value of $\overline{\mu}_t$ was determined for the probed region and the trend was removed according to the procedure $I_r(z)\exp\left(2\overline{\mu}_t z\right) \propto Q_{bs}(z)$. The obtained function is proportional to the depth distribution of the backscattering efficiency factor and can be used both for the quantitative analysis of morphologic features of the biological tissue and for its visualisation. Note that the value of $\overline{\mu}_t$ obtained as a result of trend determination can be also used for the quantitative characterisation of the biotissue in the region of probing.

The application of this approach using the LCR probing of skin affected by lichen ruber planus with tissue clearing by means of 1,2-propylene glycol and without it is illustrated in Fig. 5. Figure 6 presents the depth distributions of LCR signals for the affected skin region before the beginning of optical immersion and in 30 minutes after the application of the immersion agent with the corresponding exponential trends. The immersion was implemented by applying the agent to the surface of the affected region. Figure 6,b shows the reconstructed distributions of the normalised values of the backscattering efficiency factor $Q_{bs}(z)$ (the values were normalised to the maximal value of $Q_{bs}(z)$ in the probed region before the application of the immersion agent). In the reconstructed distributions $Q_{bs}(z)$ one can clearly identify two zones associated with the epidermis and the papillary layer of dermis, characterised by more intense backscattering (at the depths from ≈ 100 μm to ≈ 350 μm and from ≈ 400 μm to ≈ 650 μm).

One more example of the application of the developed approach is the estimation of the efficiency of the skin optical clearing *in vivo* for different biologically harmless immersion agents. In the present case, we estimated the values of $\overline{\mu}_t$ that determine the exponential trend of the recorded LCR signals at different moments of the immersion agent impact. 30 patients with lichen ruber planus took part in the experiment with each immersion agent. Since the values of $\overline{\mu}_t$ obtained from the LCR probing at the initial moment of the optical immersion in different patients lied in the interval from 80 cm^{-1} to 120 cm^{-1} (depending on the age, sex and other factors), for the characterisation of the immersion efficiency we used the normalised values $\overline{\mu}_t(t)/\overline{\mu}_t(0)$, averaged over a group of patients. Figure 6 presents the results of the study of the efficiency of immersion agents that allowed the choice of 1,2-propylene glycol as the most efficient clearing agent for the phototherapeutic applications in dermatology.

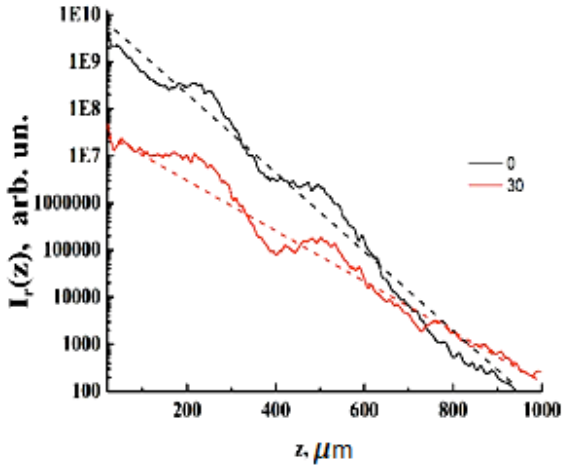

(a)

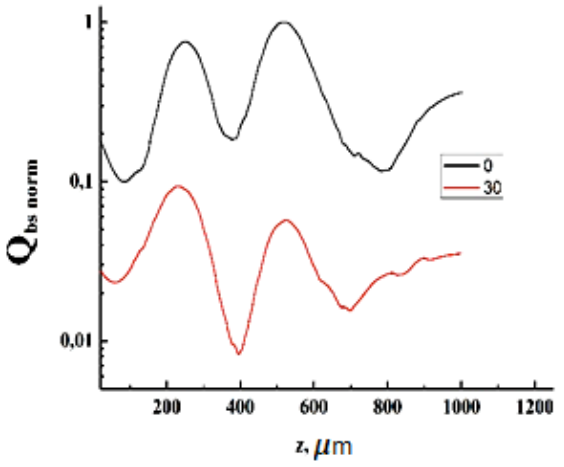

(b)

Fig. 5 The recorded LCR signal (a) and the normalised backscattering efficiency factor (b) versus the probing depth for the skin in vivo affected by the lichen ruber planus. The measurements were executed before the application of 1,2-propylene glycol as immersion agent and in 30 minutes after it.

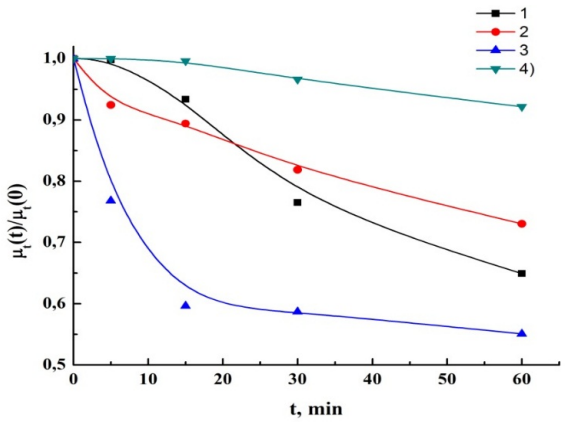

Fig. 6 Dependences of the mean normalised extinction coefficient of human skin in vivo (LRP) on the time of exposure to different immersion agents: 1 – glycerol, 2 – glucose, 3 – 1,2-propylene glycol, 4 – oleic acid. To plot the dependences the obtained data were interpolated by B-splines.

4 Conclusion

It should be emphasised that the performed *in vitro* scanning speckle polarimetry was a pilot study aimed at evaluating the applicability of the method to the identification and characterisation of skin pathologies. Other researchers have also discussed the idea of analysing the polarisation characteristics of multiply scattered speckle-modulated laser radiation for the diagnostics of skin pathologies (in particular, oncologic diseases). In this connection, we should mention the studies by T. Lee *et al.* from the University of British Columbia in Vancouver (see, e.g., [7]). However, the approaches to the interpretation of the obtained data proposed by this group are ambiguous and do not allow for all specific features of the polarisation state evolution in the process of laser radiation propagation through randomly inhomogeneous multiply scattering media.

As to our results obtained using the discussed method of scanning speckle polarimetry of skin samples *in vitro* in the transmitted light, we should note that the comparison of the mean values of excentricity and azimuthal angle of the local polarisation ellipse in the forward-scattered light allows the division of samples into a few groups, presumably related to their morphology. We present the preliminary results of mapping different pathologies on the 2D space of diagnostic parameters, chosen as the first-order statistical moments (mean values) of the excentricity and azimuthal angle of the local polarisation ellipses. These results have demonstrated acceptable selectivity of the approach in the identification of different skin pathologies. Additional facilities can be offered by multidimensional mapping of pathologies in the space of diagnostic parameters, which can be, e.g., the higher-order statistical moments of the local values of excentricity and azimuthal angle, determined in the speckle polarisation experiment.

The method of low-coherence reflectometry used in the present work implies the use of the primary signals (A-scans) of the optical coherence tomograph in order to obtain the information on the biotissue extinction coefficient averaged over the probed volume and the depth distribution of the backscattering efficiency factor. With this aim the recorded set of A-scans were additionally processed in order to suppress the noise components, to determine and eliminate the exponential trend. Note that the approach is interesting not only from the point of view of identifying human skin pathologic changes, but also from the point of view of applying therapeutic procedures based on near-UV irradiation of pathologic skin areas with preliminary optical clearing by means of biocompatible immersion agents (e.g., in therapy of lichen ruber planus [13]). In particular, the application of the approach to the determination of the most efficient clearing agent for the phototherapy of skin pathologies has shown its high efficiency.

Disclosures

All authors declare that there is no conflict of interests in this paper.

Luminescent Chemosensor Systems for Detecting Metal Ions in Aqueous Media

Andrey A. Leonov[1*], Alexander A. Sergeev[1], Alexander Yu. Mironenko[2], and Sergey S. Voznesenskiy[1]

[1] Institute of Automation and Control Processes, Far Eastern Branch of the Russian Academy of Sciences, 5 Radio Str., Vladivostok 690041, Russia

[2] Institute of Chemistry, Far Eastern Branch of the Russian Academy of Sciences, 159 Prosp. 100-letiya Vladivostoka, Vladivostok 690022, Russia

*** e-mail:** andreileonov@inbox.ru

Abstract. The paper deals with the synthesis and study of chemosensor structures for detecting metal ions in aqueous solutions based on a hydrophilic polymer modified by an ion-sensitive indicator. A new ion-sensitive indicator based on the rhodamine 6G luminophore that selectively responds to the presence of nickel ions in aqueous environment is developed. The limit of the nickel ions detection is equal to 0.1 μM.

Keywords: biopolymer; chitosan; optical sensor; sensitive coatings; luminescence; analyte; polymers; metal ions.

Paper #3277 received 15 Jan 2018; revised manuscript received 24 Feb 2018; accepted for publication 26 Feb 2018; published online 20 Mar 2018. doi: 10.18287/JBPE18.04.010502. [Special Section. Workshop "Biophotonics" of the XV all-Russian Youth Samara conference-contest on optics and laser physics].

References

1. L. Prodi, F. Bolletta, M. Montalti, and N. Zaccheroni, "Luminescent chemosensors for transition metal ions," Coordination Chemistry Reviews 205(1), 59-83 (2000).
2. Y. Xiao, Y. Cui, Q. Zheng, S. Xiang, G. Qian, and B. Chen, "A microporous luminescent metal-organic framework for highly selective and sensitive sensing of Cu2+ in aqueous solution," Chemical Communications 46(30), 5503-5505 (2010).
3. L. Prodi, "Luminescent chemosensors: from molecules to nanoparticles," New Journal of Chemistry 29(1), 456-461 (2005).
4. M. Formica, V. Fusi, L. Giorgi, and M. Micheloni, "New fluorescent chemosensors for metal ions in solution," Coordination Chemistry Reviews 256(1-2), 170-192 (2012).
5. F. M. Raymo, and I. Yildiz, "Luminescent chemosensors based on semiconductor quantum dots," Physical Chemistry Chemical Physics 9(17), 2036-2043 (2007).
6. K. Lunstroot, K. Driesen, P. Nockemann, C. Görller-Walrand, K. Binnemans, S. Bellayer, J. Le Bideau, and A. Vioux, "Luminescent Ionogels Based on Europium-Doped Ionic Liquids Confined within Silica-Derived Networks," Chemistry of Materials 18(24), 5711-5715 (2006).
7. A. Prasanna de Silva, T. S. Moodyb, and G. D. Wright, "Fluorescent PET (Photoinduced Electron Transfer) sensors as potent analytical tools," Analyst 134(12), 2385-2393 (2009).
8. R. M. Clegg, "Fluorescence resonance energy transfer and nucleic acids," Methods in Enzymology 211, 353-388 (1992).
9. Y. Jeong, and J. Yoon, "Recent progress on fluorescent chemosensors for metal ions," Inorganica Chimica Acta 381(23), 2-14 (2012).
10. S. Bonacchi, D. Genovese, R. Juris, M. Montalti, L. Prodi, E. Rampazzo, M. Sgarzi, and N. Zaccheroni, "Luminescent Chemosensors Based on Silica Nanoparticles," in Topics in Current Chemistry, vol. 300, L. Prodi, M. Montalti, N. Zaccheroni (Eds), Springer, Berlin, Heidelberg, 93-138 (2010).
11. N. R. Chereddy, K. Suman, P. S. Korrapati, S. Thennarasu, and A. B. Mandal, "Design and synthesis of rhodamine based chemosensors for the detection of Fe^{3+} ions," Dyes and Pigments 95(3), 606-613 (2012).

12. J. Y. Kwon, Y. J. Jang, Y. J. Lee, K. M. Kim, M. S. Seo, W. Nam, and J. Yoonet, "A Highly Selective Fluorescent Chemosensor for Pb^{2+}," American Chemical Society 127(28), 10107-10111 (2005).
13. Y. Zhou, J. Zhang, L. Zhang, Q. Zhang, T. Ma, and J. Niu, "A rhodamine-based fluorescent enhancement chemosensor for the detection of Cr^{3+} in aqueous media," Dyes and Pigments 97(1), 148-154 (2013).
14. Y. K. Jang, U. C. Nam, H. L. Kwon, I. H. Hwang, and C. Kim, "A selective colorimetric and fluorescent chemosensor based-on naphthol for detection of Al^{3+} and Cu^{2+}," Dyes and Pigments 99(1), 6-13 (2013).
15. Z.-C. Liao, Z.-Y. Yang, Y. Li, B.-D. Wang, and Q.-X. Zhou "A simple structure fluorescent chemosensor for high selectivity and sensitivity of aluminum ions," Dyes and Pigments 97(1), 124-128 (2013).
16. M. R. Ganjali, M. Hosseini, M. Motalebi, M. Sedaghat, F. Mizani, F. Faridbod, and P. Norouzi, "Selective recognition of Ni2+ ion based on fluorescence enhancement chemosensor," Spectrochimica Acta Part A: Molecular and Biomolecular Spectroscopy 140, 283-287 (2015).
17. A. Yari, M. B. Gholivand, and F. Rahhedayat, "Development and characterization of a new nickel(II) ion selective optode based on 2-amino-1-cyclopentenedithiocarboxylic acid," Measurement 44(9), 1691-1698 (2011).
18. N. Aksuner, E. Henden, I. Yilmaz, and A. Cukurovali, "A novel optical chemical sensor for the determination of nickel(II) based on fluorescence quenching of newly synthesized thiazolo-triazol derivative and application to real samples," Sensors and Actuators B: Chemical 166-167, 269-274 (2012).
19. H. Li, S.-J. Zhang, C.-L. Gong, Y.-F. Li, Y. Liang, Z.-G. Qi, and S. Chen, "Highly sensitive and selective fluorescent chemosensor for Ni2+ based on a new poly(arylene ether) with terpyridine substituent groups," The Analyst 138(23), 7090-7093 (2013).

1 Introduction

At present, the optical measurement methods allow efficient registration of different heavy metals ions in aqueous solutions [1, 2]. This is due to a number of advantages possessed by these methods, such as short response time, good reproducibility, wide range of determined concentrations, and high resistance to noise electromagnetic fields. One of the widely used ways to organise such sensor systems is to use luminescent indicators [3], which can change their luminescence properties in the presence of the measured substance (analyte). These indicators can be obtained from different chemical compounds, e.g., dyes [4], quantum dots [5], and rare-earth metals [6].

As a rule, the sensor response of such systems is based on the effects of photoinduced electron transfer (PET) and fluorescence resonance transfer (FRET) of the excitation energy. These effects are based on the energy exchange between chemosensitive part of indicator (donor) to luminescence centre (acceptor) that causes the change of acceptor luminescence properties. In dependence of transfer kind, the energy transfer occurs in an own specific way. In the case of PET, after the molecule excitation, the electron is transferred from the highest occupied molecular orbital to the lowest unoccupied molecular orbital, giving rise to luminescence intensity [7]. In the case of FRET, the energy transfer from donor to acceptor can occur without the emission of photons and due to dipole-dipole interactions between the donor and the acceptor, which causes the intramolecular charge transfer [8].

In the case of FRET-based sensors, it is possible to detect the ions Zn^{2+}, Cu^{2+}, Al^{3+}, Cd^{2+} in an aqueous solution using different luminescent indicators based on pyrene, coumarin, anthracene, etc. [9,10]. To detect the Fe^{3+} ions can be used the PET-effect in the rhodamine B luminophore, with achieved detection limit equal to 10^{-6} M/l [11]. Using the same luminophore, one can detect the Pb^{2+} ions in the acetonitrile medium [12], and the Cr^{3+} ions in the aqueous solution with the detection limit 10^{-3} M/l [13].

Basing on the above methods it is possible to obtain chemosensor systems possessing good selectivity, e.g., using the indicator based on the hydroxynaphthalene (naphthol), one can detect Al^{3+} ions with sufficient accuracy even in the presence of other metal ions [14]. The other one chemosensor based on the methyl pyrazinylketone benzoyl hydrazone (MPBH) indicator is able to detect the Al^{3+} ions with the concentration as low as 10^{-7} M/l [15].

At the same time, the determination of metal ion concentrations in aqueous medium by direct use of luminescent indicators in most cases is limited to laboratory conditions studies and is hardly adaptable to the measurements in real environment. Thus, the development of new sensor system that will combine the sensitivity of analytical methods with the possibility to perform measurements under the real conditions is very important.

Here, we report the synthesis and optical and sensor characteristics studies of a new ion-sensitive indicator based on rhodamine 6G. A sensitive element for the luminescent detectors of nickel ions in aqueous solutions based on modification of a thin hydrophilic polymer film with the obtained indicator was developed.

To date there are a very few publications on the development of optical sensors for direct detection of nickel in aqueous media. The detection of nickel ions is mainly implemented in buffer solutions of organic compounds (acetonitrile or dimethylformamide), which are enhancing the efficiency of the analyte ion chelation by the chemosensitive receptor. Thus, the authors of Ref. [16] use the chemosensor based on 2-(1–H-benzo[d]imidazol-2yl)-N-phenyl hydrazine

carbothioamide to detect nickel ions in the buffer solution of acetonitrile with the detection limit of 7.9×10^{-8} M. The method proposed in [16] is simple, possesses good sensitivity and selectivity. Although the studies were carried out in buffer solution, the authors declare the possibility of using this sensor for detecting Ni^{2+} ions in wastewater samples. In Ref. [17], the 2-amino-1-cyclopentene-dithiocarboxylic acid formed the sensitive element of the chemosensor intended for nickel ion detection; the range of determined concentration was from 3.1×10^{-8} to 8.0×10^{-3} M. In Ref [18] was developed the chemosensor based on the 2-{6-(3-methyl-3-mesitylcyclobutyl)-thiazolo[3,2-b][1,2,4]triazol-2-yl}-phenol with the range of determined concentrations from 1.0×10^{-9} to 4.4×10^{-3} M. Both in Ref. [17] and in Ref. [18] the studies of the sensor response were performed in the acetonitrile buffer. In Ref. [19] sensing studies for nickel detection were performed in dimethylformamide buffer solution, obtained limit of detection was equal to 0.01 μM/l.

In contrast to the papers mentioned above, here we perform sensing measurements in simple sodium acetate buffer making no significant influence on the metal ions chelation process and serving only for stabilising the working solution pH level.

2 Materials and methods

Fig. 1 illustrates the process of the rhodamine 6G ion-sensitive derivatives synthesis, which consists in the replacement of the functional O-CH_3 group with a nitrogen-containing ligand. The bonding of this group (N-ligand, Fig. 1) leads to the occurrence of photoinduced electron transfer, that quench the luminescence of the synthesised compound. However, in the case of chelating the metal ion by this group, the photoinduced transfer of electron does not occur, and the synthesised complex becomes luminescent.

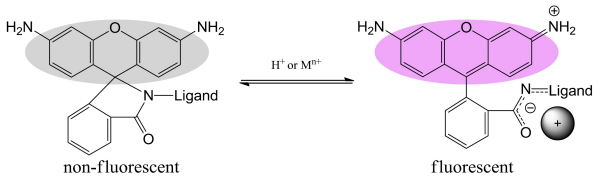

Fig. 1 The general principle of the sensor response formation by the synthesised indicator.

The synthesis of ion-sensitive indicator was performed in two steps. At the first step, we obtained the rhodamine 6G lactam. At the second stage rhodamine 6G lactam was modified with acetylacetone ligand.

To form the high-sensitivity sensor structures, we used 1% aqueous solution of high-molecular chitosan (Sigma) (the deacetylation degree 80%, the molecular mass $\approx10^6$ Da) in 1 % acetic acid. The coatings were deposited on glass substrates with the dimensions 2.5×2.5 cm by solution spin-coating on the Laurell WS-400B-6NPP-LITE device at the angular velocities 1000 revolutions per minute. The coating thickness measured by optical reflectometry technique (on Sentech SE500adv) was about 500 nm. After the deposition, chitosan coatings were annealed during 10 minutes at 150 °C, deprotonated in the 3% ammonia solution, and dried in air. For doping with the indicator, the coatings were immersed in the solution with the component content 0.05 % for 30 minutes. After the sorption, the substrates were carefully washed with deionised water and dried in air.

To study the sensor characteristics of the obtained ion To study the sensor characteristics of the obtained ion-sensitive indicator, we prepared aqueous solutions of salts of different two- and three-valence metals with the concentration 1±0.2 μM. Since the metal salts dissipation in the aqueous medium increased its acidity (lowering the pH level), the measurements in distilled water is related to essential increase of the measurement error. To equalise the experimental conditions in the studies of the sensor response for different metal ions, we prepared the sodium acetate buffer with the pH ≈ 5.6. The sodium acetate buffer (0.2 M) was prepared by mixing 91 ml of the sodium acetate aqueous solution (with the concentration of NaOAc 0.2 M) and 9 ml of the acetic acid aqueous solution with the similar concentration.

The absorption spectra were recorded using spectrophotometer Varian Cary 5000i with 2 nm scanning step and 0.1 s averaging time. The sample was placed perpendicular to the incident light beam.

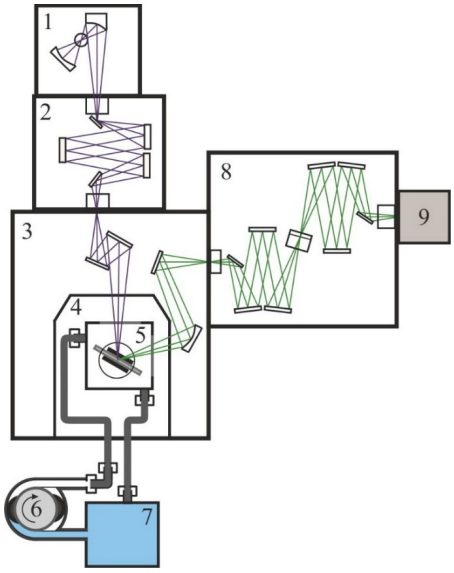

Fig. 2 Block diagram of the spectrofluorimeter Horiba Fluorolog 3 with the designed measurement chamber: 1 – radiation source unit, 2 – exciting radiation monochromator, 3 – unit of focusing the exciting radiation and the luminescence, 4 – measurement section, 5 – hermetic chamber with the fixed sample, 6 – peristaltic pump, 7 – vessel with the analysed aqueous solution, 8 – emission monochromator, 9 – detector.

The fluorescence spectra were recorded using spectrofluorimeter Horiba Fluorolog 3 with 1 nm step and 0.1 s averaging time. The sample was placed at 45° with the exciting radiation beam to provide the maximal signal level.

To perform the measurements under the conditions close to the real ones, we designed and constructed a sealed chamber compatible with the measurement unit of the spectrofluorimeter (Fig. 2). As a radiation source (1) we used the continuous-wave broadband 450 W xenon lamp.

3 Results and discussion

Fig. 3 presents the absorption spectra of the initial rhodamine 6G and ion-sensitive indicator based on it. One can see that after the modification the optical density (directly proportional to the absorption coefficient of substance) and the intensity of luminescence are reduced, which is an evidence of photoinduced transfer of electron from the base part of the rhodamine molecule to the ligand. Rhodamine 6G lactam demonstrates the domination of the absorption peak near 500 nm compared to initial rhodamine peak at 532 nm. Moreover, the rhodamine 6G lactam luminescence spectrum is red-shifted towards by at least 30 nm.

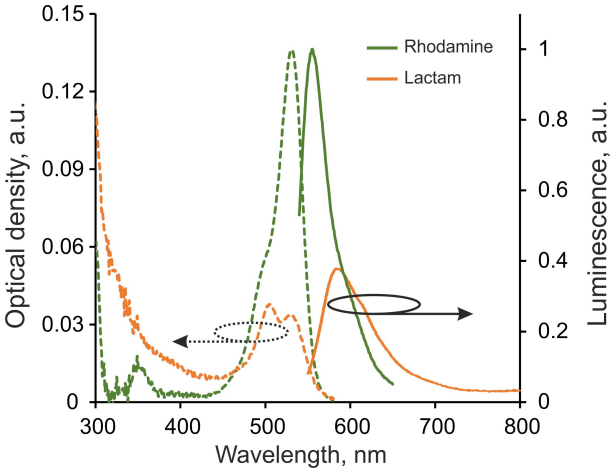

Fig. 3 Spectral characteristics of rhodamine 6G and the ion-sensitive indicator based on it. The dashed and solid lines correspond to the absorption and luminescence, respectively.

Fig. 4 shows the rhodamine 6G lactam luminescence spectra in the presence of various metal ions. One can see that the maximal luminescence intensity increase is observed for nickel ions. Some increase of the luminescence intensity occurs also in the presence of copper and silver, but in this case the luminescence intensity increase is much weaker. This might be due to formation of weak chemical bond between acetylacetone and silver and copper ions which has much lower stability compared to the acetylacetone-nickel complex.

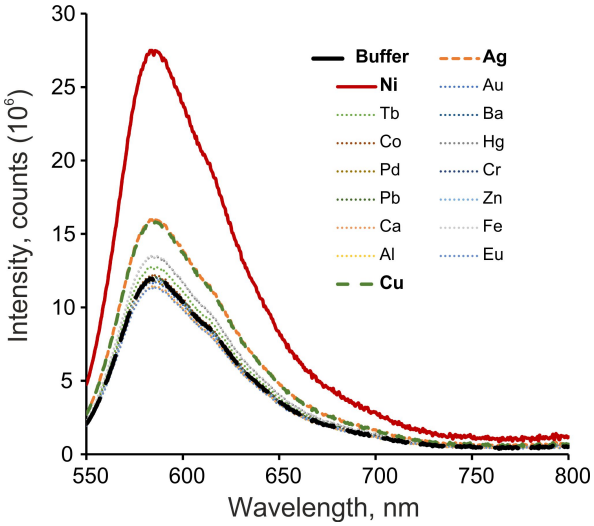

Fig. 4 Intensity of luminescence of rhodamine 6G lactam affected by different metal ions.

The rhodamine 6G lactam luminescence intensity enhancement is proportional to the analyte concentration (Fig. 5). But, one can notice some specific features of the sensor response formation. In the initial state, the rhodamine 6G lactam luminescence is essentially lower than the intensity of luminescence of rhodamine 6G (Fig. 3). The sensor response of the rhodamine 6G lactam is characterised by practically linear growth of the luminescence intensity under the increase of the analyte concentration. This is confirmed by the logarithmic approximation of the dependence of the luminescence intensity on the logarithm of the analyte concentration with the coefficient of determination (R^2) close to unity (Fig. 5(b)). At the same time, the increase of the analyte concentration leads to some changes in the luminescence spectrum of the indicator. Thus, at the analyte concentrations above 1 μM the maximum of luminescence demonstrates $\Delta\lambda \approx 5$ nm blue-shift. Such behaviour can be due to exceeding the ratio 1:1 for the chelated metal ions to chelating groups.

In other words, at low concentrations of metal ions each chemosensitive receptor binds only one analyte ion. Increasing of nickel ions concentration leads to the binding of an additional analyte ion by the chelating centre, which results in occurrence of additional changes of the electron transfer in the indicator molecule. An evidence of this process is also the fact that even at high analyte concentrations (100 μM and higher) no saturation of the sensor response was observed.

The studies of the kinetics of sensor response formation were carried out with the analyte concentration equal to 1 μM (the maximum allowable concentration for nickel amounts to 1.7 μM in the drinking water). Luminescence spectra were recorded every 15 minutes until the luminescence saturation had been achieved. Between the measurements, the studied solution was kept in darkness in order to avoid the possible photodegradation of the luminophore.

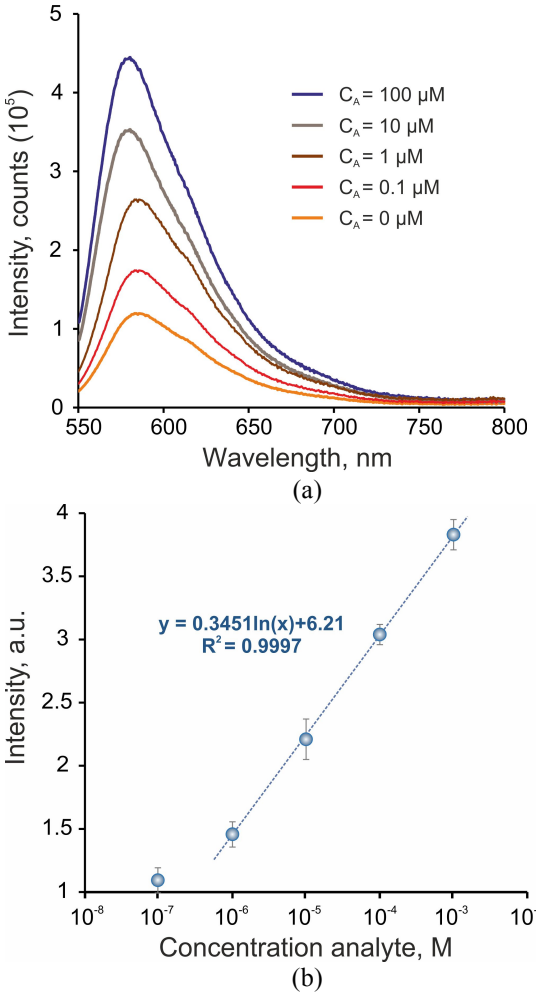

Fig. 5 Sensor characteristics of rhodamine 6G lactam for different analyte concentrations: the luminescence spectra (a) and the sensor response (b).

From the data presented in Fig. 6, one can see that the time of the sensor response formation for rhodamine 6G lactam amounts to about 110 minutes. During this time one can observe sufficiently strong deviations of the luminescence intensity function from the linear dependence (the value of R^2 for the approximation by a linear function differs from unity rather strongly). This effect is, apparently, one more evidence of the process of binding of several analyte ions by one chelating centre.

Alongside with the change of luminescence characteristics during sensor response formation, the changes of the absorption spectra also occur. Thus, increasing of optical absorption at the wavelength of rhodamine 6G excitation ($\lambda \approx 532$ nm) under the increase of the analyte concentration (Fig. 7) is clearly observable. Considering this fact, we can conclude that the luminescence intensity is increasing during the sensor response formation occurs due to greater excitation energy absorption directly by the luminescing part of the rhodamine 6G lactam. This confirms that sensor response formation related to electron transfer changes in the ion-sensitive indicator molecule during the process of analyte chelation.

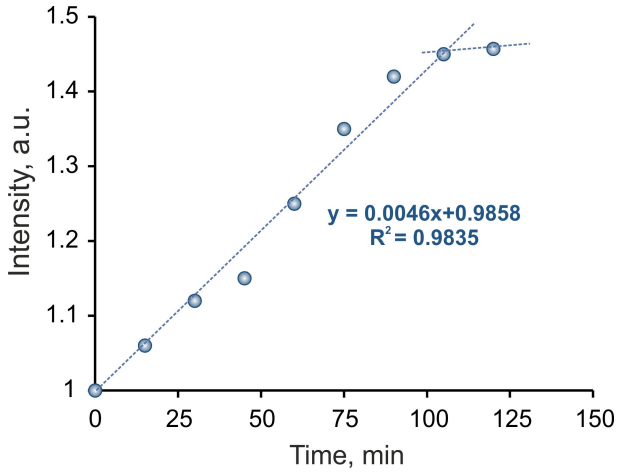

Fig. 6 Time dependence of the luminescence intensity in the rhodamine 6G derivative affected by 1 μM analyte.

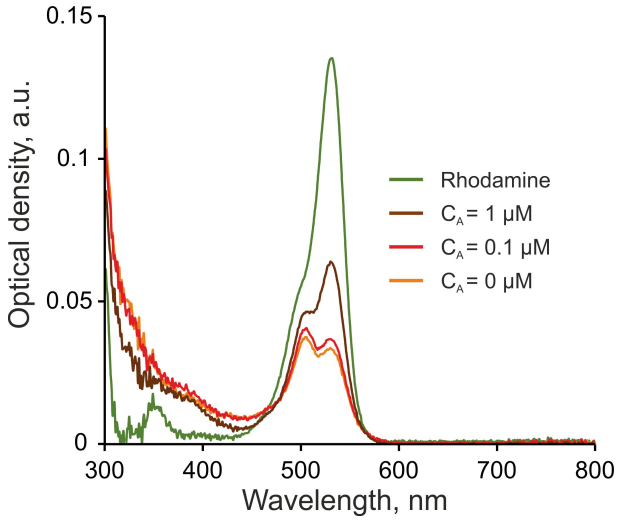

Fig. 7 Optical absorption of the rhodamine 6G lactam affected by different analyte concentrations.

At low analyte concentrations (of the order of 0.1 μM) the uniform increase of the absorption occurs while the initial spectral features of rhodamine 6G absorption (dominance of the absorption band at $\lambda \approx 500$ nm over band at $\lambda \approx 532$ nm) remains unchanged. For the analyte concentrations above 1 μM, the absorption at $\lambda \approx 532$ nm become higher than at $\lambda \approx 500$ nm. That change can determine the rhodamine 6G lactam luminescence spectral changes at high analyte concentrations (Fig. 5 (a)).

4 Conclusion

A new ion-sensitive indicator based on rhodamine 6G chemical modification was obtained. This indicator selectively responds to the presence of nickel ions in the aqueous environment. The sensor response formation occurs due to changes of electronic transfer in rhodamine-derivate molecule under the interaction with nickel ions. The detection limit for the nickel ions is equal to 0.1 μM, which is sufficient for detecting the

nickel ions in drinking water (maximum allowable concentration is 1.7 μM (0.2 mg/l)).

Disclosures

All authors declare that there is no conflict of interests in this paper.

Acknowledgements

The study of ion-sensitive indicator synthesis conditions was supported by the Russian Foundation for Basic Research (grant No. 16-33-60100_mol_a_dk). The studies of luminescence characteristics of sensitive structures in the presence of analyte were supported by the Russian Scientific Foundation (project No. 14-50-00034). The study of absorption spectra changes under the effect of different analyte concentrations was carried out at the expense of the Project ISGZ 0262-2014-0009.

Blood refractive index modelling in the visible and near infrared spectral regions

Ekaterina N. Lazareva[1,2,3*], and Valery V. Tuchin[1,4,5]

[1] Research Educational Institute of Optics and Biophotonics, Saratov State University (National Research University), 83 Astrakhanskaya Str., Saratov 410012, Russia

[2] Center for Functionalized Magnetic Materials (FunMagMa), Immanuel Kant Baltic Federal University, 14 A. Nevskogo Str., Kaliningrad 236041, Russia

[3] Interdisciplinary Laboratory of Biophotonics, Tomsk State University (National Research University), 36 Lenin av., Tomsk 634050, Russia

[4] Laboratory of Laser Diagnostics of Technical and Living Systems, Institute of Precision Mechanics and Control, Russian Academy of Sciences, 24 Rabochaya Str., Saratov 410028, Russia

[5] Samara National Research University, 34 Moskovskoye Shosse, Samara 443086, Russia

*** e-mail:** LazarevaEN@list.ru

Abstract. We present the calculation of blood refractive index based on the experimental data for the real part of the refractive index of the main protein components, haemoglobin and albumin. The refractive index of blood proteins was measured using the multi-wavelength Abbe refractometer at the wavelengths 480, 486, 546, 589, 644, 656, 680, 930, 1100, 1300, and 1550 nm at room temperature +24°C. © 2018 Journal of Biomedical Photonics & Engineering.

Keywords: refractive index; blood; blood components; blood dispersion; visible/NIR wavelengths; Sellmeier formula.

Paper #3278 received 15 Jan 2018; revised manuscript received 14 Mar 2018; accepted for publication 16 Mar 2018; published online 26 Mar 2018. doi: 10.18287/JBPE18.04.010503. [Special Section. Workshop "Biophotonics" of the XV all-Russian Youth Samara conference-contest on optics and laser physics].

References

1. V. V. Tuchin, Tissue Optics: Light Scattering Methods and Instruments for Medical Diagnostics, 3rd Edition, SPIE Press, Bellingham, WA (2015).
2. J. Heijmans, L. Cheng, and F. Wieringa, "Optical fiber sensors for medical applications – Practical engineering considerations," IFMBE Proceedings 22, 2330-2334 (2009).
3. V. V. Tuchin (Ed.), Handbook of Optical Biomedical Diagnostics. Light-Tissue Interaction, vol. 1, 2nd Edition, SPIE Press, Bellingham, WA (2016).
4. A. N. Yaroslavsky, I. V. Yaroslavsky, T. Goldbach, and H.-J. Schwarzmaier, "Optical properties of blood in the near infrared spectral range," Proceedings of SPIE 2678, 314-324 (1996).
5. S. L. Jacques, "Corrigendum: Optical properties of biological tissues: a review," Physics in Medicine and Biology 58(13), 5007-5008 (2013).
6. N. Bosschaart, G. J. Edelman, M. C. G. Aalders, T. G. van Leeuwen, and D. J. Faber, "A literature review and novel theoretical approach on the optical properties of whole blood," Lasers in Medical Science 29(2), 453–479 (2014).
7. J. Wang, Zh. Deng, X. Wang, Q. Ye, W. Zhou, J. Mei, Ch. Zhang, and J. Tian, "Measurement of the refractive index of hemoglobin solutions for a continuous spectral region," Biomedical Optics Express 6(7), 2536–2541 (2015).
8. O. Zhernovaya, O. Sydoruk, V. Tuchin, and A. Douplik, "The refractive index of human hemoglobin in the visible range," Physics in Medicine and Biology 56(13), 4013–4021 (2011).
9. M. Yahya, and M. Z. Saghir, "Empirical modelling to predict the refractive index of human blood," Physics in Medicine and Biology 61(4), 1405–1415 (2016).
10. J. D. Rowe, D. Smith, and J. S. Wilkinson, "Complex refractive index spectra of whole blood and aqueous solutions of anticoagulants, analgesics and buffers in the mid-infrared," Scientific Reports 7, 7356 (2017).

11. Y. L. Jin, J. Y. Chen, L. Xu, and P. N. Wang, "Refractive index measurement for biomaterial samples by total internal reflection," Physics in Medicine and Biology 51(20), 371–379 (2006).
12. D. J. Faber, M. C. G. Aalders, E. G. Mik, B. A. Hooper, M. J. C. van Gemert, and T. G. van Leeuwen, "Oxygen saturation-dependent absorption and scattering of blood," Physical Review Letters 93, 028102 (2004).
13. M. Jedrzejewska-Szczerska, "Measurement of complex refractive index of human blood by low-coherence interferometry," The European Physical Journal Special Topics 222(9), 2367–2372 (2013)
14. Zh. Wang, K.Tangella, A. Balla, and G. Popescu, "Tissue refractive index as marker of disease," Journal of Biomedical Optics 16(11), 116017 (2011).
15. H. Majeed, Sh. Sridharan, M. Mir, L. Ma, E. Min, W. Jung, and G. Popescu, "Quantitative phase imaging for medical diagnosis," Journal of Biophotonics 10(2), 177–205 (2017).
16. G. Mazarevica, T. Freivalds, and A. Jurka, "Properties of erythrocyte light refraction in diabetic patients," Journal of Biomedical Optics 7(2), 244-247 (2002).
17. L. V. Plotnikova, A. M. Polyanichko, M. O. Kobeleva, A. A. Nikekhin, M. V. Uspenskaya, A. V. Kayava, A. D. Garifullin, and S. W. Voloshin, "Analysis of blood serum by the method of refractometry in antitumor therapy in patients with multiple myeloma," Optics and Spectroscopy 124(1), 140-142 (2018).
18. A. N. Bashkatov, E. A. Genina, and V. V. Tuchin, "Optical properties of skin, subcutaneous, and muscle tissues: a review," Journal of Innovative Optical Health Sciences 4(1), 9-38 (2011).
19. F. P. Bolin, L. E. Preuss, R. C. Taylor, and R. J. Ference, "Refractive index of some mammalian tissues using a fiber optic cladding method," Applied Optics 28(12), 2297-2303 (1989).
20. D. K. Sardar, and L. B. Levy, "Optical properties of whole blood," Lasers in Medical Science 13(2), 106-111 (1998).
21. H. Li, L. Lin, and S. Xie, "Refractive index of human whole blood with different types in the visible and near-infrared ranges," Proceedings of SPIE 3914, 517-521 (2000).
22. S. Cheng, H. Y. Shen, G. Zhang, C. H. Huang, and X. J. Huang, "Measurement of the refractive index of biotissue at four laser wavelengths," Proceedings of SPIE 4916, 172–176 (2002).
23. R. Barer, "Refractometry and interferometry of living cells," Journal of the Optical Society of America 47(6), 545–556 (1957).
24. M. V. Volkenshtein, Molecular Optics, Gosteskhizdat, Moscow (1951) [in Russian].
25. D. Segelstein, "The complex refractive index of water," M.S. thesis, Department Of Physics, University of Missouri, Kansas City (1981).
26. N. G. Khlebtsov, I. L. Maksimova, I. V. Meglinski, L. Wang, and V. V. Tuchin, "Introduction to light scattering by biological objects," Chapter 1 in Handbook of Optical Biomedical Diagnostics. Light-Tissue Interaction, 2nd Edition, SPIE Press, Bellingham, WA (2016).
27. W. Heller, "Remarks on refractive index mixture rules," The Journal of Physical Chemistry 69(4), 1123–1129 (1966).
28. G. J. Tearney, M. E. Brezinski, J. F. Southern, B. E. Bouma, M. R. Hee, and J. G. Fujimoto, "Determination of the refractive index of highly scattering human tissue by optical coherence tomography," Optics Letters 20(21), 2258-2260 (1995).
29. H.-C. Cheng, and Y.-C. Liu, "Simultaneous measurement of group refractive index and thickness of optical samples using optical coherence tomography," Applied Optics 49, 790-797 (2010).
30. I. Yu. Yanina, N. A. Trunina, and V. V. Tuchin, "Photoinduced cell morphology alterations quantified within adipose tissues by spectral optical coherence tomography," Journal of Biomedical Optics 18(11), 111407 (2013).
31. J. H. Jung, K. Kim, J. Yoon, and Y. K. Park, "Hyperspectral optical diffraction tomography," Optics Express 24(3), 2006-2012 (2016).
32. Y. K. Park, T. Yamauchi, W. Choi, R. Dasari, and M. S. Feld, "Spectroscopic phase microscopy for quantifying hemoglobin concentrations in intact red blood cells," Optics Letters 34(23), 3668-3670 (2009).
33. F. E. Robles, C. Wilson, G. Grant, and A. Wax, "Molecular imaging true-colour spectroscopic optical coherence tomography," Nature Photonics 5(12), 744-747 (2011).
34. F. E. Robles, L. L. Satterwhite, and A. Wax, "Non-linear phase dispersion spectroscopy," Optics Letters 36(23), 4665-4667 (2011).
35. J. Singh, Optical Properties of Condensed Matter and Applications, Wiley, Chichester, (2006).
36. J. A. Lamasso, "Error in hematocrit value produced by excessive ethylenediaminetetraacetate," American Journal of Clinical Pathology 44, 109-110 (1965).

1 Introduction

Optical properties of blood can be considered in a microscopic or macroscopic way. As a microscopic object, blood is a strongly scattering medium. It is a heterogeneous medium, consisting of plasma and blood corpuscles. The blood plasma consists of 90% water and 10% proteins. The blood corpuscles are mainly red blood cells (almost 99%), leucocytes (1%) and thrombocytes (>1%). The red blood cells possess the largest geometric size, as a rule, 6.2-8.2 μm, and mainly determine the optical properties of blood [1-3]. The quantitative and qualitative information on the blood optical properties, in particular, on the refractive index, is of great interest for many fields of biomedical studies and practical medicine, since the noninvasive or low-invasive optical technologies become wider and wider used in diagnostics and therapy [1-6]. It is well known that the optical properties of blood are determined by such physiologic and biologic parameters as haematocrit, temperature, osmolarity, saturation with oxygen or other gases, membrane rigidity of the red blood cells, and depend on the wavelength in a complex way [1, 4-12]. The visible and near infrared spectral regions are often referred to as "therapeutic/diagnostic window", since just in this wavelength range water, which is a major component of many biological tissues, absorbs weakly. At present there is a revival of interest to the problem of measuring the refractive index of different biological tissues and blood in a wide range of wavelengths, since just the refractive index is proposed for using as an endogenous diagnostic marker of different diseases [13-17]. For example, in Ref. [17] it is shown that the refractive index of blood serum can be used as additional criterion to assess the dynamics of the variation of blood serum properties under the antitumour therapy. The knowledge of the refractive index of blood in a wide range of wavelengths (optical dispersion) is necessary to describe the optical properties of different layers of blood-saturated tissues, e.g., using the Monte Carlo method of statistical modelling [1, 18]. The knowledge of tissue and blood optical properties allows for determination of the optimal wavelength providing the maximal penetration depth of laser radiation. This is important for modelling the interaction between the tissue and laser radiation, e.g., in planning such clinical procedures as laser interstitial heating or photodynamic therapy, as well as in choosing the operating wavelengths of pulse oximeters widely used in different fields of medicine for monitoring the blood oxygen saturation [1-6].

Thus, the determination of optical dispersion of blood and its components in the visible and near infrared spectral regions is an urgent problem, since there are no complete data in the literature. Moreover, the known data on blood refractive index strongly differ among themselves [8-10,19-22], which additionally motivates the studies.

The refractive index is a complex quantity $\tilde{n} = n + ik$; its real and imaginary part can be described within the frameworks of electron theory as [23-25]:

$$n = 1 + \frac{2\pi q^2 N(\omega_0^2 - \omega^2)}{m(\omega_0^2 - \omega^2)^2 + \gamma^2\omega^2}, \quad (1)$$

$$k = \frac{2\pi q^2 N\gamma\omega}{m(\omega_0^2 - \omega^2)^2 + \gamma^2\omega^2}, \quad (2)$$

where q is the molecule charge; N is the number of molecules per unit volume; ω_0 is the natural vibration frequency of the oscillator; ω is the frequency of the external field oscillation; m is the molecular mass; γ is the damping coefficient; n is the real part of refractive index characterising the wave phase shift; k is the imaginary part of refractive index, characterising the wave absorption.

The refractive index of a multicomponent biological medium can be calculated using the Gladstone-Dale law, according to which in the absence of chemical interaction between the components of the medium the resulting refractive index is the average of refractive indices of the components with their volume fractions as weighting factors, i.e., [26,27]

$$n = \sum_{i=1}^{N} n_i f_i, \quad (3)$$

where n_i and f_i are the refractive indices and the volume fractions of individual components, respectively, and N is the number of components.

In a simplified model, the blood can be presented as a two-component medium consisting of red blood cells suspended in plasma. Then Eq. (3) can be applied to the blood in the form

$$n_{blood} = n_{RBC} f_{RBC} + n_{Pl} f_{Pl}, \quad (4)$$

where n_{blood}, n_{RBC}, and n_{Pl} are the refractive indices of blood, red blood cells, and plasma, respectively; f_{RBC} and f_{Pl} are the volume fractions of red blood cells and plasma in the blood, respectively.

Since the plasma consists of 90% water and 10% proteins, the main of which is albumin, its refractive index can be calculated using the Gladstone-Dale formula written in the form:

$$n_{Pl} = 0.9\, n_{Water} + 0.1\, n_{Alb}, \quad (5)$$

where n_{Pl}, n_{Water}, and n_{Alb} are the refractive indices of plasma, water and pure albumin, respectively.

The refractive index of red blood cells can be also calculated using Eq. (3) keeping in mind that haemoglobin, the main protein in the red blood cell, occupies 25% of its volume, and the rest volume is filled with water [1-3]:

$$n_{RBC} = 0.75\, n_{Water} + 0.25\, n_{Hb}, \quad (6)$$

where n_{RBC}, n_{Water}, and n_{Hb} are the refractive indices of the red blood cell, water, and pure haemoglobin, respectively.

Since the blood is a biological extremely turbid medium with high anisotropy of scattering (g = 0.9996) [3], possessing strong scattering and absorption in the visible region, different models of light scattering by particles and other indirect methods are used to determine the refractive index and its dispersion dependence. They include, e.g., the empirical methods based on the calculation of blood refractive index from the experimental values of the refractive indices of the components [10] or the theoretical methods that allow for calculation of the real part of the refractive index from the measured spectra of its imaginary part (absorption spectra) using the Kramers-Kronig relations [10, 11, 12].

Among the direct methods, the most frequently used ones are different modifications of the optical coherence tomography (OCT) [1, 13, 28-33] and phase microscopy [15, 34, 35], the laser refractometer with hollow prism [20, 21], and the methods exploiting the principle of total internal reflection [8, 11, 22]. These methods possess a number of advantages, but are not free of drawbacks. The OCT-based methods allow for refractive index measurements in scattering media, but with the accuracy restricted to 0.01-0.001, which is not always sufficient in analytical applications. However, in the *in vivo* measurements the OCT offers wide possibilities for medical applications, where the above accuracy of the refractive index measurement is sufficient [1, 13, 28-33]. Various modifications of phase microscopy are most frequently used to study the refraction properties of individual cells of blood, e.g., the red blood cells [15, 34, 35]. The application of the laser refractometer with hollow prism allows for refractive index measurement in fluids having large coefficients of scattering and absorption, to which the blood belongs. The method provides *in vitro* measurements with the accuracy to 0.01-0.0001. The drawbacks of the method include the necessity to use laser sources of radiation with relatively high power [20, 21]. The methods based on total internal reflection allow for *in vitro* measurement of the refractive index of blood and its individual components with the accuracy 0.0001-0.00001. The simplicity and the small amount of the required sample material make them available for on-line monitoring of the refractive index [8, 11, 22].

In the present paper, we report the experimental studies of the real part of the refractive index of haemoglobin and albumin, the main protein components of blood. Basing on these data, we calculate the refractive index of whole blood. The refractive index of blood proteins was measured using the multi-wavelength Abbe refractometer for 11 wavelengths in the visible and near infrared ranges at room temperature +24°C.

2 Methods and Materials

For the experimental studies, the haemoglobin solution was prepared from whole blood of a healthy human. The whole blood was collected in test tubes containing heparin to prevent coagulation. The blood sample was centrifuged during 10 min at 2000 rpm to separate the blood into fractions and to separate the red blood cells from plasma and other blood corpuscles. The red blood cells were gathered in a separate test tube, and then their haemolysis was implemented by multiple freezing and defrosting of erythrocyte mass at the temperature −18°C. The haemoglobin concentration in the studied samples was calculated using the spectral method from the absorption spectra and amounted to 260 g/l, which corresponds to the mean haemoglobin concentration in a red blood cell.

To prepare the albumin solution we used the dry human serum albumin (Sigma-Aldrich), dissolved in 0.9% NaCl saline to the concentration of 55 g/l. The obtained concentration corresponded to the mean value of the albumin concentration in the blood plasma.

The refractive index was measured using the multi-wavelength Abbe refractometer (Atago, Japan). In the setup, the source of radiation was a high-power candescent lamp. To select the wavelength we used narrow-band interference filters for 480, 486, 546, 589, 644, 656, 680, 930, 1100, 1300, and 1500 nm. The measurement error introduced by the instrument amounts to ±0.0002.

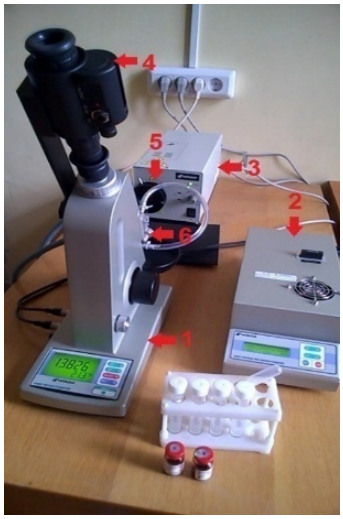

Fig. 1 General view of the experimental setup: 1 – multi-wavelength Abbe refractometer; 2 – power supply; 3 – light source; 4 – special head for measurements in the near IR range; 5 – interference filter; 6 – sample.

In the beginning of every measurement, the calibration of the instrument using the known tabulated value of the refractive index of distilled water was executed. The sample temperature during the measurements was kept to be +24°C by means of water

circulation in the refractometer provided by a thermostat.

The blood refractive index was calculated using Eqs. (4), (5), and (6). The volume fractions of plasma and red blood cells were taken to be 0.55 and 0.45, which corresponds to the haematocrit 45%. The refractive index of pure albumin was calculated using the Gladstone-Dale formula from the measured refractive index of the albumin solution with the concentration 55 g/l:

$$n_{Alb} = (n_{Alb\,sol} - f_{Water}\, n_{Water})/f_{Alb}, \quad (7)$$

where n_{Alb}, $n_{Alb\,sol}$, n_{Water} are the refractive indices of pure albumin, albumin solution and water, respectively; f_{Water}, f_{Alb} are the volume fractions of water and pure albumin in the plasma, respectively.

The refractive index of pure haemoglobin for Eq. (6) was calculated from the measured refractive index of the haemoglobin solution with the concentration 260 g/l:

$$n_{Hb} = (n_{Hb\,sol} - f_{Water}\, n_{Water})/f_{Hb}, \quad (8)$$

where n_{Hb}, n_{Hbsol}, n_{Water} are the refractive indices of haemoglobin in a red blood cell, haemoglobin solution, and water, respectively; f_{Water}, f_{Hb} are the volume fractions of water and haemoglobin in a red blood cell.

The refractive index of blood was approximated by the Sellmeier formula:

$$n^2(\lambda) = 1 + \frac{A1 * \lambda^2}{\lambda^2 - B1} + \frac{A2 * \lambda^2}{\lambda^2 - B2}, \quad (9)$$

where $A1$, $A2$, $B1$, $B2$ are empirical constants. The Sellmeier formula yields the best result for the description of the dispersion curve of a multicomponent system near the absorption band of each component [35].

3 Results and Discussion

The values of refractive index for the haemoglobin and albumin solutions measured at 11 wavelengths of the visible and near infrared range are presented in Table 1. The values of the blood refractive index also presented in Table 1 were calculated using Eq. (4).

Fig. 2 displays the dispersion dependence of the blood refractive index for the calculated values of the refractive index (squares) and the best approximation (red solid line), implemented using the Sellmeier formula (9). As seen from the plot, for the visible and near infrared regions the dispersion of the blood refractive index demonstrates nonlinear behaviour, and the refractive index value decreases with the growth of the wavelength.

After determination of the empirical constants, the Sellmeier Eq. (9) takes the form

$$n^2(\lambda) = 1 + \frac{0.83423 * \lambda^2}{\lambda^2 - 10775.44775} + \frac{0.04296 * \lambda^2}{\lambda^2 - 6.13587 * 10^6}. \quad (10)$$

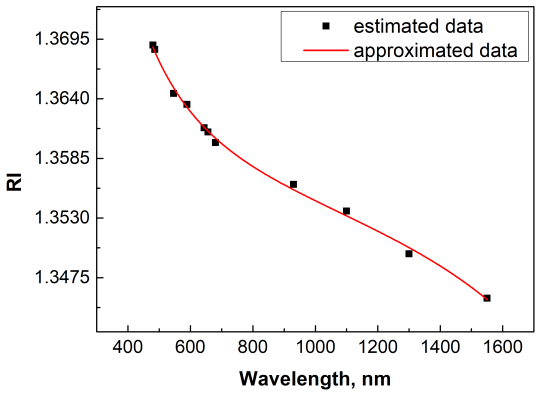

Fig. 2 Dispersion curve of blood refractive index.

The correlation coefficient for fitting of experimental data to the Sellmeier formula equals $R^2 = 0.99$.

Fig. 3 presents the comparison of the refractive index obtained in the present paper with those found in the literature [9, 19-22].

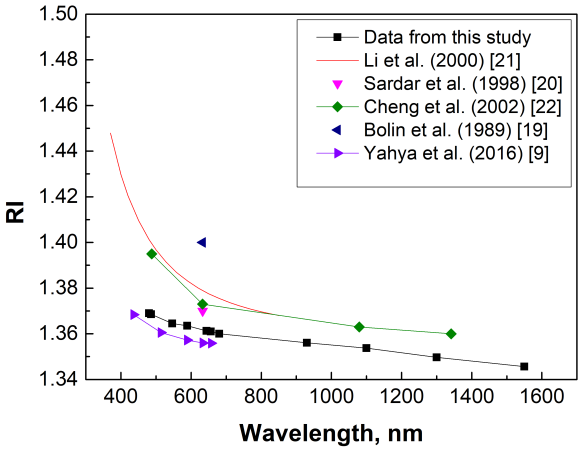

Fig. 3 Dispersion curve of blood in comparison with the data from literature

As already mentioned above, the measurement of blood refractive index is a complex problem solved using complementary direct and indirect methods. The advantage of direct methods is the measurement of the refractive index in the presence of all blood components. However, the inhomogeneity of the cell suspension medium, the strong absorption and scattering do not allow for measurement of whole blood using a direct method with high accuracy, so that the values of the refractive index can strongly differ depending on the sample condition and measurement

Table 1 Refractive indices of haemoglobin and albumin solutions measured at temperature +24°C and of blood calculated using these measurements.

Wavelength, nm	Refractive index of haemoglobin solution in water (260 g/l)	Refractive index of albumin solution in water (55 g/l)	Refractive index of blood
480	1.3945 (±0.0002)	1.3480(±0.0002)	1.3690(±0.0002)
486	1.3939(±0.0002)	1.3478(±0.0002)	1.3686(±0.0002)
546	1.3885(±0.0002)	1.3449(±0.0002)	1.3645(±0.0002)
589	1.3880(±0.0003)	1.3434(±0.0002)	1.3635(±0.0002)
644	1.3854(±0.0003)	1.3416(±0.0002)	1.3613(±0.0002)
656	1.3849(±0.0004)	1.3414(±0.0002)	1.3610(±0.0002)
680	1.3837(±0.0002)	1.3405(±0.0002)	1.3600(±0.0002)
930	1.3782(±0.0005)	1.3380(±0.0004)	1.3561(±0.0003)
1100	1.3751(±0.0006)	1.3361(±0.0003)	1.3537(±0.0003)
1300	1.3707(±0.0004)	1.3325(±0.0004)	1.3497(±0.0003)
1550	1.3665(±0.0005)	1.3285(±0.0004)	1.3456(±0.0003)

technique. The results of direct measurement of blood refractive index are also affected by two additional important phenomena, the aggregation and sedimentation. The necessary usage of anticoagulants can lead to the deformation of some blood corpuscles, which affects the optical properties. For example, it is known that the use of heparin can change the size and shape of thrombocytes and leucocytes, and the excess amount of K_2EDTA can be hypertonic and lead to osmotic stress. The sedimentation is related to the fact that the density of blood cells is higher than the density of plasma and saline. Although the sedimentation rate in normal blood is not high (up to 30 mm/h), it can be essential in the long-time measurements of the sample optical properties [3, 36]. Bolin *et al*. obtained the value of blood refractive index equal to 1.400 using a fibre-optical laser refractometer at the wavelength 632.8 nm [19]. Sardar *et al*. measured the refractive index of a few concentrations of the diluted solutions of whole blood by means of the laser refractometer with hollow prism. Thus, for the 60% blood solution they found the refractive index 1.37 at the wavelength 632.8 nm [20]. Li *et al*. performed the refractive index measurement in the samples of different groups of blood (O(I), A(II), and B(III)) using the method based on the principle of total internal reflection; they presented a dispersion formula for calculating the averaged refractive index of blood in the visible and near infrared spectral region. According to this formula, they determined the value of refractive index 1.4480-1.3680 for the wavelength range 370-850 nm [21]. Cheng *et al*. measured the refractive index of the whole blood using the method of total internal reflection with several lasers. They obtained the following values of the refractive index: 1.395 for 488 nm, 1.373 for 632.8 nm, 1.363 for 1079.5 nm, 1.360 for 1341.4 nm [22].

The modelling methods allow for reconstruction of blood refractive index in a wide range of wavelengths without considering the medium inhomogeneity from the known data for each of its components. In the present paper, using the modelling method with the values of albumin and haemoglobin refractive index measured by means of refractometry, we obtained the values of blood refractive index 1.3690-1.3456 for the wavelength range 480-1550 nm. Recently Yahya *et al*. presented the calculation of the real part of refractive index at different haemoglobin concentrations, temperatures, and wavelengths basing on the experimental values of refractive index of dry haemoglobin aqueous solutions, measured by means of the Abbemat refractometer. For example, at room temperature, for the haemoglobin concentration of 150 g/l, and the wavelengths 436.1, 513.9, 589.1, 633.2, and 657.2 nm they found the values of blood refractive index 1.36481, 1.36053, 1.35724, 1.35601, and 1.35587, respectively [9]. The values of the refractive index obtained in the present paper do not strongly differ from those of Ref. [9], which can be seen in Fig. 3. The discrepancies can be due to the difference in the preparation protocols of blood samples and blood components, the specific features of experimental setups and modelling methods.

The results of the study show that the proposed method of modelling the refractive index in

multicomponent media is suitable for the calculation of blood refractive index in the visible and near infrared spectral regions and can be used for express estimates of blood refractive index. The obtained data complete well the ones already reported in the literature and are important for the calculations of light distribution in blood-saturated tissues, interpretation of results of optical coherence tomography, fluorescence diagnostics, diaphanoscopy in the near infrared spectral region, as well as for providing precision dosimetry in photodynamic therapy and laser thermotherapy.

4 Conclusion

The present study demonstrates the possibility of blood refractive index modelling based on the measured values of refractive index of albumin and haemoglobin aqueous solutions. For the dispersion dependence of blood refractive index, we obtained the coefficients that allow for data extrapolation by the Sellmeier formula in the visible and near infrared wavelength range. The results agree well with the known literature data and can be used in further study of dispersion in biological media.

Disclosures

The authors have no relevant financial interests in this article and no potential conflicts of interest to disclose.

Acknowledgments

The authors are grateful for the support of this work within the 5 top 100 Russian Academic Excellence Project at the Immanuel Kant Baltic Federal University (ENL), and the Research Programme of the Institute of Precision Mechanics and Control of RAS (VVT).

Probe microscopy of biological fluid crystallograms after laser impact

Alexander N. Malov[1], Sergey A. Nebogin[1], Anna V. Neupokoeva[2*], and Andrey A. Vaychas[3]

[1] Irkutsk National Research Technical University, 83 Lermontova Str., Irkutsk 664074, Russia

[2] Irkutsk State Medical University, 1 Kracnogo Vosstaniya Str., Irkutsk 664003, Russia

[3] Irkutsk Branch of Moscow State Technical University of Civil Aviation, 3 Kommunarov Str., Irkutsk 664047, Russia

*** e-mail:** Annett_2005@inbox.ru

Abstract. We consider the probe microscopy of crystallograms of biological fluids as a method of revealing structural changes in them under the impact of laser radiation. The experimental data on the influence of laser radiation with different wavelengths on the structure of crystallograms of biological solutions are presented. © 2018 Journal of Biomedical Photonics & Engineering.

Keywords: biological liquid; solution; laser; crystallogram; probe microscopy.

Paper #3275 received 15 Jan 2018; revised manuscript received 14 Mar 2018; accepted for publication 14 Mar 2018; published online 31 Mar 2018. doi: 10.18287/JBPE18.04.010504. [Special Section. Workshop "Biophotonics" of the XV all-Russian Youth Samara conference-contest on optics and laser physics].

References

1. A. V. Kartelishev, A. G. Rumyancev, A. R. Evstigneev, A. V. Geiniz, and S. V. Usova (eds.), Lazernaya terapiya i profilaktika, Prakticheskaya meditsina, Moscow, Russia (2012). [in Russian]. ISBN 978-5-98811-219-8.
2. T. I. Karu, L. V. Pyatibrat, S. F. Kolyakov, and N. I. Afanasyeva, "Absorption Measurements of Cell Monolayers Relevant to Mechanisms of Laser Phototherapy: Reduction or Oxidation of Cytochrome c Oxidase Under Laser Radiation at 632.8 nm," Photomedicine and Laser Surgery 26(6), 593-599 (2008).
3. S. V. Moskvin (ed.), Osnovy lazernoy terapii. Seriya "Effektivnaya lazernaya terapiya", Triada, Tver, Russia, (2016). [in Russian]. ISBN 978-5-94789-738-8
4. A. V. Finkelshtein, and O. B. Ptitsyn (eds.), Fizika belka., KDU, Moscow, Russia (2002). [in Russian]. ISBN 5-8013-0150-X.
5. V. D. Lakhno (ed.), Klastery v fizike, khimii, biologii, NITs «Regulyarnaya i khaoticheskaya dinamika", Izhevsk, Russia (2001). [in Russian]. ISBN 5-93972-060-9
6. N. Yu. Ilyasova, A. V. Kupriyanov, and A. G. Khramov, Informatsionnye tekhnologii analiza izobrazheniy v zadachakh meditsinskoy diagnostiki, Radio i svyaz', Moscow, Russia (2012). [in Russian]. ISBN: 5-89776-014-4.
7. E. G. Rapis, "Self-assembly of cluster protein films (allotropic nonequilibrium noncrystalline modification) during the process or their condensation," Technical Physics 45(11), 121-131 (2000).
8. E. G. Rapis, "Properties and symmetry of the solid cluster phase of protein," Technical Physics 46(10), 1307-1313 (2001).
9. E. G. Rapis, "A change in the physical state of a nonequilibrium blood plasma protein film in patients with carcinoma," Technical Physics 47(4), 510-512 (2002).
10. Yu. Yu. Tarasevich, "The models and mechanisms of the dehydration self-organization of biological fluids," Physics-Uspekhi 47(7), 717-728 (2004).
11. Ya. M. Vakhrushev, and N. A. Khokhlacheva, "Possibilities of using the crystal optical properties of bile in early diagnostics of cholelithiasis," Eksperimental'naya i klinicheskaya gastroenterologiya 4, 26-30 (2011). [in Russian].
12. A. I. Andryushkin, S. P. Sapozhnikov, and A. V. Karpunina, "Crystallography of biological fluids (a review)," Vestnik Chuvashskogo Universiteta 3, 355-359 (2013). [in Russian].
13. M. A. Petrovskaya, K. A. Kurbatova, and M. B. Belyakova, "Assessment of different-origin conditioned media quality by means of crystal morphology method," Mediko-biologicheskiye, klinicheskiye i sotsialnye voprosy zdorovya i patologii cheloveka. Materialy III Vserossiyskoy obrazovatelno-nauchnoy konferentsii studentov i

molodykh uchenykh s mezhdunarodnym uchastiyem v ramkakh XIII oblasnogo festivalya "Molodye uchenye – razvitiyu Ivanovskoy oblasti", 8-9 (2017). [in Russian].
14. A. N. Malov, A. Yu. Seteikin, A. V. Neupokoeva, E. S. Musatova, I. E. Golub, L. V. Sorokina, V. S. Fetschenko, and A. A. Vaichas, "The laser radiation action on the biological objects," Optik 124(23), 6034-6041 (2013).
15. A. N. Malov, A. A. Vaychas, and E. N. Novikova, "On the mechanism of the gallstone nucleus formation and the impact of laser radiation on its growth," Journal of Biomedical Photonics & Engineering 3(2), 020306 (2017).
16. A. N. Malov, A. V. Neupokoeva, and A. Y. Sambyalova, "Diagnostics of liquid properties by the example of bioorganic solutions," Journal of Biomedical Photonics & Engineering 2(1), 010304 (2016).

1 Introduction

At present considerable experimental material is accumulated, that confirms the biostimulating effect of laser radiation [1-3]. However, the mechanisms of stimulating effect and the processes that allow the response of the entire organism to the local action of laser radiation remain poorly studied. The authors of the present paper propose to consider the blood protein complexes as a universal acceptor of laser radiation. It is known [4, 5] that macromolecules in solutions form the so-called clusters, i.e., associates that can comprise tens of molecules. The biological activity of a molecule incorporated in a cluster considerably differs from that of a single molecule, since its active centres can be overlapped by neighbours, and a molecule inside the cluster is not able to interact with the environment at all. The smaller are the clusters, the larger is their relative surface and the higher is the reactivity of the molecules that form the cluster.

If we suppose that the laser radiation interacting with protein clusters causes their disintegration into smaller associates, then we can propose a number of hypotheses on the possible mechanisms of biostimulation. First, the disintegration of clusters and the change of conformation of protein molecules without the disturbance their primary structure allows the explanation of the increased enzymatic activity, the improvement of oxygen transfer, and other effects at the site of laser impact. Second, the transfer of macromolecules "activated" by laser radiation in the composition of blood plasma can be considered as a mechanism of generalisation of the laser effect on the organism as a whole. Third, the presence of clusters having various sizes and configurations provides the absorption in a wide wavelength range, which makes it possible to explain why the biostimulating effect of laser radiation weakly depends on the wavelength [2].

However, the study of laser radiation effect on the structure and activity of macromolecular complexes directly in the organism is a hardy solvable problem, since it requires considering too many factors (the interaction of laser radiation with medical preparations in the blood, the influence of vascular pathologies on the propagation of "exposed" blood, the presence of accompanying diseases). Therefore, to confirm the laser effect on the size of macromolecular clusters we have to use a model medium reflecting the specific features of biological fluids and, at the same time, available for *in vitro* experiments. With these requirements taken into account, we have chosen the solutions of Grippferon and bile as model media.

To estimate the changes occurring under the impact of laser radiation in biological-like fluids we used the method of crystallogram analysis as one of the simplest methods of structure change diagnostics. The crystallograms of biological fluids are formed at the expense of dehydration self-organisation of the solutions of proteins and other substances [6-12] in the process of drop drying on a solid substrate. It is established that the patterns appearing in this case correlate well with the evidences of diseases in patients [6, 9, 11, 12]. The possibility to apply the crystallogram analysis method for assessing the quality of conditioned media, i.e., the nutritive media containing the waste products of cells preliminarily cultivated in them, is also discussed. Such media are considered as potential drugs for regeneration medicine [13].

Therefore, the method of crystallogram analysis can be used to detect the changes that occur in biological fluids under the impact of laser radiation. In Ref. [14], the possibility of detecting the laser-induced changes in the blood serum and plasma was demonstrated. The possible mechanism of the induced changes is related to the size reduction of the clusters of bioorganic molecules (first of all, macromolecules) caused by laser radiation [14].

Usually crystallograms are analysed using an optical microscope. The geometric dimensions (transverse and longitudinal) of the characteristic patterns of the crystallogram are commonly estimated, while the relief (surface profile) of the patterns is usually lost.

The aim of the present paper is to get information on the three-dimensional crystallogram pattern and to estimate the changes that occur in the structure of liquid media (biological-like fluids) subjected to laser irradiation with different wavelengths by analysing the crystallograms using the probe microscopy method.

2 Materials and methods

As mentioned above, the possible mechanism of biological fluid changes induced by laser radiation is related to the reduction of the size of bioorganic molecular clusters, therefore, for study we have chosen biological-like media containing organic molecules and,

first of all, macromolecules. If for the chosen objects of study the probe microscopy analysis of crystallograms shows the presence of changes in the their three-dimensional structure and the results agree with earlier optical microscopy ones, then we are able to make more definite statements on the reliability of earlier proposed mechanism and its universal character.

One of the chosen objects of study was Grippferon solution. The main component of this solution is interferon alfa-2b, the protein-nature factor that provides antivirus immunity.

The other object of study was 20% aqueous solution of medical conserved bile, consisting of natural bovine and porcine bile, as well as auxiliary substances (rectified ethanol, formalin, and spirituous solution of Furacilin). The natural bile itself contains cholesterol, bile acids and their salts, phospholipids, conjugated bilirubin, protein, and inorganic ions.

It is worth noting that the results of the study of the laser radiation effect on the processes of crystal formation in volume colloidal and gel-like media by the example of human bile have been already presented in Ref. [15]. Initially the bile crystallisation after the laser impact was studied with the purpose to clarify the possibility of using the laser radiation for preventing crystal formation in hepatobiliary system. The results obtained at that time allowed an idea that the laser radiation affects the processes of crystal formation only in the volume of white bile. No effect of laser radiation was detected in the volume of natural pigmented bile. Probably, this was because the presence of pigment caused sufficiently strong absorption of the radiation in a thin layer of bile near the cuvette walls and the radiation did not penetrate into the volume. It was found that the morphology of bile crystallograms depends on the absence or presence of destabilisation of the bile colloidal structure, its stage, and the remoteness of the appearance of biliary pathology symptoms [11].

To eliminate the influence of the abovementioned factors on the process of crystal formation we used the medical conserved bile (pigmented bile). To enhance the penetration of radiation into the bile volume, we studied its 20% aqueous solution.

The crystallograms of the corresponding solutions were studied before and after the impact of laser radiation.

The crystallograms were prepared in the following way. We applied a drop of the studied liquid (the samples to be exposed to laser radiation and the control ones) on the defatted glass substrate and kept dust-protected at room temperature 20-25ºC and relative air humidity 65-70% during 18-24 hours to obtain dry films, i.e., the crystallograms. Then these crystallograms were studied using the scanning probe microscope **NT-MDT Solver**. The contact scanning mode was used.

The Grippferon solution in the cuvette was exposed to laser radiation (having the wavelength 650 nm or 530 nm and the intensity about 80 mW/cm^2) during 1, 2, 5, and 10 minutes. The aqueous bile solution was exposed to the radiation of a semiconductor laser with the wavelength 650 nm during 2 minutes, the power density of radiation being about 250 mW/cm^2.

Then using the probe microscope, we constructed 3D models of the crystallogram relief. Separately three parallel sections of the relief were plotted as the segment height dependence on the coordinate. To estimate the changes of a crystallogram segment size in each section numerically, the minimal and maximal height was found, and their difference divided by two was taken as the mean height of the layer. The segment size was determined by averaging the widths of all "peaks" at the height, equal to the mean height of the layer. Note that the described procedure of numerical estimations allows one to assess on the qualitative changes, but is not sufficient to construct correct numerical dynamics, since it considerably reduces the information volume inherent in the 3D model and is expected to give rise to essential variance of the estimate. Therefore, in the present paper the measurement error was not estimated.

3 Results

The 3D models of the crystallogram relief, obtained by means of probe microscopy, are presented in Figs. 1 and 2. Figure 1 presents the results for the Grippferon solution.

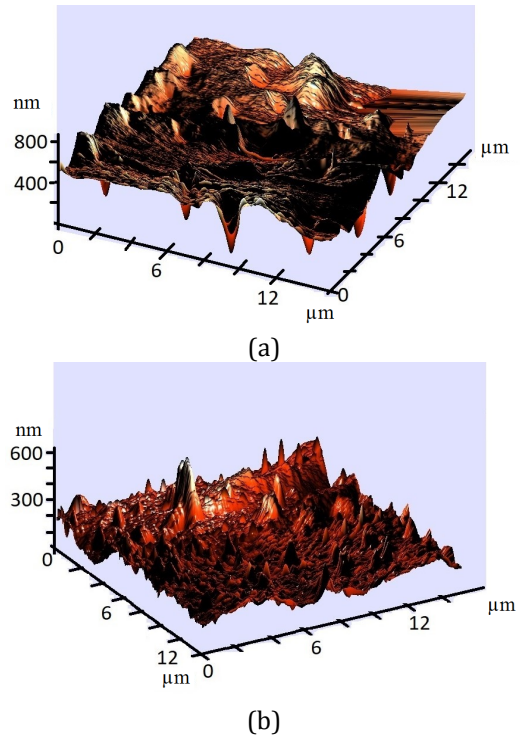

Fig. 1 3D model of the crystallogram relief for the Grippferon solution. (a) – before the impact (control); (b) – In 10 minutes after the impact (the wavelength 530 nm, the total energy density 48 J/cm^2).

As a result of laser irradiation with the wavelength 530 nm, the decrease of the characteristic size of the pattern was observed already in 5 minutes of the

exposure (the total energy density 24 J/cm^2), and after 10 minutes of exposure the size of the inhomogeneity decreased by two times. Besides that, the mean height of the layer (the level above which the peaks rise), as seen from Fig. 1, amounts to about 500 nm for the control solution and nearly 250 nm for the exposed solution. Similar results were obtained for the action of the laser radiation with the wavelength 650 nm, namely, the changes of the crystallogram characteristics size also began from 5 minutes of exposure, but the change relative to the initial size was smaller. To our opinion, higher efficiency of green irradiation is due to the greater energy of quantum that allows greater energy transfer to the clusters and more efficient destruction of the bonds stabilising them.

It is worth attention that the crystallograms were obtained at discrete moments of time, i.e., the laser exposure time changed stepwise. At small values of the exposure time (less than 5 minutes), both the visual and the numerical estimation showed insignificant changes. On the contrary, in the crystallograms obtained from the liquid after 10 and more minutes of laser exposure the changes were significant as compared to the control samples, but slightly differed from each other. Thus, under the conditions of our experiment one can conclude that the changes occur abruptly and correspond to the exposure time of nearly 5 minutes. Therefore, the threshold energy density can be assessed to equal 20-25 J/cm^2, independent of the wavelength. The present result agrees well with the estimates obtained from the crystallogram studies using optical microscopy [16].

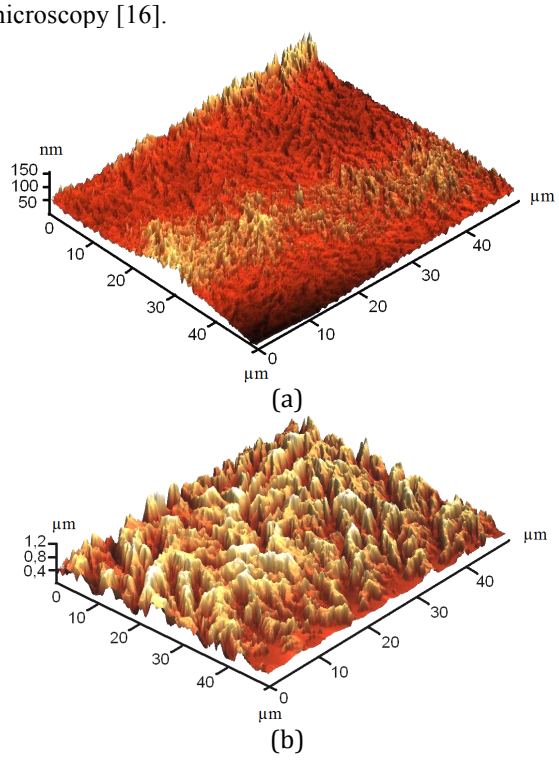

Fig. 2 3D model of crystallogram relief for the bile solution. (a) – before the impact; (b) – After 2 minutes of exposure (the wavelength 650 nm, the total energy density 30 J/cm^2).

The study of crystallograms of irradiated and unirradiated aqueous solutions of bile has shown that their structures also significantly differ both qualitatively and quantitatively (Fig. 2). In particular, it was found that in the crystallogram from the unirradiated solution the structure (peaks) possesses the height smaller by nearly an order of magnitude (0.15 μm for the unirradiated solution and 1.2 μm for the irradiated one). The level difference between the individual crystallogram patterns is also smaller by nearly an order of magnitude and amounts to approximately 35-40 nm upon average. Alongside with these facts, the crystallogram patterns for the unirradiated solution are arranged much more densely, in contrast to the crystallogram of the irradiated solution, although the mean transverse structure size in both cases differs slightly an equals nearly 1-2 μm (Fig. 3).

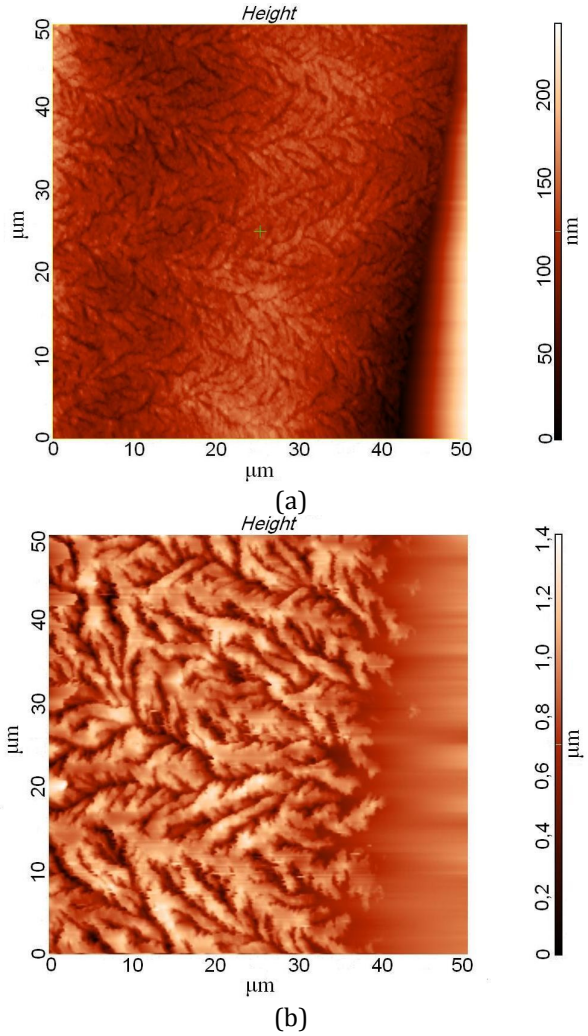

Fig. 3 2D image of the crystallogram surface. (a) – Before the impact; (b) – After 2 minutes of exposure (the wavelength 650 nm, the total energy density 30 J/cm^2).

A possible mechanism of the laser radiation effect on the crystallisation processes in volume and thin

layers of organic solutions consists in the decomposition of large molecular associates that otherwise could be nucleation centres into smaller associates [14, 15]. Similar to the case of Grippferon solution, under the irradiation with relatively low power the validity of this hypothesis is demonstrated by both the reduction of the characteristic crystallogram size and the decrease of the mean layer thickness.

However, in the case of bile, the considerable radiation power density as compared to that used in Refs. [14, 15] to act on the solution, caused the increase of the solution temperature, the substrate staying "cold". Therefore, the enhancement of the film crystal formation took place, in contrast to the crystallisation of unirradiated solution. Since the crystallisation occurred in a thin layer, together with the temperature difference it additionally accelerated the crystallisation, leading to the difference in the density of arrangement of crystalline structures between the irradiated and unirradiated solutions.

4 Conclusion

Thus, it is experimentally shown that under the effect of laser radiation the structure of Grippferon protein solution changes, which manifests itself in the characteristic size of the crystallogram segments. These changes can be not only detected qualitatively, but also determined quantitatively using the 3D models of the crystallogram surface, obtained by means of a probe microscope. Further improvement of the quantitative estimation procedure is required to consider the entire amount of information contained in the 3D model and to automate the image processing procedure.

The laser radiation of green range produces more significant structure change as compared to that produced by red radiation, which is probably due to the greater quantum energy.

The analysis of crystallograms of bile aqueous solutions also allows a suggestion that the laser radiation affects the crystallisation processes in bile preparations. The mechanisms of the effect are not studied yet, and its hypothetic explanation is related to the changes of the biological fluid structure that occur under the irradiation of the solution [11].

Disclosures

The authors have no relevant financial interests in this article and no potential conflicts of interest to disclose.

Study of Tumour and Surrounding Tissue Heating with Near-Infrared Radiation after the Injection of Gold Nanoparticles into the Tissue

Vadim D. Genin[1*], Elina A. Genina[1,2], Alla B. Bucharskaya[3], Marina L. Chekhonatskaya[3], Georgy Terentyuk[3], Daria K. Tuchina[1], Nikolay G. Khlebtsov[4], Valery V. Tuchin[1,2,5], and Alexey N. Bashkatov[1,2]

[1] Saratov State University, 83 Astrakhanskaya Str., Saratov 410012, Russia
[2] Tomsk State University, 36 Prosp. Lenina, Tomsk 634050, Russia
[3] Saratov State Medical University named after V.I. Razumovsky, 112 Bol'shaya Kazachya Str., Saratov 410012, Russia
[4] Institute of Biochemistry and Physiology of Plants and Microorganisms, Russian Academy of Sciences, 13 Prosp. Entuziastov, Saratov 410049, Russia
[5] Institute of Precision Mechanics and Control, Russian Academy of Sciences, 24 Rabochaya Str., Saratov 410028, Russia

*** e-mail:** versetty2005@yandex.ru

Abstract. We study the heating kinetics in transplanted model tumours after the intravenous injection of suspension of gold nanorods having the concentration from 400 to 1200 μg/mL under the laser irradiation at the wavelength 808 nm during 15 min. The object of study were 40 outbred white laboratory rats with transplanted liver cancer tumours (Cholangiocarcinoma PC1). The obtained results allow the optimisation of the gold nanorods injection technique at different degrees of vascularisation of tumour tissues aimed to provide the maximal heating of tumours by the laser radiation. It is shown that the maximal increase of the tumour temperature is related to the maximal accumulation of gold nanorods in the tumour tissues, observed in the case of its high vascularisation.

Keywords: tumour; NIR laser irradiation; photothermal therapy; gold nanorods.

Paper #3282 received 26 Feb 2018; revised manuscript received 12 Mar 2018; accepted for publication 16 Mar 2018; published online 31 Mar 2018. doi: 10.18287/JBPE18.04.010505. [Special Section. Workshop "Biophotonics" of the XV all-Russian Youth Samara conference-contest on optics and laser physics]

References

1. N. N. Aleksandrov, N. E. Savchenko, S. Z. Fradkin, and E. A. Zhavrid, Using Hyperthermia and Hyperglycaemia in the Treatment of Malignant Tumours, Meditsina, Moscow (1980) [in Russian].
2. G. F. Baronzio, and E. D. Hager, Hyperthermia In Cancer Treatment: A Primer Series Medical Intelligence Unit XXIII, New York (2006).
3. K. K. Jain, "Advances in the field of nanooncology," BMC Medicine 8, 83, (2010).
4. N. S. Abadeer, and C. J. Murphy, "Recent progress in cancer thermal therapy using gold nanoparticles," The Journal of Physical Chemistry C 120(9), 4691-4716 (2016).
5. X. Huang, P. K. Jain, I. H. El-Sayed, and M. A. El-Sayed, "Plasmonic photothermal therapy (PPTT) using gold nanoparticles," Lasers in Medical Science 23(3), 217-228 (2008).
6. E. B. Dickerson, E. C. Dreaden, X. Huang, I. H. El-Sayed, H. Chu, S. Pushpanketh, J. F. McDonald, and M.A. El-Sayed, "Gold nanorod assisted near-infrared plasmonic photothermal therapy (PPTT) of squamous cell carcinoma in mice," Cancer Letters 269(1), 57-66 (2008).
7. M. A. Sirotkina, V. V. Elagin, M. V. Shirmanova, M. L. Bugrova, L. B. Snopova, V. A. Nadtochenko, V. V. Kamenskii, and E. V. Zagaynova, "Laser hyperthermia of tumours using nanothermosensitisers," Sovremennye tekhnologii v meditsine 1, 6-11 (2010) [in Russian].

8. M. A. Sirotkina, V. V. Elagin, M. L. Bugrova, M. V. Shirmanova, V. A. Nadtochenko, and E. V. Zagaynova, "Optical diagnostics and laser hyperthermia of tumours using plasmon-resonance nanoparticles," Al'manakh klinicheskoy meditsiny 26, 63-67 (2012) [in Russian].
9. A. B. Bucharskaya, G. N. Maslyakova, N. I. Dikht, N. A. Navolokin, G. S. Terentyuk, A. N. Bashkatov, E. A. Genina, V. V. Tuchin, B. N. Khlebtsov, and N. G. Khlebtsov, "Cancer cell damage pathways at laser induced plasmon-resonant photothermal therapeutics of transplanted liver tumor," BioNanoScience 6(3), 256-260 (2016).
10. L. A. Dykman, and N. G. Khlebtsov, "Uptake of engineered gold nanoparticles into mammalian cells," Chemical Reviews 114(2), 1258-1288 (2014).
11. A. V. Alekseeva, V. A. Bogatyrev, B. N. Khlebtsov, A. G. Mel'nikov, L. A. Dykman, and N. G. Khlebtsov, "Gold nanorods: Synthesis and optical properties," Colloid Journal 68(6), 661-678 (2006).
12. M. A. Sirotkina, V. V Elagin., M. V. Shirmanova, E. V. Zagainova, P. V. Subochev, and N. N. Denisov, "Laser hyperthermia of tumors using gold nanoparticles monitored by optical coherence tomography and acoustic thermometry," Biophysics 56(6), 1102-1105 (2011).
13. M. Bonesi, S. G. Proskurin, and I. V. Meglinski, "Imaging of subcutaneous blood vessels and flow velocity profiles by optical coherence tomography," Laser Physics 20(4), 891-899 (2010).
14. E. A. Genina, Yu. I. Svenskaya, I. Yu. Yanina, L. E. Dolotov, A. N. Bashkatov, N. A. Navolokin, G. S. Terentyuk, A. B. Bucharskaya, G. N. Maslyakova, D. A. Gorin, V. V. Tuchin, and G. B. Sukhorukov, "*In vivo* optical monitoring of transcutaneous delivery of calcium carbonate microcontainers," Biomedical Optics Express 7(6), 2082-2087 (2016).
15. S. Schuh, J. Holmes, M. Ulrich, L. Themstrup, G. B. E. Jemec, N. De Carvalho, G. Pellacani, and J. Welzel, "Imaging Blood Vessel Morphology in Skin: Dynamic Optical Coherence Tomography as a Novel Potential Diagnostic Tool in Dermatology," Dermatology and Therapy (Heidelb) 7(2), 187-202 (2017).
16. L. Li, R. Wang, D. Wilcox, X. Zhao, J. Song, X. Lin, W. M. Kohlbrenner, S. W. Fesik, and Y. Shen, "Tumor vasculature is a key determinant for the efficiency of nanoparticle-mediated siRNA delivery," Gene Therapy 19, 775-780 (2012).
17. H. B. Frieboes, M. Wu, J. Lowengrub, P. Decuzzi, and V. Cristini, "A computational model for predicting nanoparticle accumulation in tumor vasculature," PLoS ONE 8(2), e56876 (2013).
18. K.-C. Mei, J. Bai, S. Lorrio, J. T.-W. Wang, and K. T. Al-Jamal, "Investigating the effect of tumor vascularization on magnetic targeting in vivo using retrospective design of experiment," Biomaterials 106, 276-285 (2016).
19. International Guiding Principles for Biomedical Research Involving Animals, CIOMS-ICLAS (2012).
20. W. T. Yang, G. M. K. Tse, P. K. W. Lam, C. Metreweli, and J. Chang, "Correlation between color power Doppler sonographic measurement of breast tumor vasculature and immunohistochemical analysis of microvessel density for the quantitation of angiogenesis," Journal of Ultrasound in Medicine 21(11), 1227-1235, (2002).
21. D. Kidron, J. Bernheim, R. Aviram, I. Cohen, A. Fishman, Y. Beyth, and R. Tepper, "Resistance to blood flow in ovarian tumors: correlation between resistance index and histological pattern of vascularization," Ultrasound Obstet Gynecol 13(6), 425-430 (1999).
22. M. Emoto, H. Iwasaki, K. Mimura, T. Kawarabayashi, and M. Kikuchi, "Differences in the angiogenesis of benign and malignant ovarian tumors, demonstrated by analyses of color doppler ultrasound, immunohistochemistry, and microvessel density," Cancer 80(5), 899-907 (1997).
23. B. N. Khlebtsov, E. S. Tuchina, V. A. Khanadeev, E. V. Panfilova, P. O. Petrov, V. V. Tuchin, and N. G. Khlebtsov, "Enhanced photoinactivation of Staphylococcus aureus with nanocomposites containing plasmonic particles and hematoporphyrin," Journal of Biophotonics 6(4), 338-351 (2013).
24. P. Puvanakrishnan, J. Park, D. Chatterjee, S. Krishnan, and J. W Tunnell, "In vivo tumor targeting of gold nanoparticles: effect of particle type and dosing strategy," International Journal of Nanomedicine 7, 1251-1258 (2012).
25. A. B. Bucharskaya, G. N. Maslyakova, N. I. Dikht, N. A. Navolokin, G. S. Terentyuk, A. N. Bashkatov, E. A. Genina, B. N. Khlebtsov, N. G. Khlebtsov, and V. V. Tuchin, "Plasmonic photothermal therapy of transplanted tumors in rats at multiple intravenous injection of gold nanorods," BioNanoScience 7(1), 216-221 (2017).
26. L. R. Hirsch, R. J. Stafford, J. A. Bankson, S. R. Sershen, B. Rivera, R. E. Price, J. D. Hazle, N. J. Halas, and J. L. West, "Nanoshell-mediated near-infrared thermal therapy of tumors under magnetic resonance guidance," Proceedings of the National Academy of Sciences 100(23), 13549-13554 (2003).

1 Introduction

The growth of oncological diseases stimulates extensive development of both early tumour diagnostics and therapy methods. Earlier it has been shown that the heating of a tumour leads to its death and the exposure regimes for tumour damage have been determined, namely, 120 minutes at 42°C, 60 minutes at 43°C, 30 minutes at 44°C and 15 minutes at 45°C [1]. However, the hyperthermia is restricted by low selectivity, which leads to significant damage of healthy tissues adjacent to the tumour. The laser hyperthermia is a promising method of fighting tumours that provides more heating locality than the traditional hyperthermia, which allows damage reduction in surrounding healthy tissues [2].

The use of sensitizers allows even higher selectivity of laser hyperthermia due to the reduction of the laser radiation power to the level safe for the healthy tissues adjacent to the tumour [3-7]. Nanoparticles possessing plasmon resonance near 800 nm are effectively applied as sensitizers, which makes it possible to use lasers with the appropriate generation wavelength as sources of radiation [8, 9]. It has been shown that gold nanorods (GNRs) are promising agents for photothermal tumour therapy (PTTT) due to their long-term circulation in blood flow [10], colloidal stability, easy spectral tuning of plasmon resonance [6], and efficient light-to-heat energy conversion [11].

In spite of multiple studies in the field, this kind of therapy requires optimising the dose of nanoparticles and their injection method, as well as the technique of heating them with near-infrared optical radiation, i.e., the power, exposure time, and depth of penetration of laser radiation into the tissue. The authors of Ref. [12] proposed the optical monitoring of accumulation of nanoparticles in the tumour using the optical coherence tomography. However, this method is applicable only to surface tumours, since due to the strong scattering of light in tissues the optical probing depth is restricted to 0.3-1.5 mm, depending on the illumination source wavelength [12-15]. Among other factors that affect the efficiency of using GNR for PTTT an important role is played by the degree of tumour vascularisation, i.e., the development of its blood vessel system, since the degree of vascularisation directly affects the accumulation of nanoparticles in the very object of study, the tumour tissue [16-18]. In turn, the accumulation of nanoparticles in the tumour tissue will determine the tumour temperature in the course of laser heating, directly affecting the PTTT efficiency [8]. Since to estimate the vascularisation of the tumour one needs the probing depth of about 10 mm, this problem can be solved using the Doppler USI. Unfortunately, in spite of its importance, the problem is still far from its final solution. Hence, the aim of the present paper is to study the heating kinetics in tumours with different vascularisation after the intravenous injection of gold nanorods.

2 Materials and methods

The object of study were 40 laboratory outbred male rats with the body mass 200 ± 20 g. The animals were kept in the Shared Cervices Centre of Saratov State Medical University named after V.I. Razumovsky under the standard vivarium conditions with fixed illumination regime. The animals were treated in accordance with the rules of the European Convention for the Protection of Vertebrate Animals used for Experimental and Other Scientific Purposes (Strasbourg, 1986) and the International Guiding Principles for Biomedical Research Involving Animals [19].

The experimental model of rat cholangiocarcinoma PC1 was obtained by subcutaneous injection of tumour cell suspension (2×10^6 cells/0.5 mL of Hanks solution). When the tumour volume achieved nearly 3 cm^3, the rat tumours were examined using the US system Voluson E8 Expert (GE Healthcare, USA) in the Doppler mode at the frequency 7.2 MHz. The 3D Doppler US imaging allowed the assessment of tumour vascularisation degree using the standard technique [20]. The estimation of the tumour vascularisation degree was based on the analysis of the resistance index (RI) of the tumour blood vessels, defined as the difference between the peak systolic velocity (PSV) and the end diastolic velocity (EDV) divided by the peak systolic velocity, RI = (PSV - EDV) / PSV. The values of PSV and EDV were determined in the course of dopplerography. It was found that at a certain stage of growth (RI ≤ 0.3) the developed afferent vessels with increased flow velocity appear in the tumour [21, 22].

Basing of the degree of tumour development, the animals were divided into two parties: 1) with poorly developed tumour vascularisation (24 animals with RI > 0.3); 2) with well-developed tumour vascular system (16 animals with RI ≤ 0.3).

Within these parties, the animals were randomly divided into 6 and 4 groups, respectively (10 groups overall, 4 rats in each group). Before the irradiation, the rats of eight groups were subjected to intravenous injection of GNR suspension. The experimental conditions are described in Table 1.

The gold nanorods were synthesised and functionalised with thiolated polyethylene glycol (molecular weight 5000, Nektar, USA) using the methods described in Refs. [11, 23]. The GNR geometric parameters determined by means of transmission electron microscopy (Libra-120, Carl Zeiss, Germany) amounted to 41 ± 8 nm (length) and 10 ± 2 nm (diameter). For the study, we used the GNR suspension with the concentration 400 μg/mL, which corresponds to the optical density 20 at the wavelength 810 nm. To increase the heating temperature, the animals of Groups 5 and 6 received the suspension with double GNR concentration, i.e., 800 μg/mL, 48 and 24 hours before the irradiation, respectively.

Table 1 Description of groups of animals used in the experiments (4 rats in each group).

Group number	Regime of injecting the GNR suspension doses	Total suspension dose
	Poorly developed tumour vascular system	
1	Irradiation without injecting nanoparticles	-
2	Single injection (1 mL) 24 hours before irradiation	400 μg/mL
3	Double injection (1 mL each, 400 μg/mL) 48 and 24 hours before irradiation	800 μg/mL
4	Triple injection (1 mL each, 400 μg/mL) 72, 48, and 24 hours before irradiation	1200 μg/mL
5	Single injection (1 mL) 48 hours before irradiation	800 μg/mL
6	Single injection (1 mL) 24 hours before irradiation	800 μg/mL
	Well-developed tumour vascular system	
7	Irradiation without injecting nanoparticles	-
8	Single injection (1 mL) 24 hours before irradiation	400 μg/mL
9	Double injection (1 mL each, 400 μg/mL) 48 and 24 hours before irradiation	800 μg/mL
10	Triple injection (1 mL each, 400 μg/mL) 72, 48, and 24 hours before irradiation	1200 μg/mL

To irradiate the tumours we used the diode laser LS-2-N-808-10000 with the wavelength 808 nm (Laser Systems Ltd., Russia). The exposure time was 15 min with the power density 2.3 W/cm^2. The laser spot area at the skin surface was ~0.5 cm^2. The temperature control of the tumour heating was implemented using the IR visualizer IRI4010 (IRYSYS, UK) with the interval of 30 s. Before all procedures the rats were anesthetised with Zoletil 50 (Virbac, France) dosed 0.05 mg/kg.

3 Results and Discussion

The heating kinetics of the experimental tumours and adjacent tissues is presented in Fig. 1. As seen from the figure, the laser irradiation of tumours without preliminary injection of GNR in Groups 1 and 7 caused insignificant increase of the tumour surface temperature approximately to 40°C, independent of the tumour vascularisation degree. In the case of poorly developed vascular blood flow, a single injection of the GNR suspension also caused the temperature growth not exceeding 40°C under the laser irradiation (Group 2). To our opinion, this is because no accumulation of a sufficient amount of nanoparticles occurs in the tumours due to the low vascularisation of the tumour tissue. This assumption is confirmed by the fact that the mean temperature of skin surface covering the tumour in Group 8 (with well-developed vascular blood flow) at the same dose as in Group 2 (with poorly developed vascular blood flow) achieved the value of 49.9±4.3°C, which is explained by considerable accumulation of particles in the tumour tissue.

Besides that, it is clearly seen that the dose doubling and tripling (Groups 3-6) has practically no effect on the temperature growth. The maximal temperature approached the values from 47°C to 52.2°C upon average, which allows a conclusion that in these groups no sufficient accumulation of nanoparticles in tumours occurred, because of the low tumour tissue vascularisation.

Note that in Group 9 we observed the temperature increase to 59.4 ± 10.4°C at the same injected GNR dose, as in Groups 3, 5, and 6. This group differed from Groups 3, 5, and 6 by higher vascularisation of tumour tissues, due to which in Group 9 the accumulation of nanoparticles appeared sufficient to provide significant tumour heating.

Group 10 has demonstrated the average temperature growth in the region of the tumour to 68.2°C, which, to our opinion, is related to the maximal GNR accumulation due to both the high total dose of the injected suspension and the high vascularisation of the tumour tissues. This assumption is confirmed by the data of Ref. [24], where it was shown that the maximal accumulation of nanorods in the tumour is observed in the case of triple injection of nanoparticles.

In Ref. [25] it was shown that the direct intratumoural injection of GNR suspension with the concentration 400 μg/mL followed by the irradiation of tumours with laser light at the wavelength 808 nm led to the increase of temperature in the heating zone to 65.5 ± 5°C. With this method of injection, the maximal amount of nanoparticles was accumulated in tumour. Since in our experiments (Groups 2-6, 8-10) the injection of GNR suspension was intravenous, the maximal concentration could be achieved only in the case of well-developed vascular system of the tumour.

To approximate the heating kinetics, presented in Fig. 1, we used the empirical equation:

$$T(t) = A_1\left(1-\exp\left(-\frac{t}{\tau_1}\right)\right) + A_2\left(1-\exp\left(-\frac{t}{\tau_2}\right)\right) + T_0, \quad (1)$$

where T_0 is the initial temperature (before heating) having the mean value of 32.9 ± 1.7°C, A_1 and A_2 are empirical constants, τ_1 and τ_2 are the constants that

characterise the heating rate for skin and tumour, respectively. The first term describes the heating kinetics of the adjacent tissues, and the second term describes the heating kinetics of the tumour itself.

The approximation parameters are presented in Table 2.

The analysis of the approximation parameters shows that after the intratumoural injection of GNR suspension the characteristic time of tumour heating is minimal. In this case, the degree of tumour vascularisation does not matter, since the nanoparticles are injected into the interstitial fluid. On the contrary, the characteristic time of heating for the surrounding tissues is maximal, which can be because the particles are localised in the injection sites, i.e., are not distributed uniformly over the tumour volume. Thus, sufficiently strong and fast heating of the localisation sites of nanoparticles occurs in combination with rather slow heat penetration into the surrounding tissues, which is in good correlation with the results of Ref. [26].

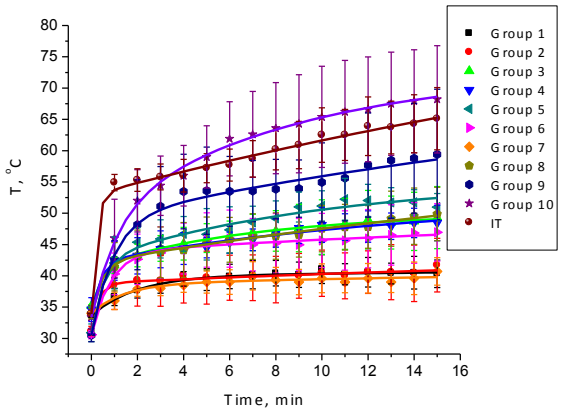

Fig. 1 Heating kinetics of experimental tumours and adjacent tissues stimulated by near-infrared radiation (the IT group comprises the rats subjected to a single intratumoural injection of GNR suspension with the concentration 400 μg/mL [25]).

In the first and the seventh groups of animals (irradiation without injection of nanoparticles), the value of τ_2 is relatively large. In the case of poorly developed vascular system (Group 1), the time necessary to heat the tumour is smaller than in the case of well-developed vascular system (Group 7), since the heat transfer from the heated region with the blood flow is weaker in Group 1. The value of τ_1, on the contrary, is smaller in Group 7, which confirms the greater velocity of heating the tissues surrounding the tumour at the expense of heat transfer from the heated region to the surrounding tissue with the blood flow.

The large deviation of the approximation parameters from the mean value, to our opinion, is related to the variety of structural features of tumours in individual animals and the location of blood vessels with respect to the irradiation zone. The latter is of primary importance in the case of intravenous injection of GNR. To determine these parameters with greater precision, one has to increase the sample volume, i.e., the number of studied animals, which is planned by the authors in future. However, the presented results of pilot experiments allow the observation that, overall, the increased vascularisation reduces the rate of tumour heating due to the increased temperature gradient from the irradiation zone.

The data of Table 2 allow the estimation of the partial contributions ΔT_1 and ΔT_2 to the experimentally recorded increment of temperature from the tumour itself and from the surrounding tissues, respectively, during the irradiation time ($0 < t < 15$ min). Here

$$\Delta T_1 = \frac{A_1\left(1-\exp\left(-\frac{t}{\tau_1}\right)\right)}{N},\ \Delta T_2 = \frac{A_2\left(1-\exp\left(-\frac{t}{\tau_2}\right)\right)}{N},$$

and $N = 31$ is the number of time points at which the temperature was measured. In Fig. 2a, the groups with equal volume of injected GNR suspension differing by the tumour vascularisation degree are presented in pairs.

Table 2 Parameters for approximating the experimental data.

Group number	Approximation parameters				
	T_0, °C	A_1	A_2	τ_1, min	τ_2, min
1	33.7±0.3	3.0±0.2	4.6±0.9	30.3±12.6	1.4±0.96
2	31.1±0.8	5.7±0.9	7.7±3.1	32.7±6.5	0.3±0.003
3	35.2±0.2	8.7±2.5	6.2±4.1	6.9±1.1	0.5±0.35
4	34.6±1.9	10.3±3.6	7.6±1.6	14.3±12.0	0.4±0.03
5	30.9±1.4	12.9±2.8	11.6±0.9	10.2±4.4	0.5±0.03
6	30.6±0.4	7.1±2.1	13.1±3.4	28.9±2.2	0.8±0.18
7	34.0±0.3	1.4±0.4	6.3±1.9	28.8±0.5	1.9±0.06
8	33.9±0.8	19.4±4.9	8.1±3.5	30.5±11.1	0.5±0.03
9	30.5±1.1	25.6±17.8	18.6±4.7	32.3±18.8	0.96±0.05
10	33.4±1.9	23.8±8.0	15.7±4.1	8.7±3.4	1.1±0.8
IT	33.9±0.2	40.9±13.0	19.0±0.9	41.9±6.9	0.2±0.01

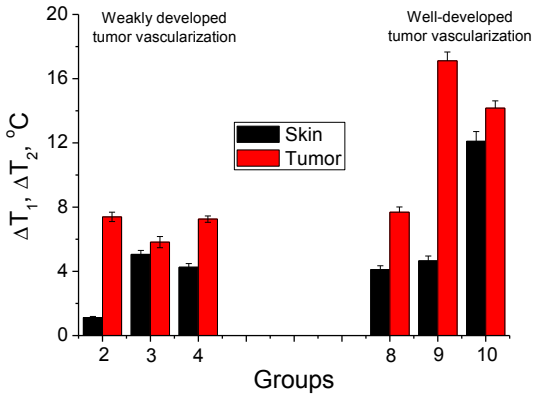

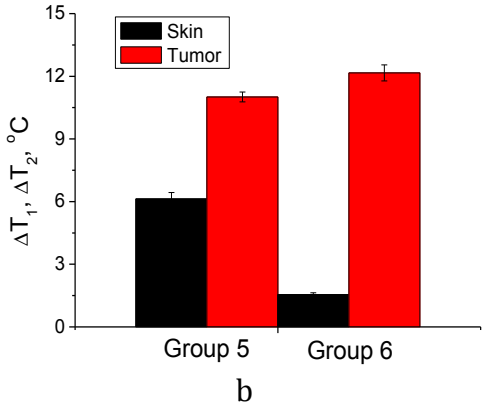

Fig. 2 Partial contributions ΔT_1 and ΔT_2 to the experimentally recorded temperature increment from the tumour and the surrounding tissues, respectively, in the groups of animals with equal volume of injected GNR suspension.

In Fig. 2a it is clearly seen that in the case of weakly expressed vascularisation degree the tumour heating due to GNR does not provide the temperature of the order of 45°C [1], necessary for the damage of cancerous cells (Groups 2-4), taking into account that the mean recorded initial temperature for all groups being 32.9 ± 1.7°C (see Table 2). Similar situation is observed for the animals with developed vascularisation of tumour after a single injection (Group 8). With double and triple increase of the GNR doze (Groups 9 and 10), the temperature necessary for damaging the cancer cells is achieved. However, for Group 10 we see unacceptable temperature growth in the tissues surrounding the tumour, which, to our opinion, is related to the escape of GNRs from the tumour vessels and their distribution in the surrounding tissues. This conclusion is confirmed by the data presented in Fig. 2b. It is clearly seen that when the GNRs are injected 2 days before the irradiation, the observed heating of surrounding tissues differs from the situation, when the same doze was injected only 1 day before irradiation. In the latter case, the growth of temperature in the surrounding tissues is essentially lower.

4 Conclusion

The obtained results allow a comparison of the techniques of gold nanorods injection providing the maximal heating of tumour with laser radiation. The maximal tumour temperature increase is related to the maximal accumulation of gold nanorods in the tumour. It is observed after triple intravenous injection of 400 μg/mL (the total dose 1200 μg/mL) 72, 48, and 24 hours before irradiation, provided that the vascular system of the tumour is sufficiently developed, since the accumulation of nanoparticles in the tumour tissue depends on its vascularisation degree. It is shown that in tumours with well-developed vascular system a trend that can be detected is the growth of the partial contribution of tumour heating under the increase of the GNR dose. However, when using a triple GNR injection, one can observe a damage of the surrounding tissues. Thus, to our opinion, the double injection of 400 μg/mL (the total dose 800 μg/mL) 48 and 24 hours before the irradiation is more preferable, if the vascular system of the tumour is sufficiently developed.

One of the ways to evaluate the tumour vascularisation degree is to use the Doppler USI. For the values of the tumour vessels resistance index ≤ 0.3 the vascularisation is sufficient for the PTTT procedure. Thus, the Doppler US visualisation of blood flow can be used to optimise the time of GNR injections before the PTTT with the purpose of improving the procedure efficiency.

Disclosures

All authors declare that there is no conflict of interests in this paper.

Acknowledgments

ANB, EAG and VVT acknowledge the MES RF (grant No.17.1223.2017/AP) for supporting the part of the work related to PPTT. The work with animals was supported by the Ministry of Health of the Russian Federation (ABB, MLC, GST). The synthesis of GNRs was supported by the RFBR grants Nos. 16-02-00054 and 17-02-00075 (NGK). Temperature measurements and analysis were obtained in the frameworks of the RF President's grant “Leading Scientific Schools” No. NSh-7898.2016.2 (VDG) and Scholarships of the President of the RF for young scientists (DKT).

Double-channel fluorimeter with pulsed excitation of advanced glycation end products in skin

Vladimir N. Grishanov*, Victor S. Kulikov, and Konstantin V. Cherepanov
Samara National Research University, 34 Moskovskoye Shosse, Samara 443086, Russia

*** e-mail:** vladgrishanov@yandex.ru

Abstract. A double-channel diagnostic fluorimeter operating in pulsed mode for *in vivo* assessment of the content of advanced glycation end products (AGEs) in skin by the autofluorescence integral intensity in the visible spectral region is developed. To excite the fluorescence we use a light-emitting diode with the peak wavelength 365 nm. A green light-emitting diode and an additional photodetection channel are intended to allow for the skin phototype of the patient. The fluorimeter analogue electronics comprises two photodetection channels based on silicon photodiodes. The accepted noise-suppressing circuitry solutions reduce the effect of sun and illumination lamp background light on the digital signal at the output of the 10-bit ADC to the one-bit level in both channels. The digital part of the fluorimeter is based on the Arduino platform. The software controls the operation modes of the fluorimeter, provides the quantitative processing of results, the diagnostic data storage and visualization. The experimental studies demonstrated the capabilities of revealing age-related changes in the skin.

Keywords: skin autofluorescence; fluorimeter; advanced glycation end products; medical diagnostics.

Paper #3274 received 15 Jan 2018; revised manuscript received 7 Mar 2018; accepted for publication 12 Mar 2018; published online 31 Mar 2018. doi: 10.18287/JBPE18.04.010506. [Special Section. Workshop "Biophotonics" of the XV all-Russian Youth Samara conference-contest on optics and laser physics].

References

1. R. V. Golubev, G. V. Papayan, A. A. Glazunova, N. Yu. Korosteleva, N. N. Petrishchev, and A. V. Smirnov, "Study of skin autofluorescence for determining the content of glycation end products in patients under chronic haemodialysis," Terapevticheskii arkhiv 88(6), 65–72 (2016) [in Russian].
2. D. A. Rogatkin, O. A. Prisnyakova, L. G. Moiseeva, and A. S. Cherkasov, "Analysis of the accuracy of clinical laser fluorescence diagnostics," Measurement Technique 41(7), 670-674 (1998).
3. I. A. Novikov, Ya. O. Grusha, and N. P. Kiryushchenkova, "Increasing the efficiency of fluorescence diagnostics of skin and mucosa neoplasms in ophthalmic oncology," Vestnik RAMN 10, 62-69 (2012) [in Russian].
4. A. V. Dunaev, V. V. Dryomin, E. A. Zherebtsov, S. G. Palmer, S. G. Sokolovskiy, and E. U. Rafailov, "Analysis of individual variability of parameters in laser fluorescence diagnostics," Biotekhnosfera 2(26), 39–47 (2013) [in Russian].
5. R. B. Blyumin, E. M. Naumova, and A. A. Khadartsev, "Technologies of non-contact diagnostics," Vestnik novykh meditsinskikh tekhnologiy XV(4), 146–149 (2008) [in Russian].
6. R. Meerwaldt, R. Graaff, P. H. N. Oomen, T. P. Links, J. J. Jager, N. L. Alderson, S. R. Thorpe, J. W. Baynes, R. O. B. Gans, and A. J. Smit, "Simple non-invasive assessment of advanced glycation end product accumulation," Diabetologia 47(7), 1324–1330 (2004).
7. D. J. Mulder, P. L. van Haelst, R. Graaff, R. O. Gans, F. Zijlstra, and A. J. Smit, "Skin autofluorescence is elevated in acute myocardial infarction and is associated with the one-year incidence of major adverse cardiac events," Netherlands Heart Journal 17(4), 162–168 (2009).

8. R. Meerwaldt, J. W. L. Hartog, R. Graaff, R. J. Huisman, T. P. Links, N. C. den Hollander, S. R. Thorpe, J. W. Baynes, G. Navis, R. O. B. Gans, and A. J. Smit, "Skin autofluorescence, a measure of cumulative metabolic stress and advanced glycation end products, predicts mortality in hemodialysis patients," Journal of the American Society of Nephrology 16(12), 3687–3693 (2005).
9. G. V. Papayan, N. N. Petrishchev, E. V. Krylova, K. Uk, S. V. Kim, V. B. Berezin, and B. Soo-Jin, "Method of estimating the biological age of skin by means of a fluorescence multispectral video dermatoscope," Journal of Optical Technology 77(2), 126-131 (2010).
10. M. S. Ahmad, T. Kimhofer, S. Ahmad, M. N. AlAma, H. H. Mosli, S. I. Hindawi, D. O. Mook-Kanamori, K. Šebeková, Z. A. Damanhouri, and E. Holmes, "Ethnicity and skin autofluorescence-based risk-engines for cardiovascular disease and diabetes mellitus," PLoS One 12(9), e0185175 (2017).
11. K. Uk, V. B. Berezin, G. V. Papayan, N. N. Petrishchev, and M. M. Galagudza, "Spectrometer for fluorescence-reflection biomedical research," Journal of Optical Technology 80(1), 40-48 (2013).
12. N. N. Bulgakova, V. V. Smirnov, V. I. Fabelinskii, A. G. Fedotov, and S. V. Shchichkin, "Spectral fluorescence colposcope," Biomeditsinskaya radioelektronika 4, 42–49 (2013) [in Russian].
13. D. V. Kornilin, and V. N. Grishanov, "Portable fluorescence meter for medical applications," Proceedings of SPIE 9887, 98871N (2016).
14. D. V. Kornilin, V. N. Grishanov, V. P. Zakharov, and D. S. Burkov, "Portable fluorescence meter with reference backscattering channel," Proceedings of SPIE 9961, 99610C (2016).
15. O. I. Kozlov, E. A. Zherebtsov, A. I. Zherebtsova, V. V. Dryomin, and A. V. Dunaev, "Laser Doppler flowmetry method and device for recording the intensity of the skin blood flow components," Biomeditsinskaya radioelektronika 6, 68–75 (2017) [in Russian].
16. I. A. Nakhaeva, O. A. Zyuryukina, M. R. Mohammed, and Yu. P. Sinichkin, "The effect of external mechanical compression on *in vivo* water content in human skin," Optics and Spectroscopy 118(5), 834-840 (2015).
17. I. A. Nakhaeva, M. R. Mohammed, O. A. Zyuryukina, and Yu. P. Sinichkin, "The effect of an external mechanical compression on in vivo optical properties of human skin," Optics and Spectroscopy 117(3), 506-512 (2014).
18. Y. Wang, L. Zhang, L. Zhu, Y. Liu, G. Zhang, and A. Wang, "A trifurcated fiber-optic probe based optical system designed for AGEs measurement," Proceedings of SPIE 8329, 832908 (2012).
19. G. T. Petrovsky (Ed.), Coloured Optical Glass and Special Glasses. A Catalogue, Dom optiki, Moscow (1990) [in Russian].
20. V. A. Petin, Project Using Arduino Controller, BKhV Peterburg, Saint-Petersburg (2014) [in Russian].
21. G. Petin, "Key synchronous detector," Skhemotekhnika 3, 14–15 (2003) [in Russian].

1 Introduction

The intensity of induced endogenous skin fluorescence, or autofluorescence (AF), is measured *in vivo* for diagnostic purposes in endocrinology, cardiology, and nephrology [1–8]. Complications of diabetes mellitus, coronary heart disease, and renal insufficiency lead to the increased concentration of advanced glycation end products (AGEs) in the skin, manifesting itself in the excess intensity of the skin AF. The processes of aging [9] and biological oxidation [5] of tissues are also accompanied by the change of AGE content in the skin.

The advanced glycation end products are a result of the reaction of sugars with proteins without enzyme participation. In collagen that contains a large amount of glucose, the AGE manifests itself in the increased number of covalent-bond cross-links [1]. The structures most probably responsible for the fluorescence intensity growth due to AGE include CDCCL (collagenase-digestible cross-links) and ECL (elastin cross-links), in which the long-wave edges of the excitation and emission bands amount to 360/420 nm and 390/420 nm, respectively. With age, the rate of ECL accumulation can slightly exceed that of CDCCL. Another cause of such dynamics can be the accumulation of lipofuscin pigment. Its fluorescence maximum lies in the green spectral region and the lipofuscin itself is known as an age pigment. It is worth noting that the most probable AGEs responsible for the increased level of autofluorescence, such as CDCCL, ECL, and pentosidine form a certain group of substances with similar properties, including the fluorescent ones [6, 9].

To assess the AGE content they use either different modifications of AGE-Reader devices [10], based on measuring the AF spectrum, or original all-purpose fluorimeters having a complex transformable structure [4, 5, 11, 12]. Since the originality and universality cannot provide operational and economic efficiency, the development of portable and easy-to-operate instrumentation for measuring the integral intensity of skin fluorescence is rather urgent.

The portable fluorimeter is based on measuring the integral parameter of the AGE content in skin, proposed in Refs. [6, 7]. The idea is to calculate the ratio of the measured value of the AF intensity in the wavelength range 420–600 nm to the intensity of the fluorescence-exciting radiation in the wavelength range 300–420 nm, elastically scattered by skin. The use of an integral criterion allowed essential simplification of the

diagnostic fluorimeter engineering solution by means of using two photodiodes in the receiving part, one of them installed after a cut-off optical absorption filter. This photodiode provides the analogue integration of the signal over the AF spectrum. The other photodiode records the signal of the AF-exciting ultraviolet (UV) radiation scattered elastically by the skin. At the expense of high sensitivity of photodetection channels, it was enough to excite AF with a low-power UV photodiode with purifying optical filter. This allowed the creation of a compact optical unit with low energy consumption and low supply voltage.

Earlier the authors proposed capable versions of diagnostic fluorimeters with continuous excitation [13] and additional channel for elastic scattering [14]. However, in the process of trial exploitation the effect of bright sunlight illumination on the instrument indications was revealed, although the forearm of the examined patient shielded the entrance window of the device. This effect is probably due to the background radiation arriving at the high-sensitivity detection channel after multiple scattering in the skin. Besides that, we observed intrinsic fluorescence from the cut-off optical filter made of coloured glass FGL435 (Thorlabs, USA), overlapping the AF spectrum of the skin.

In the integral assessment of AGE content in skin, one should allow for the significant individual variability of AF and elastic scattering signals [4], which can reduce the reliability of diagnostics. The probable causes of the individual variability include the endogenous melanin [11], the saturation of skin with blood microvessels at the measurement site [4], the vessels blood filling [15], and the skin tissue mechanical compression [16, 17]. Therefore, it looks promising to introduce additional information channels that would allow for the individual features of radiation absorption in skin. In particular, the authors of Ref. [18] proposed additional measurement of spectral intensity of radiation from a white light-emitting diode (LED) scattered by skin. However, the interpretation of the results for such wideband signal gives rise to certain difficulties in the measurement of the integral diagnostic parameter. In this case, it is reasonable to perform the measurements in the centre of the fluorescence band, using an additional coloured LED for this purpose.

The purpose of the reported study was to develop a version of the fluorimeter in which the individual variability of the integral diagnostic parameter, the effect of external illumination, and the fluorescence of its own optical elements would be reduced. This reduction was achieved by measuring the skin-scattered radiation in the visible spectral region using pulsed sources of radiation, frequency filtering in the photodetection channels, and low-AF materials in the construction of the fluorimeter optical scheme.

2 Functional diagram of the fluorimeter

The functional diagram of the fluorimeter with pulsed excitation is presented in Fig. 1. The excitation of AF of the AGE is implemented using the radiation of the EOLD-365-525 UV LED *1* having the peak wavelength near 365 nm that passes through the purifying optical filter *2* made of coloured 3 mm thick optical UFS6 glass. Detailed description of the function and choice justification of the coloured optical glass UFS6 is given in Ref. [14]. The UV radiation purified from the long-wave component *3* through the window in the metallic case of the device *4*, covered with the protective glass *5* (microscope slide 1 mm thick), is incident on the fluorescing object (forearm inner side) *6,* applied to the glass plate from outside.

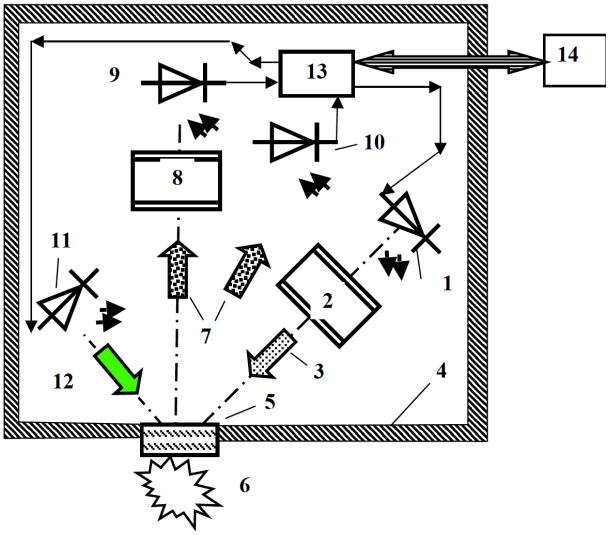

Fig. 1 Functional diagram of the alternating-current fluorimeter: 1 – light-emitting diode EOLD-365-525; 2 – purifying optical filter made of coloured optical glass UFS6; 3 – ultraviolet radiation flux; 4 – metallic case with a window; 5 – protection glass; 6 – object of study; 7 – flux of radiation scattered towards the photodetectors; 8 – cut-off optical ZhZS6 filter; 9 – BPW21R photodiode; 10 – SFH 229 photodiode; 11 – DFL-3014PGW green LED; 12 – flux of green radiation; 13 – electronics unit; 14 – PC; thin arrows show the electric connections and the directions of electric signal transmission.

A part of the exciting radiation scattered by the forearm skin and the fluorescence radiation *7* passes through the cut-off optical filter *8* made of coloured 3 mm thick ZhZS6 glass, in which the elastically scattered UV radiation is almost completely absorbed. The ZhZS6 glass does not belong to fluorescent materials [19] and, therefore, does not contribute to the recorded signal, which was confirmed experimentally. Thus, only the fluorescence radiation is incident on the silicon BPW21R photodiode *9*, so that the output electric signal from this photodiode is directly proportional to the integral intensity of the skin AF in the transmission band of the filter *3*. A part of elastically

scattered and fluorescence radiation is incident on the SFH229 photodiode *10*. Since the quantum efficiency of AGE fluorescence is small, we assume that the output signal from the SFH229 photodiode is proportional to the intensity of the exciting UV radiation, scattered by the skin. This photodiode belongs to the channel of the elastic scattering intensity measurement.

To reduce the variability of the integral diagnostic parameter, the green light-emitting diode DFL-3014PGW *11* with the peak wavelength 539 nm was introduced into the optical scheme of the fluorimeter.

The UV and the green LED are software switched on by turns and operate in pulsed mode with the pulse repetition rate 487 Hz, which allowed the synthesis of the receiving electronics for the alternating-current operation. The axes of the directional patterns of the UV and green LED make an angle ~45° with the normal to the protection glass *5*. Thus, the 45°/0° geometry of measuring the fluorescence and the elastic scattering is accepted. The functional diagram is completed with the unit of electronics *13* and the personal computer *14*.

3 The fluorimeter electronics unit

The fluorimeter electronics unit comprises two photodetector channels, two drivers of photodiodes, and the Arduino board [20]. The first photodetection channel is optimised for measuring the fluorescence intensity and the second channel for measuring the intensity of elastically scattered exciting UV radiation and the radiation of the greed LED. The LED drivers provide them with stable-amplitude currents, using the source of reference voltage. The Arduino board determines by software the sequence of switching the LEDs on, the repetition rate, and the off-duty ratio of the optical pulses.

A specific feature of the channel recording the fluorescence radiation is the system of active noise suppression, in which the frequency filtering method is implemented. As frequency-selective element the lock-in-amplifier [21] is used, since the fluorimeter comprises a source of reference pulsed signal.

In the skin AF fluorescence intensity measuring channel, the BPW21R photodiode operating in the photoconductive mode is connected to the transimpedance amplifier (current-voltage convertor), the signal from which is preliminarily amplified by the bandpass amplifier and arrives at the synchronous detector. The role of electronic analogue key is played by the CMOS multiplexor operating in the analogue mode. The electronic key is controlled by the same clock signal from the microcontroller unit, as the illuminator driver (that provides the synchronous mode of operation). The signal from the outputs of the electronic key arrives at the inputs of the instrumentation amplifier, where the detection occurs. The detected signal is applied to the input of the active low-pass filter. In the presented device, we use the active low-pass Sallen-Key filter of the second order, the nominals of the RC-components of which provide the Q-factor equal to 16. The electronic key, the instrumentation amplifier, and the low-pass filter comprise the synchronous detector. The detected filtered signal arrives at the final amplifier, from which the signal is transmitted to the analogue-to-digital convertor (ADC) of the Arduino board. The final amplifier executes the scaling function in order to use the entire dynamic range of the ADC.

In the channel measuring the intensity of the elastically scattered radiation, the silicon SFH229 photodiode is used as a photosensitive element. The level of the recorded signal in this case is relatively high, and no additional noise-suppression system is necessary. One should only match the maximal level of the output signal with the ADC dynamic range and suppress the background radiation from the natural and artificial illumination sources. The channel consists of the transimpedance amplifier of alternating voltage and the peak amplitude detector based on diodes with doubling (to enhance the linearity, the Schottky diodes with small forward voltage drop are used). The detected signal is applied to the input of the second ADC of the Arduino board.

4 Fluorimeter construction

Structurally the fluorimeter consists of a remote unit, an additional 12 V power supply, and a PC. The base for mounting the electronics *2* is the bottom cover *1* of the case (Fig. 2). In the top cover of the case, a ∅10 mm window is drilled that serves for exciting the patient's skin fluorescence and for receiving the fluorescence and elastic scattered radiation. The optical-to-electrical (OE) unit of the fluorimeter *4* is mounted coaxial with the window. The OE unit carrying the LEDS and the photodiodes determines the geometry of detecting the intensity of fluorescence and elastic scattering.

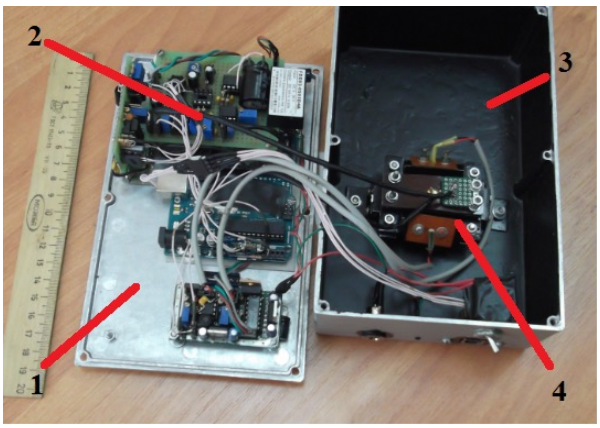

Fig. 2 Construction of the fluorimeter remote unit: 1 – bottom cover; 2 – boards of electronics unit; 3 – top cover of the case; 4 – optical-to-electrical unit.

For performing diagnostic procedures, the remote unit is placed on a table with its window up. The inner side of the patient's forearm is applied to the window, although, in principle, the remote unit can be applied

itself to any part of a human body. The case of the remote unit has the dimensions 153×83×51 mm.

The fluorimeter software creates and saves on a disc of the controlling PC the file, containing the information on the patient, the date and time of the diagnostic procedure, the values of signals (counts) from the ADC of the Arduino platform in arbitrary units for the UV or green LED switched on. The file also contains the results of statistical processing of the signals, in particular, the arithmetic mean amplitudes during the measurement time for the signals of autofluorescence, *MF*, elastic scattering with the UV LED switched on, ME_{UV}, elastic scattering with the green LED switched on, ME_G; the coefficients of variation for the signals of autofluorescence, *VF*, elastic scattering with the UV LED switched on, VE_{UV}, elastic scattering with the green LED switched on, VE_G; the mean amplitude ratios of autofluorescence to elastic scattering in the UV range, MR_{UV}, autofluorescence to elastic scattering in the green range, MR_G, and autofluorescence signal to the product of elastic scattering signals in the UV and green range, MR_{UVG}.

5 Results of the fluorimeter testing

The fluorimeter was calibrated using the black body model (BBM) and the fluoroplastic sample – a certainly non-fluorescing object with stable optical properties. The experiments with BBM were aimed to estimate the contribution of the electronic tract noises, the radiation scattered by the fluorimeter elements, and the cross-talk of channels due to imperfections of the purifying and cut-off optical filter. The following results were obtained. With the UV LED switched on at the output of the fluorescence channel we got *MF* = 68 arb. units with the coefficient of variation *VF* = 3%. At the output of the elastic scattering channel we obtained ME_{UV} = 14 arb. units with the coefficient of variation VE_{UV} = 5%. With the green LED switched on at the output of the elastic scattering channel we got ME_G = 168 arb. units with the coefficient of variation VE_G = 0,4%. Note that during the green LED operation the fluorescence channel was automatically switched off to prevent saturation. In the subsequent experiments, we interpreted the above values as steady-state noises with constant arithmetic mean values and programmatically subtracted them.

In the fluorimeter trial with the stable fluoroplastic scatterer and the UV LED switched on, no significant signal increase at the output of the fluorescence channel was observed, and the coefficient of variation amounted to *VF* = 4%, which differs from the BBM experiments by 1%, i.e., within the measurement error. The mean value of the signal at the output of the elastic scattering channel increased to ME_{UV} = 41.5 arb. units, the coefficient of variation being VE_{UV} = 1.7%. With the green LED switched on, the mean value increased to ME_G = 318.2 arb. units, the coefficient of variation being VE_G = 0.21%. The external background illumination, caused by the sunlight and the illuminating lamps did not manifest itself in the output signal.

Thus, the instability of the optical-to-electrical system of the fluorimeter that can be considered as the instrumentation error does not exceed 2 arb. units.

The individual variability of the results and the stability of the fluorimeter indications were estimated by repeating multiple measurements at nearly the same site of the left forearm inner side of the same volunteer (Table 1). The first series of measurements simulated the standard diagnostic procedure and was repeated during 2.5 months every three days at nearly the same time of the day. The second and the third series were performed during one hour with removing the forearm from the window before each new measurement. The fourth series of measurements was performed without removing the forearm from the window to demonstrate the stability of indications.

Table 1 Individual variability of the measurement results.

No. of the series	The number of experiments in the series	Coefficient of variation		
		VF, %	VE_{UV}, %	VE_G, %
1	28	13	20	22
2	8	10	8	4
3	10	4	6	3
4	8	1.0	2.1	1.7

Comparing the values of the variation coefficients obtained in the series with removing the forearm from the window, one can see that a considerable contribution to the variability of indications arises from uncontrollable changes in the conditions of the experiment, caused by the change of the chosen area of exposure and the forearm position. The series 4, performed without removing the forearm, demonstrates the stability of the instrument indications.

In 58 practically healthy persons aged from 16 to 65 years, a comparative experiment on the stability of the diagnostic parameters MR_{UV} and MR_{UVG} with respect to the endogenous melanin was carried out. The authors proceeded from the fact that the skin of the outer side of forearm contains greater concentration of melanin as compared to the inner side. This fact can be easily confirmed visually, since the outer side of the forearm always looks more suntanned, and experimentally, by the smaller values of the signals MF_{UVe}, ME_{UVe}, ME_{Ge} for the outer side in comparison with their values MF_{UVi}, ME_{UVi}, ME_{Gi} for the inner side.

The experiment was carried out as follows. The inner and outer side of the forearm were alternately applied to the input window of the device. As a result, the values of the diagnostic parameters were measured for the inner (MR_{UVi} and MR_{UVGi}) and outer (MR_{UVe} and MR_{UVGe}) sides of the forearm of each arm, and the absolute values of the relative differences of these diagnostic parameters were calculated:

Table 2 Age-related changes of the normalised ratios.

Number of tested persons	Age interval, years	Interval centre, years	RF_{UV}, arb. units	Coefficient of variation, %	RF_G, arb. units	Coefficient of variation, %	RF_{UVG}, arb. units	Coefficient of variation, %
47	16-25	20	0.59	23	0.65	33	0.60	30
9	26-35	30	0.67	35	0.84	17	0.62	44
4	36-45	40	0.71	12	0.55	22	0.77	8
4	46-55	50	0.71	11	0.95	33	0.67	23
7	56-65	60	1.0	27	1.0	36	1.0	34
Parameters of linear regression equation		k_1	7.44×10^{-3}		7.778×10^{-3}		7.677×10^{-3}	
		k_0	0.435		0.446		0.43	

$$DR_{UV} = |2\,(MR_{UVi} - MR_{UVe}) \,/\, (MR_{UVi} + MR_{UVe})|, \quad (1)$$

$$DR_{UVG} = |2\,(MR_{UVGi} - MR_{UVGe}) \,/\, (MR_{UVGi} + MR_{UVGe})|. \quad (2)$$

The arithmetic mean values of the relative differences for 58 patients amounted to M(DR_{UV}) = 0.28 and M(DR_{UVG}) = 0.18, i.e., M(DR_{UV}) / M(DR_{UVG}) = 1.5, which allows a conclusion that the diagnostic parameter MR_{UVG} is less sensitive to such destabilising factor as endogenous melanin.

Table 2 summarises the measurement data for the patients divided into age groups, with the standard statistical processing of the results performed within each group. The measured values of MR_{UV}, MR_G, MR_{UVG} were preliminarily normalised to the maximal value in the group:

$$RF_{UV} = MR_{UV} \,/\, MR_{UV,\,max}, \quad (3)$$

$$RF_G = MR_G \,/\, MR_{G,max}, \quad (4)$$

$$RF_{UVG} = MR_{UVG} \,/\, MR_{UVG,\,max}. \quad (5)$$

Then using the least squares method, the parameters for the linear regression equation were determined for each normalized mean value of the signals (3) – (5):

$$y(t) = k_1\, t + k_0, \quad (6)$$

where t is the age of a healthy patient expressed in years. The values of k_1 and k_0 for each of the functions [$RF_{UV}(t)$, $RF_G(t)$, $RF_{UVG}(t)$] ≡ $y(t)$ are also presented in Table 2.

The obtained trend of age-related changes of AGE agrees with the results of Refs. [6, 9, 14] for all the three ratios MR_{UV}, MR_G, MR_{UVG} due to the small difference of the linear regression parameters (see Table 2). One can see that in the case of considering only the scattering and absorption in the fluorescence emission band, the ratio RF_G is characterised by relatively large coefficients of variation. However, for the simultaneous consideration of the skin absorption and scattering in the UV and visible spectral region, RF_{UVG} weakly differs from the values obtained considering only the individual skin properties at the excitation wavelength, RF_{UV}. The latter is probably due to two reasons: the greater intensity of the exciting UV radiation and the limited statistical data, which does not allow unambiguous preference of one of the normalisation methods.

6 Conclusion

A fluorimeter intended for *in vivo* diagnostics of the content of fluorescent advanced glycation end products in human skin is designed, its characteristics are experimentally studied and the trial measurements are carried out. The use of pulsed radiation sources made it possible to improve the noise immunity of the fluorimeter against the background illumination, to normalise the integral diagnostic parameter allowing for the skin individual optical properties and phototype in the visible and UV spectral regions, to determine the individual variability of skin AF, and to reveal its age-related changes. We demonstrate that the integral diagnostic parameter, defined as the ratio of the fluorescence intensity to the product of intensities of the elastic scattering in the ultraviolet and green spectral regions, is more robust against the variations endogenous melanin content in skin than two other ratios (the fluorescence to UV or green scattering separately).

Disclosures

The authors have no relevant financial interests in this article and no potential conflicts of interest to disclose.

Acknowledgment

The work was supported by the Russian Foundation for Basic Research, grant No. 17-42-630907r_a.